Electrodynamic Guiding and Deceleration of Polar Diatomic Molecules

Richard Vincent Bernard Darnley

August 2007

Thesis submitted in partial fulfillment of the requirements for the degree of Doctor of Philosophy of the University of London and the Diploma of Membership of Imperial College.

Imperial College London

University of London

Declaration

With the exception of: the Stark shift calculation presented in Section 2.2 and the transverse acceptance of the decelerator in Figure (2.7) in Chapter 2; the expected CaF rotational line pattern presented in Figure (4.8) in Chapter 4; and the 3D numerical simulations presented in Chapter 5; I declare that the work presented in this thesis is my own.

Richard V B Darnley

Abstract

Electrodynamic Guiding and Deceleration of Polar Diatomic Molecules

Richard V B Darnley

I report on guiding and decelerating heavy polar diatomic molecules, $^{179}Yb^{19}F$ and $^{40}Ca^{19}F$, in the ground ro-vibrational and electronic state using an alternating gradient Stark decelerator. A study of clustering was undertaken pointing to a link between cluster formation and the molecular beam intensity. A cold ($\sim$3 K) supersonic beam of CaF molecules was developed for these experiments.

We studied the guiding properties of the Stark decelerator over a wide range of parameters, encompassing different voltages, molecular beam speeds and species. Transmission of molecules through the decelerator was compared to various theoretical predictions, and agreement was found only when a full 3-dimensional finite-element map of the electrostatic field of the lenses was considered. A localized strengthening of the defocusing force was found at the entrance and exit of the lenses. This defocusing field gradient, brought on by the non-zero longitudinal gradient in the fringe fields, is an inherent property of our two-electrode lens design. A better, four-electrode lens geometry is suggested. A universal scaling, applicable to harmonic lenses, was found. This allowed direct comparison between all the experimental and simulated transmission data, and worked remarkably well even when anharmonic and fringe field effects were significant. Some residual discrepancies remain to be understood.

YbF molecules have been decelerated, demonstrating an increased loss in kinetic energy (13%) over previous published results, and for the first time, we have decelerated (accelerated) CaF demonstrating a 10% loss (gain) in kinetic energy. The deceleration data agree with the expected energy loss, and also demonstrate the effect of longitudinal bunching. We have observed and understood a further loss of transmission when molecules are strongly decelerated. This is due to a decrease of the confining potential in the axial direction. The proposed 4-electrode decelerator is expected to produce more decelerated molecules.

Acknowledgements

I would firstly like to thank the principle investigator of this project, Ed Hinds, for his excellent supervision. His patience and support have been invaluable during my time with the group, and has made this thesis possible.

Special thanks also to Mike Tarbutt, for allowing me to join him on his quest to decelerate molecules, and for training me in the art of experimental physics! He has often been my first port of call in and outside the lab. and his expert, and clear explanations of physics, continue to be a source of inspiration to me. I am also very grateful for his careful proof reading of this thesis.

Many thanks to Jon Dyne; his mechanical expertise and hard work helped deliver a superbly built Stark decelerator. His help on all things mechanical has been hugely beneficial to the experiment, and the enthusiastic discussions on AutoCAD and Inventor we have had have been very enjoyable. Thanks also to Bandu Ratnasekara for his help with the electronic aspects of the experiment.

Thanks to Ben Sauer, whose help and advice on plumbing the water cooling of the lasers was invaluable. Thanks to Jalani and Tom, who have joined the decelerator team and are valiantly continuing experimental work on the AG Stark decelerator.

I would also like to thank all members of the CCM group, past and present, who have made life in and outside the lab. enjoyable. In particular, I thank Jony, Chris, Paul and Daniel whose company and good humour was very much appreciated.

Finally, thanks to my family for their support and encouragement throughout, and a very special thankyou to my girlfriend Sarah, who has done so much to help and encourage me throughout my PhD.

Contents

List of Figures

Chapter 1

Introduction

The last century has seen the advent and further development of quantum mechanics. Since then immense progress has been made experimentally, that has allowed the quantum nature of the microscopic domain to be probed and put to the test. A prime example is the cooling, trapping and manipulation of neutral atoms with laser light [1, 2]. Such powerful optical methods combined with magnetic trapping and evaporative cooling have managed to bring atomic vapours from room temperature all the way down to the nano-Kelvin range where the de Broglie wavelength is comparable to the mean atomic separation. Such coherent matter waves allow for the atom laser, atom interferometry and lithography. In 1995 this work had reached a further milestone: the attainment of a Bose-Einstein condensate, the ultimate coherent matter wave. Technical developments are now allowing the production and control of cold ($\sim$1K) and ultra-cold ($\sim \mu$K) molecules. The new physics promised by such ensembles of molecules will go beyond that provided by atoms, and is only just beginning to be realized in the laboratory. These experiments will improve the resolution of spectroscopic measurements, which many tests of fundamental symmetries depend on, and open new avenues in the investigation of collision physics and quantum chemistry.

In our laboratory we are interested in measuring the electron electric dipole moment using the heavy polar diatomic molecule ytterbium fluoride (YbF) [3]. This is a test for time reversal symmetry violation and thus is a search for new physics beyond the standard model. This experiment looks at shifts in the hyperfine energy levels of the ground state as they evolve in an externally applied electric and magnetic field. The current value is based on a measurement using a thermal source of YbF molecules [3]. The sensitivity of this measurement has been recently improved using a cold and more intense beam of ground state YbF molecules [4, 5], however, an even greater sensitivity is expected by slowing the molecules to increase the coherence time. This has motivated our entry into the exciting field of cold molecules.

Cold molecules will also have a major impact in the field of collision physics and chemistry; in a trapped ensemble of ultra-cold molecules, the collisions are influenced by tunneling

effects which can be sensitively controlled, either by choice of the initial quantum state, or by application of external electric and magnetic fields [6, 7], thus providing complete control over the reaction pathways. When these molecules are polar, their dynamics are strongly influenced by the long-range interactions of the dipole moments. This may also lead to a rich variety of spatial order over the length of the trapped cloud and be a prime toolbox for many-body physics [8]. Furthermore the strength of the interaction of the dipoles can be controlled by manipulating the trap geometry. For example, this would be useful in a quantum register composed of dipolar molecules, where it is important to be able to precisely control their interaction [9].

However, the now conventional laser cooling techniques used for atoms are nearly impossible to use with molecules. Simple atoms often have a closed set of levels that allow a very large number of photons to be absorbed and emitted between them without loss to other atomic levels. Similar cycling transitions rarely occur in molecules because their spontaneous decay branches to several vibrational and rotational levels, causing the ground state to decouple from the light and stopping the cooling. Translationally ultra-cold molecules can be approached by starting with ultra-cold, trapped atoms and photo-associating these to form molecules at temperatures similar to those of the colliding atom pairs. Taken a step further, Feshbach resonances have been used to join atoms in a Bose-Einstein condensate to form a molecular condensate. Both these techniques have been successful in making simple diatomic species at exceedingly low temperatures; Cs_2 [10], KRb [11] and LiCs [12] to name but a few. The constituent atoms of these molecules belong to the readily laser-cooled alkali atom group. However, more interesting molecules, composed of H, C, N, O and F atoms for example, cannot be made in cold atom traps, either because, the constituent atoms cannot be laser cooled, or because the molecules are too complex to assemble from atoms.

Several new cooling methods that act directly on the molecules as a whole have been investigated. Molecules with low translational temperatures, several Kelvin, can be filtered out of a room temperature thermal reservoir. This has been achieved by injecting an effusive beam of H_2CO molecules into a quadrupole guide [13]. The guide is bent at 90^o, and the centripetal force due to the electric field gradient guides only the slowest molecules. Alternatively, the molecules can be directly cooled by collisions with a cold bath. One technique uses cryogenically cooled helium buffer gas as the cold bath. The molecules cool by elastic collisions, and reach thermal equilibrium with the $\sim$300 mK He atoms. Combining this with magnetic trapping of paramagnetic molecules has yielded trapped samples of CaF [14], CaH [15], NH [16], VO [17] and PbO [18]. The range of cold molecular sources is extended to molecular ions when sympathetically cooled with laser-cooled atomic ions in an ion trap. The molecular ions thermalize with the atomic ions by coulomb collisions and, by appropriate choice of atomic ion, virtually any mass molecule may be cooled this way, including biological molecules [19]. To date, HCO^+, N_2H^+ [20] and MgH^+, MgD^+ [21], have been cooled in this

way to 4 K and 100 mK respectively.

A common technique for producing a wide range of cold ($\sim$1 K) atoms or molecules is to allow them to expand under high pressure through a nozzle into vacuum, a so called *supersonic source* [22]. This is an established technique that has been implemented on a vast array of atomic and molecular species across disciplines, and owing to the low temperature in the beam, it has been extensively used for high-resolution spectroscopy. We have used this technique to produce intense beams of cold YbF and cold CaF molecules [23] in the ground ro-vibrational electronic state. It seems natural therefore to seek a method that will reduce the centre of mass motion of these low temperature molecules to rest in the laboratory. The nozzle can be mounted on the end of a high speed rotor [24] whose counter-rotation cancels the flow velocity of the molecules that emerge from the nozzle, however greater control over the molecules is achieved by using the interaction between an electric field and the molecules to exert forces on them.

Significant effort has been invested in reducing the centre of mass motion of these molecules using the electric fields produced by intense laser beams and by charged conductors. Far off-resonant and intense laser light has been used to exert large deceleration forces on a supersonic molecular beam of nitric oxide and benzene molecules [25, 26]. The dipole moment, induced by the interaction of the intense laser field with the molecular polarizability, experiences a force that is dependent on the field intensity gradient. This technique is potentially widely applicable as many molecular species are, with sufficiently intense lasers ($\sim 10^{12}$ W/cm^2), polarizable, and the non-resonant character of the fields removes any critical dependence on the energy level structure of the molecule.

However, working with such intense lasers is a challenge. More modest electric fields, produced by charged conductors, are used to exert forces on polar molecules. The gradient of the Stark shift in an inhomogeneous static electric field induces a force which is used to decelerate the molecules. Prof. Meijer's group have pioneered this technique and have demonstrated the first deceleration of a molecular beam of CO molecules in a weak-field seeking state [27]. This showed that the kinetic energy of the beam was significantly reduced by 80% with a modest applied field of 125 kV/cm. The electric fields are produced by pairs of oppositely charged electrodes that straddle the beamline; this structure is called a Stark decelerator. As the molecules move along the beamline they pass through the field generated by the charged electrodes, and the electrode voltages are switched on and off in a particular time sequence. The decelerated group of molecules finds itself climbing a potential hill every time the volts are on and coasting with the fields switched off whenever they would otherwise be going downhill. Since the first demonstration of this technique, in 1999, it has been successfully applied to various other strongly polar and light molecules in their weak-field seeking states, including: $^{14}ND_3$ and $^{15}ND_3$ [28], OH [29, 30], H_2CO [7], SO_2 [31] and NH [32].

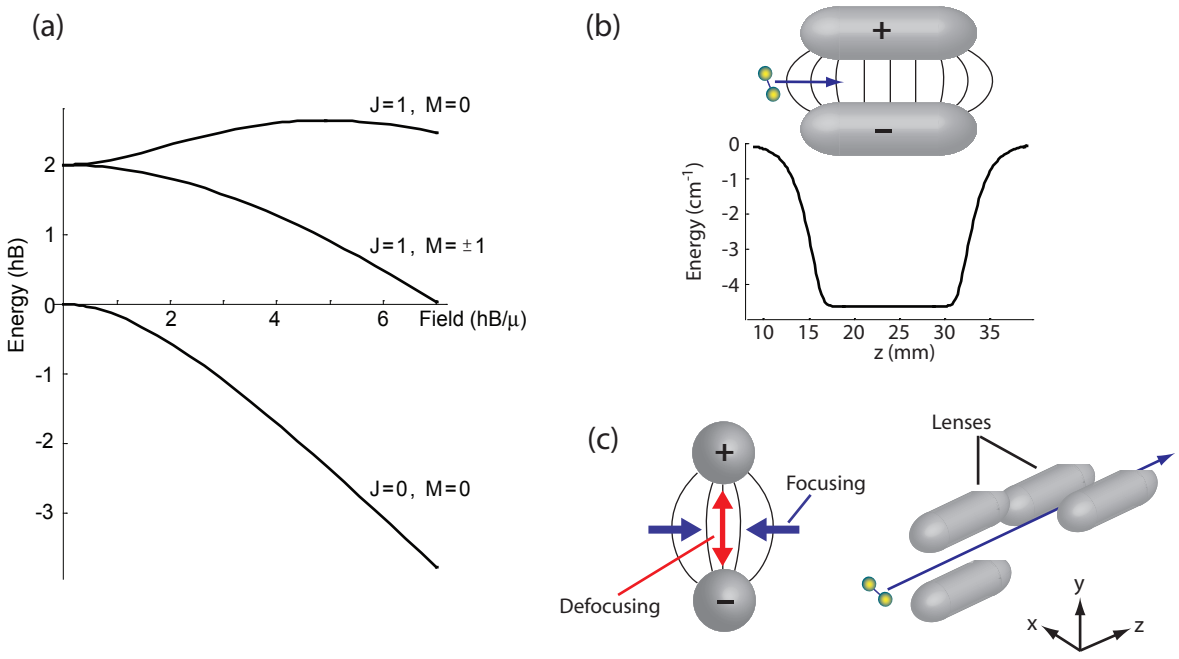

Figure 1.1: Alternating gradient principle.

This technique can be extended to heavy ground state molecules, or light molecules that are weakly polar, in an Alternating Gradient Stark decelerator. Figure (1.1) (a) shows the Stark shift of a rigid rotor molecule, with energy in units of the rotational constant hB and the applied electric field in units of hB/μ, where μ is the dipole moment of the molecule. The ground rotational state $(J = 0, M = 0)$ and the excited state $(J = 1, M = \pm 1)$ shift downwards in the electric field (seeking strong field), whereas $(J = 1, M = 0)$ initially shifts up (seeking weak field). The maximum energy that can be removed from a weak-field seeking molecule is the maximum upward Stark shift. A molecule in a weak-field seeking state moves up a potential hill as it approaches the charged electrodes, and the spatial gradient of the Stark shift exerts a force that removes kinetic energy from the molecule. If the electrodes are now switched off, the molecule will coast at the reduced speed. For the $(J = 1, M = 0)$ state of the rigid rotor the maximum energy loss is $0.64\,hB$. This typically represents a very small fraction of the initial kinetic energy, however, by repeatedly switching the electrodes on and off, complete removal of kinetic energy from the beam is possible, as has been demonstrated by most of the molecular species decelerated to date. As indicated in Figure (1.1) (b), a decelerating switching sequence for a molecule in a strong-field seeking state is slightly different; the electrodes are off as the molecule approaches the electrodes, and are only switched on when the molecule has passed the region where there is a downward potential hill. It is subsequently decelerated as it exits the electrode pair, and will continue to coast at a reduced velocity.

Decelerating heavy molecules in the $(J = 1, M = 0)$ state is unfeasible, as the maximum energy loss $0.64\,hB$ decreases as the mass of the molecule increases. In our supersonic molecular beam the slowest speeds are roughly 300 m/s; for YbF (m=3.2×10^{-25} kg, B=7.2 GHz, μ=3.9 Debye), the kinetic energy is ≈705 cm^{-1}, and $0.64\,hB$ ≈0.15 cm^{-1}. This means that approximately 4700 stages would be required to bring this beam to rest; this would be a prohibitively long decelerator! In contrast, the conditions for deceleration of ground state molecules are much more favourable; these states shift downwards strongly and indefinitely, limited only by the applied electric field strength. In a field of 100 kV/cm, the $(J = 0, M = 0)$ state for YbF shifts by $20\,hB$ making a decelerator of approximately 150 stages possible. Lighter molecules having roughly the same value of m/μ require roughly the same number of stages of 100 kV/cm each.

The biggest challenge associated with strong-field seekers is finding a way to keep them close to the molecular beam axis, as they are attracted to the strong fields on the electrode surfaces. In contrast to weak-field seekers, for which creating a field minimum on the beam axis is relatively straightforward, creating a maximum in the field strength on the beam axis is not possible. The alternating gradient decelerator circumvents this outcome; two identical and oppositely charged electrodes are shown in grey on the left in Figure (1.1) (c) pointing into the page. The applied voltages create a saddle-point in the field strength, which focuses strong-field seekers along the x–axis and defocuses them along the y–axis. We call this electrode pair a lens. Successive lenses are rotated by 90^o, as shown in the right diagram in Figure(1.1) (c), and bring about a net focusing force on the strong-field seeking molecules in both transverse planes. The alternating gradient focusing technique is very similar to that used in charged particle accelerators [33] and relies on the fact that the displacement of the molecules from the beam axis is always largest inside the focusing lenses and smallest when inside the defocusing lenses. The alternating gradient Stark decelerator has been successfully demonstrated using a strong-field seeking state of CO [34] and the ground ro-vibrational electronic state of YbF [35]. The YbF deceleration data in the latter publication was carried out in collaboration with Prof. Meijer's group and used a different lens array design than is presented in this thesis.

1.1 Experimental Approach

Figure (1.2) is an illustration of the experiment described in this thesis. YbF (CaF) are made in the reaction between sulfur hexafluoride (SF_6) molecules and the Yb (Ca) atoms released by ablation of a Yb (Ca) target using a Q–switched Neodymium-doped Yttrium Aluminum Garnet (Nd:YAG) laser. A molecular beam is formed when the laser ablation of the target is crossed by the expansion of an inert gas (e.g. Ar, Kr or Xe) containing a few percent of SF_6. This is a pulsed source operating at 10 Hz. On their way to the skimmer, the molecules

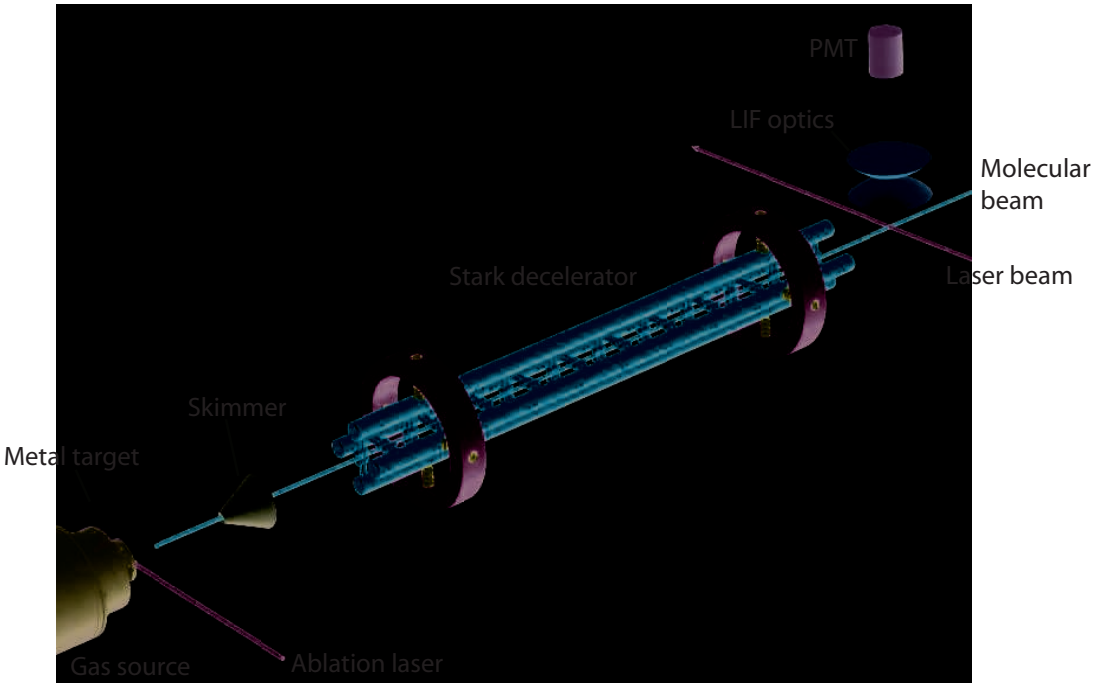

Figure 1.2: Experiment layout.

entrained in the carrier gas cool by collisions with the inert gas atoms, thus increasing the population in the ground state; after passing through the skimmer aperture they approach the entrance to the Stark decelerator. The applied voltages to the decelerator are switched on and off. By timing the switching pattern correctly, the alternating gradient arrangement of the lenses keeps the molecules close to the beam line whilst the downward gradient of the electric field magnitude along the beam axis decelerates them. The molecules are detected downstream of the decelerator by the method of laser-induced fluorescence (LIF) and the fluorescence is detected using a photomultiplier tube (PMT). A control computer synchronizes the time-resolved data collection from the PMT with the Q-switch of the Nd:YAG laser to yield molecular beam time-of-flight (TOF) data with 10 μs resolution.

1.2 Outline of the Thesis

The rest of this thesis is structured as follows. Chapter 2 explains the theory necessary to understand the motion of molecules through the Stark decelerator. This begins with an explanation of the Stark effect for polar molecules. The electric field produced by the electrostatic lenses is derived and used to calculate the forces exerted on the molecules. Finally the transverse and longitudinal motion of the molecules are considered. The formalism used to explain the transverse motion follows the treatment given in [36]. The experimental apparatus is then described in Chapter 3, which includes details of the vacuum system, the

molecular beam source, the laser system, and the construction and electrical testing of the Stark decelerator. Chapter 4 describes in detail the production and detection of cold beams of YbF and CaF molecules. The theory pertaining to supersonic beams is outlined and an account is given for the optimization of the intensity and speed of the molecular beam. A spectroscopic characterization of the CaF molecular beam is given and data demonstrating the formation of inert gas clusters is discussed. Chapter 5 presents a discussion of the observed guiding and deceleration of YbF and CaF molecules. Finally, Chapter 6 concludes the thesis with a summary and a discussion of ideas for future work.

Chapter 2

Theory of the Stark Decelerator

2.1 Principle

The dynamics of molecules within static electric fields is dependent on two factors: the geometry of the electric field and the internal quantum state of the molecule. The molecules do not move in a potential proportional to the electrostatic potential, but instead the motion is dictated by the Stark shift of their energy levels due to the local magnitude of the electric field. In an inhomogeneous field the molecules will experience a spatially modulated Stark shift.

This Stark potential, W, that the polar molecules move through is characterized by the familiar equation for the interaction between a dipole moment, $\boldsymbol{\mu}$, with an applied electric field, $\mathbf{E}(x, y, z)$

$$W = -\boldsymbol{\mu} \cdot \mathbf{E} = -|\boldsymbol{\mu}||\mathbf{E}| \cos\theta, \tag{2.1}$$

where θ is the angle between the dipole moment of the molecule and the electric field vector. This potential gives rise to a force through the relation $\mathbf{F} = -\boldsymbol{\nabla} W$. Thus we can write

$$\mathbf{F} = -\frac{\partial W}{\partial E} \boldsymbol{\nabla} E, \tag{2.2}$$

where $E(x, y, z)$ is the magnitude of the electric field vector. We immediately see the interplay between the quantum state of the molecule $\partial W/\partial E$ and the geometry of the field $\boldsymbol{\nabla} E$. For quantum states whose dipole moments are parallel to the electric field vectors the force and the electric field gradient also point in the same direction; a molecule in such a state is termed a strong-field seeker. Similarly, when a dipole is aligned in the opposite direction to the field, the force exerted on it is in opposition to the electric field gradient; a molecule in such a state is called a weak-field seeker.

The presence of an electric field perturbs the rotational motion of a linear molecule and this perturbation depends on the orientation of the angular momentum vector with respect

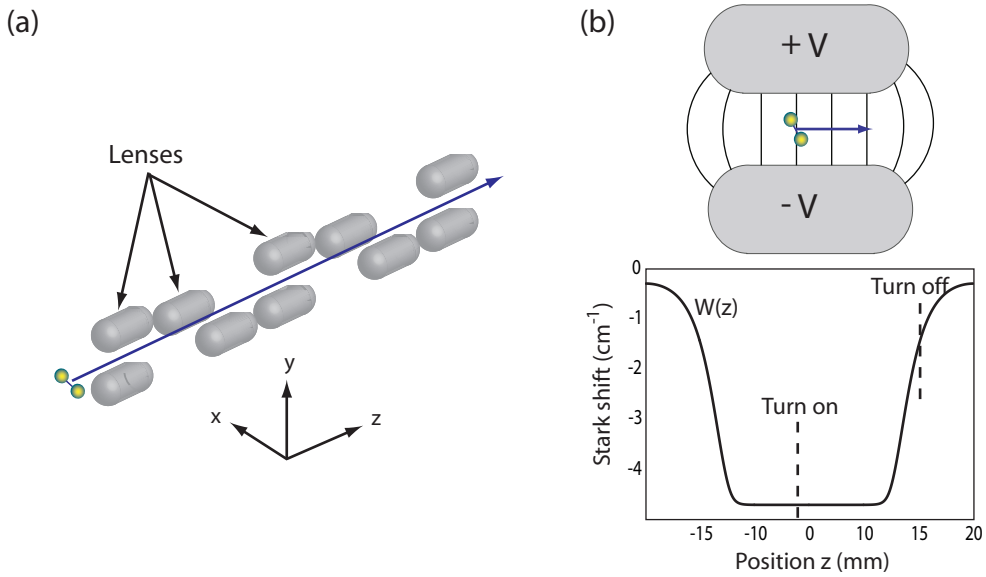

Figure 2.1: Lens electrode geometry and the molecular Stark shift.

to the applied electric field. Before we proceed to calculate the Stark effect we will continue to discuss several general principles regarding the use of the static inhomogeneous electric fields to control the motion of molecules.

Deceleration is easily implemented: a beam of polar molecules in strong field seeking states will lose energy as they move away from the high field region between two oppositely charged capacitor plates whereas molecules in weak field seeking states will be decelerated on entering the field between two capacitor plates. The energy removed by a single such capacitor stage is typically 0.5% of the initial kinetic energy and so this needs to be repeated many times to bring the molecules to rest.

This effect has a classical analogue: when a dielectric slab is moved towards the field of two oppositely charged capacitor plates it will feel an attractive electrostatic force that will accelerate it. Once between the plates, the presence of the dielectric material increases the capacitance and so the voltage between the plates will decrease if the charge on the plates is fixed. Thus the kinetic energy of the dielectric slab has increased at the expense of the energy in the field between the capacitor plates. The reverse situation corresponds to the Stark decelerator: as the molecules leave the field they lose kinetic energy, the energy density between the plates is now greater and so more work is done to discharge the plates.

The method for transverse confinement of a beam of polar molecules is not so straightforward and is highly dependent on their quantum state. In particular molecules in strong field seeking states are difficult to confine. Ideally we require the electric field magnitude to be a maximum on the molecular beam axis, however Earnshaw's theorem prohibits this [37, 38]. A way around this is to apply a field that is focussing along one transverse direction and

defocusing along the other.

There are two requirements for there to exist a static equilibrium in the motion of a neutral particle in the force field, $\mathbf{F}$: firstly, that the force vanishes at one point, say $\mathbf{r} = 0$; and secondly, that the force, to first order, restores the displacement of the particle back to this point. A Taylor expansion of this force is

$$\mathbf{F} = \mathbf{r} \cdot \nabla \mathbf{F}, \tag{2.3}$$

where the quantity, $\nabla \mathbf{F}$, is evaluated at $\mathbf{r} = 0$ and is a matrix whose elements are $(\nabla \mathbf{F})_{ij} = \partial F_j / \partial x_i$, where the indices run through the xyz axes. If we consider a coordinate system in which this matrix is diagonal then the only non-zero derivatives are $\partial F_x/\partial x$, $\partial F_y/\partial y$ and $\partial F_z/\partial z$ each of which must be negative if the force is to be restorative. In this coordinate system, the trace of $\nabla \mathbf{F}$ is simply the divergence of the force, $\nabla \cdot \mathbf{F}$, which must also be negative.

The force acting on molecules is $\mathbf{F} = -\boldsymbol{\nabla} W$ and for molecules that experience a linear Stark shift with applied electric field, $W = -\boldsymbol{\mu} \cdot \mathbf{E}$, it can be shown that the sign of $\nabla \cdot \mathbf{F}$ is solely determined by the sign of μ [39]. Thus for weak-field seekers $\nabla \cdot \mathbf{F} \leq 0$ is always true. However for high-field seekers, for which μ is positive, we have that $\nabla \cdot \mathbf{F} \geq 0$, thus focussing is not guaranteed.

2.2 Stark Effect of a Linear Diatomic Polar Molecule

A rotating polar diatomic molecule can be modelled as a linear rigid rotor with the vector dipole moment, μ, lying along the internuclear axis [40]. In the centre of mass frame of the molecule the hamiltonian of a rigid rotor in a uniform electric field $\mathbf{E}(x, y, z)$ is

$$\hat{\mathbf{H}} = \frac{\hbar^2 \hat{\mathbf{J}}^2}{2I} - \boldsymbol{\mu} \cdot \mathbf{E}, \tag{2.4}$$

where I is the moment of inertia of the molecule and $\hat{\mathbf{J}}$ is the total angular momentum operator. Equation (2.4) can be solved in the basis of the field-free eigenfunctions which are the solutions to the field-free hamiltonian

$$\hat{\mathbf{H}}_\mathbf{0} = \frac{\hbar^2 \hat{\mathbf{J}}^2}{2I}. \tag{2.5}$$

The field-free eigenfunctions of the rigid rotor are the spherical harmonic functions which are characterized by the rotational angular momentum quantum number, J, and magnetic quantum number M:

$$Y_M^J(\theta, \phi) = N_{JM} P_{|M|}^J(\cos\theta) e^{iM\phi}, \tag{2.6}$$

where

$$N_{JM} = \left[\frac{(2J+1)}{4\pi}\frac{(J-|M|)!}{(J+|M|)!}\right]^{1/2} \tag{2.7}$$

is a normalization constant, θ the angle between the internuclear axis of the molecule and the space-fixed z–axis, and $P^J_{|M|}(\cos\theta)$ are the associated Legendre polynomials. The energy eigenvalues of the field-free rotor are given by the equation

$$E_J = hB_0J(J+1). \tag{2.8}$$

The quantum number J can take any positive integer value $J = 0, 1, 2, \ldots$ and M any integral value in the interval $-J \leq M \leq +J$. The pre-factor has been written in terms of the rotational constant $B_0 = h/8\pi^2I$.

Returning to the linear rigid rotor in an electric field. The energy equation we wish to solve is

$$\hat{\mathbf{H}}\Psi = \varepsilon\Psi, \tag{2.9}$$

where ε is the new energy eigenvalue corresponding to the perturbed eigenfunction Ψ and the hamiltonian $\hat{\mathbf{H}}$ is given by Equation (2.4). In the basis spanned by the perturbed eigenfunctions Ψ the hamiltonian $\hat{\mathbf{H}}$ would be diagonal with the energy eigenvalues being the diagonal elements. However we are working in the basis of the field-free eigenstates $Y^J_M(\theta,\phi)$ and in this case the interaction term gives non-zero off-diagonal elements. The matrix elements of the hamiltonian are given by

$$\langle J'M'|\hat{\mathbf{H}}|JM\rangle = E_J\delta_{JJ'}\delta_{MM'} + \mu E\langle J'M'|Y^1_0|JM\rangle. \tag{2.10}$$

It is noted that the z-component of the unit length spherical vector operator, Y^1_0, is the angular operator $\cos\theta$ and the second term in Equation (2.10) is a standard result in the theory of angular momentum [41]. This term is non-zero only when $J' - J = \pm 1$ and $M = M'$. These non–vanishing angular matrix elements are given by

$$\begin{aligned}\langle J+1\,M|Y^1_0|J\,M\rangle &= \left(\frac{J^2-M^2}{(2J+1)(2J-1)}\right)^{1/2}\\ \langle J-1\,M|Y^1_0|J\,M\rangle &= \left(\frac{(J+1)^2-M^2}{(2J+3)(2J+1)}\right)^{1/2}.\end{aligned} \tag{2.11}$$

The computer program *Mathematica* has built in routines to evaluate these terms and an example of the resulting tri–diagonal hamiltonian matrix for $M = 0$ and with $J = 0, 1, 2, 3$ is

$$\begin{pmatrix} 0 & \frac{\mu E}{\sqrt{3}} & 0 & 0 \\ \frac{\mu E}{\sqrt{3}} & 2hB_0 & \frac{2\mu E}{\sqrt{15}} & 0 \\ 0 & \frac{2\mu E}{\sqrt{15}} & 6hB_0 & \frac{3\mu E}{\sqrt{35}} \\ 0 & 0 & \frac{3\mu E}{\sqrt{35}} & 12hB_0 \end{pmatrix}. \tag{2.12}$$

For a given value of M this matrix is in principle infinitely large i.e. $J = 0, 1, 2, .., \infty$ and for any J, M has values $M = -J, -J+1, ..., J-1, J$. The eigenvalues we seek are the diagonal elements that result after diagonalization of the hamiltonian matrix. As we cannot diagonalize an infinitely large matrix, in practice the hamiltonian matrix is written in a sub-space of the full state space spanned by the $|JM\rangle$ states. A Stark map is built up by repeating this procedure for various values of the electric field, and the results are plotted in Figure (2.2) for YbF and CaF. The values used for the mass m, rotational constant B_0 and the dipole moment μ are also included in the figure.

In the limit that the applied electric field is weak, $\mu E << hB_0$, the ground and first excited state perturbed energy levels ε_0 and ε_1 are close to the field-free ground and first excited state energy levels E_0 and E_1, and we can use second–order perturbation theory to give an expression for the perturbed energies

$$\varepsilon_0 = E_0 - \frac{\mu^2 E^2 |\langle 00|\hat{\mathbf{H}}|10\rangle|^2}{E_1 - E_0}, \tag{2.13a}$$

$$\varepsilon_1 = E_1 - \frac{\mu^2 E^2 |\langle 00|\hat{\mathbf{H}}|10\rangle|^2}{E_0 - E_1}. \tag{2.13b}$$

The perturbation theory results can be used to explain the form of the energy level shifts in an electric field shown in Figure (2.2) at low values of the electric field. The perturbation theory results tell us that the ground state energy ε_0, being the lowest energy state, is reduced whilst the first excited state energy ε_1 is raised as it is coupled to the ground state; these states repel each other. This is seen in the Stark map for the rotational levels, $|J = 0, M = 0\rangle$ and $|J = 1, M = 0\rangle$, of CaF for fields below 25 kV/cm shown in Figure (2.2). However the Stark effect couples states of all values of J for given M, i.e. the $|J = 1, M = 0\rangle$ state is also coupled to the $|J = 2, M = 0\rangle$ state, and the strength of this coupling increases as the field strength increases. This has the effect that for fields above 45 kV/cm, the $|J = 1, M = 0\rangle$ state for CaF begins to decrease whilst the $|J = 2, M = 0\rangle$ increases. At even higher values of the electric field the coupling between states $|J = 2, M = 0\rangle$ and $|J = 3, M = 0\rangle$ is similarly noticeable. By definition the ground state energy can only mix with higher energy states so that the perturbed ground state energy always decreases with applied electric field. This is similarly true for all for the $|J, M = J\rangle$ states as these are the lowest energy states in a given M manifold.

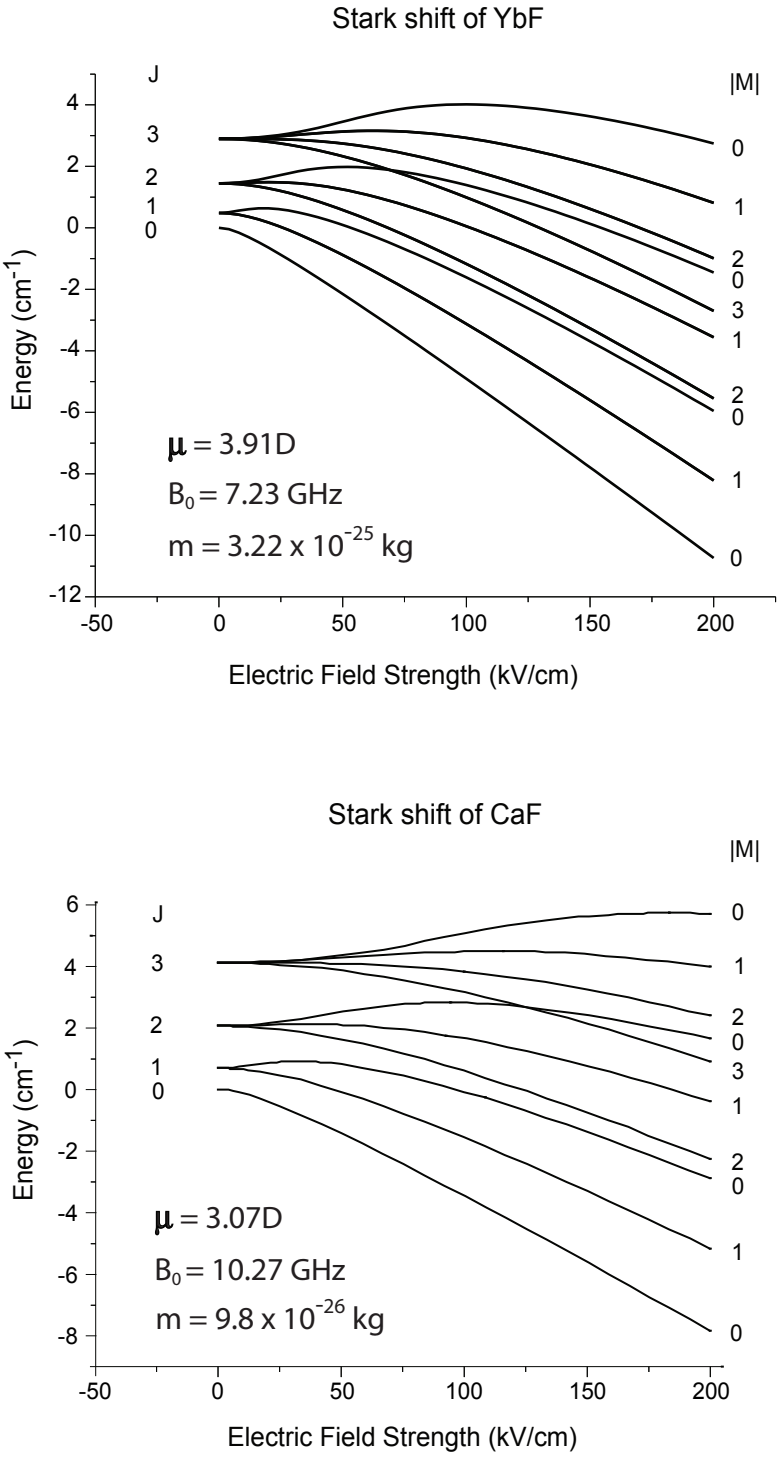

Figure 2.2: Shifts of the rotational energy levels of YbF and CaF in an electric field. For each molecule, the dipole moment μ, rotational constant B_0 and mass m have been included for reference.

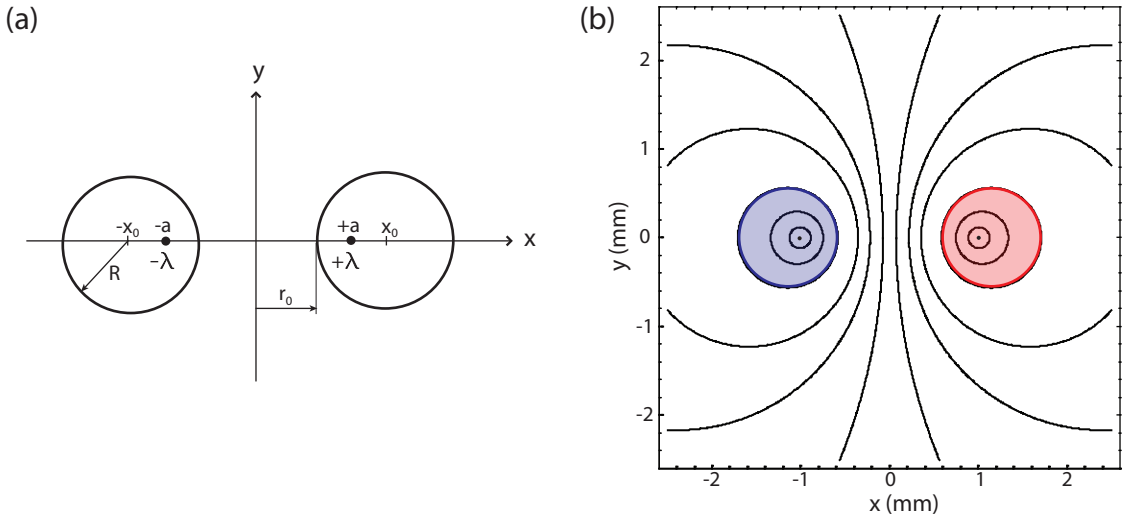

Figure 2.3: (a) The electrostatic potential for two oppositely charged cylinders can be determined by consideration of the electrostatic potential of two oppositely charged line charges, $\pm\lambda\,\mathrm{C/m}$, positioned at $x = \pm a$. (b) The equipotential surfaces of this potential are cylinders. Thus the electrostatic potential of two cylinders simply requires matching a given equipotential surface characterized by the line charge positions $\pm a$ to the radius (R), center positions ($\pm x_0$) and the applied voltage (V_0) of the cylindrical conductors.

2.3 The Electrostatic Field and the Forces Exerted on the Molecules

In our decelerator a single electrostatic lens is comprised of two oppositely charged cylindrical electrodes with hemispherical ends. The electrostatic field formed by these electrodes will defocus molecules in the plane of the electrodes whilst focusing in the other transverse plane. This geometry is particularly convenient as the transverse and longitudinal effects of the static electric field on the molecules can be approximately separated depending on where the molecules are: exactly between the electrodes, where the gradient of the electric field along the z–axis is zero, it is appropriate to consider only transverse forces, whilst for molecules in the fringe field the longitudinal gradient of the electric field is non–zero and deceleration is the dominant effect.

2.3.1 The Static Electric Field Between Two Long Conductors

We begin by considering the region of electrostatic field between the oppositely charged cylinders far from their ends. An analytical expression for the electrostatic field in this region is easily derived if we consider the combined electrostatic potential of two oppositely charged and infinitely long line charges. Figure (2.3) (a) shows these two line charges with charge densities $\pm\lambda\,\mathrm{C/m}$ and positioned at $x = \pm a$ respectively. The electric field given by the positive line charge only is $E_r = \lambda/(2\pi\epsilon_0 r)$ where $r = \sqrt{(x-a)^2 + y^2}$. By integration,

we find the potential difference between any point and the origin, for this line charge:

$$V_1(x,y) = V_1(0) + \frac{\lambda}{2\pi\epsilon_0} \ln\left[\frac{a}{\sqrt{(x-a)^2+y^2}}\right]. \tag{2.14}$$

Similarly the potential due to the negative line charge is

$$V_2(x,y) = V_2(0) - \frac{\lambda}{2\pi\epsilon_0} \ln\left[\frac{a}{\sqrt{(x+a)^2+y^2}}\right], \tag{2.15}$$

and since $V_1(0) = -V_2(0)$, we get for the combined potential

$$V(x,y) = \frac{\lambda}{4\pi\epsilon_0} \ln\left[\frac{(x+a)^2+y^2}{(x-a)^2+y^2}\right]. \tag{2.16}$$

Figure (2.3) (b) shows the equipotential lines (in black) derived from the total electrostatic potential. These curves are all circles and as both line charges extend to $\pm\infty$ along z–direction, the equipotential surfaces are cylindrical; close to the line charges the equipotential surfaces are centered on the line charges themselves, however as we move further away they become progressively centered away from the line charge positions. This is very convenient for us as we wish to determine the electric field of two oppositely charged cylinders, each having radius R and located at $x = \pm x_0$. As the conductor surfaces are, by definition equipotential surfaces, then we we are only required to find the line charge locations $\pm a$ which make this so.

It is more appropriate to cast the total electrostatic potential of Equation (2.16) in terms of the parameters of the experiment: the applied voltages to the conductors $\pm V_0$, the conductor radius R and conductor centers $\pm x_0$. This gives for the electrostatic potential:

$$V(x,y) = A \ln\left[\frac{(x+a)^2+y^2}{(x-a)^2+y^2}\right], \tag{2.17}$$

where the line charge locations are given by

$$a = \pm\sqrt{x_0^2 - R^2}, \tag{2.18}$$

and

$$A = \frac{V_0}{2\ln\left[\frac{R}{x_0-a}\right]}. \tag{2.19}$$

Thus knowing the applied voltages $\pm V_0$, conductor radius R and positions $\pm x_0$ completely determines the electrostatic potential $V(x,y)$.

As we wish to calculate the Stark shift of our molecules we need to know the electric field magnitude. The electric field $\mathbf{E}(x,y,z)$ is related to the electrostatic potential through $\mathbf{E}(x,y,z) = -\nabla V(x,y,z)$. In particular, the electric field magnitude for the two–dimensional

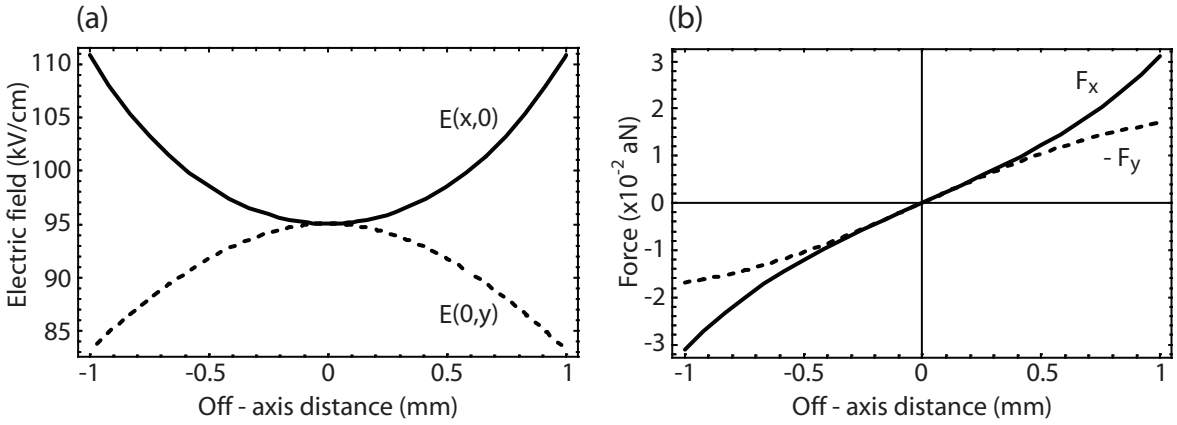

Figure 2.4: (a) The electric field magnitude along the x and y axes between two oppositely charged electrodes ($V_0 = \pm 10\,\mathrm{kV}$, $R = 3\,\mathrm{mm}$, $x_0 = \pm 4\,\mathrm{mm}$) lying in the xz-plane. (b) The force on the CaF molecule in the J=0 state along the x and y axes as a function of displacement from the beam axis. Note the sign of the force along the focusing y axis has been changed for ease of comparison with the x component of the force.

case is derived from the potential as

$$E(x,y) = \sqrt{\left(\frac{\partial V}{\partial x}\right)^2 + \left(\frac{\partial V}{\partial y}\right)^2} \tag{2.20}$$

which gives

$$E(x,y) = \frac{4A}{a}\left(1 - 2\frac{(x^2-y^2)}{a^2} + \frac{(x^2+y^2)^2}{a^4}\right)^{-1/2}. \tag{2.21}$$

This closed form solution for the magnitude of the electric field can be expanded in a Taylor series about the origin to reveal harmonic and higher order terms present in the real electric field,

$$E(x,y) \approx E_0\left(1 + \eta\frac{(x^2-y^2)}{r_0^2} + \eta^2\frac{(x^4+y^4-4x^2y^2)}{r_0^4}\right) \tag{2.22}$$

where $\eta = (x_0 - R)/(x_0 + R)$ and $E_0 = \frac{4A}{a}$. The force on the molecule is the gradient of the Stark shift. For the large electric fields we use in the experiments the Stark shift of our molecules is very nearly linear in the electric field magnitude. We write

$$W(x,y) = -\mu_{eff}E(x,y), \tag{2.23}$$

where μ_{eff} is a constant called the effective dipole moment which tends to μ, the molecular dipole moment, as the field becomes very large. In the approximation that the first two terms of Equation (2.22) dominate the expansion, the forces along the x–axis or y–axis are linear with respect to displacements from the molecular beam axis and have opposite signs

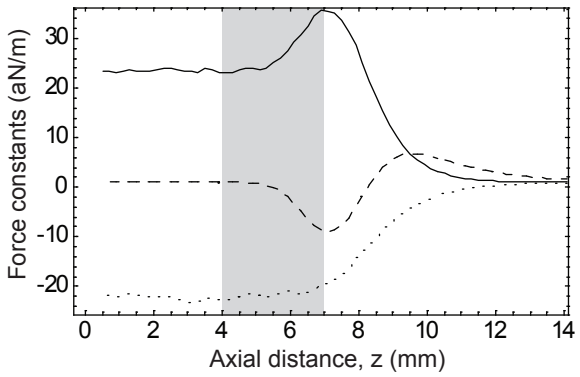

Figure 2.5: The axial variation of the force constants k_x, k_y and k_z for CaF in the J=0 state travelling through one stage of our decelerator; z =0 is at the centre of a lens. All the force constants are evaluated on the molecular beam axis and the applied voltages to the decelerator are ±10 kV. Full line: defocusing force constant $k_x = \partial F_x/\partial x$. Dotted line: focusing force constant $k_y = \partial F_y/\partial y$. Dashed line: axial force constant $k_z = \partial F_z/\partial z$.

as expected. The first two terms in the expansion of the electric field magnitude have the desired form but the full electric field includes higher order terms which produce focusing abberations. The relative magnitude of these terms is determined by the value of η: if the gap is much smaller than the electrode radius then η will be much less than one and the field will approximate well the desired harmonic field for all x, $y < r_0$. The actual electrodes have a radius R =3 mm and a half gap r_0 =1 mm which give η =1/7. Thus at a point $(x/r_0, y/r_0) = (1, 0)$ the contribution to the electric field from the first higher order term is 14% that of the harmonic term. Figure (2.4) shows the transverse forces exerted on a CaF molecule in the $J = 0$ state in the field given by Equation (2.21) with $V_0 = \pm 10$ kV, $R = 3$ mm and $x_0 = \pm 4$ mm. Close to the origin, both transverse forces have equal and opposite linear gradients. Further away from the origin, the non-linearity due to the higher order terms strengthens the defocusing power and the focussing is weakened.

2.3.2 Fringe Field of Two Finite Length Conductors

So far the electrodes have been assumed infinitely long. However the electrodes have finite length and the molecules necessarily move through the region where the electrodes terminate. We call this region of the electrostatic field the fringe field. Due to the complexity of the electric field in this region, it is calculated using a finite-element program FemLab v.4.0 [42]. This program is given the electrode geometry of a lens for which it then solves Laplace's equation on a three dimensional mesh with a typical resolution of 0.1 mm. Using the known Stark shift of the molecule, the Stark energy and forces are calculated on the same grid. Finally, differentiation of the force gives us the force constants. Figure (2.5) shows the variation of the force constants $k_x = \partial F_x/\partial x$, $k_y = \partial F_y/\partial y$ and $k_z = \partial F_z/\partial z$ evaluated on the beam axis

as we move from the centre of a lens to a point 14 mm away from it. The grey area marks the region where the hemispherical ends of the electrodes begin and end.

Starting from the left hand side of Figure (2.5), in the middle of the lens, the axial electric field is uniform and so there is no force along this direction, consequently k_z=0 (dashed line). As the transverse forces are equal and opposite in this region, then $k_x = -k_y$. We see from the full and dotted lines that indeed $k_x = -k_y$ =23 aNm. As the fringe region is approached the axial electric field is no longer uniform and there is an axial force that opposes the motion of the molecules, thus $k_z < 0$ and the sum $k_x + k_y$ is raised. The transverse forces are no longer equal and opposite and the increase in $k_x + k_y$ is brought about by an increase in the defocusing spring constant k_x which reaches its peak value at he exit of the lens. This peak value is almost twice as big as the focusing constant, and represents a very undesirable effect: it *kicks* molecules out of the beam line. As this repeats at each lens, this effect is a significant loss mechanism for molecules in the Stark decelerator as it kicks molecules out of the beam that would otherwise have undergone stable motion inside the decelerator. This effect is studied further in Chapter 5.

2.4 Transverse Motion of a Single Molecule

Let us consider a particle moving along the direction of the z–axis with velocity v_z and whose transverse position vector $\mathbf{r}$ at some axial location z has coordinates $\mathbf{r} = (x, y)$. We consider the transverse motion in a region of space where there is no axial gradient of electric field, so that the forces in the z–direction are zero. Under the action of only transverse forces that are linear with respect to displacements from the z–axis, the equation of motion for the particle is $m\ddot{\mathbf{r}} = \pm k\mathbf{r}$. It is convenient to rewrite these equations in terms of the position coordinate, z, rather than time:

$$\frac{\partial^2 x}{\partial z^2} - \kappa^2 x = 0, \tag{2.24a}$$

$$\frac{\partial^2 y}{\partial z^2} + \kappa^2 y = 0. \tag{2.24b}$$

The number of oscillations per unit length inside a lens is given by $\kappa/2\pi$ and is related to a force constant k by $\kappa = \sqrt{|k|/mv_z^2}$. The value of the κ is found from Equations (2.22) and (2.23)

$$\kappa = \sqrt{\frac{\mu_{eff}}{mv_z^2}\frac{2\eta E_0}{r_0^2}}. \tag{2.25}$$

The general solution to these differential equations is well known and can be written in

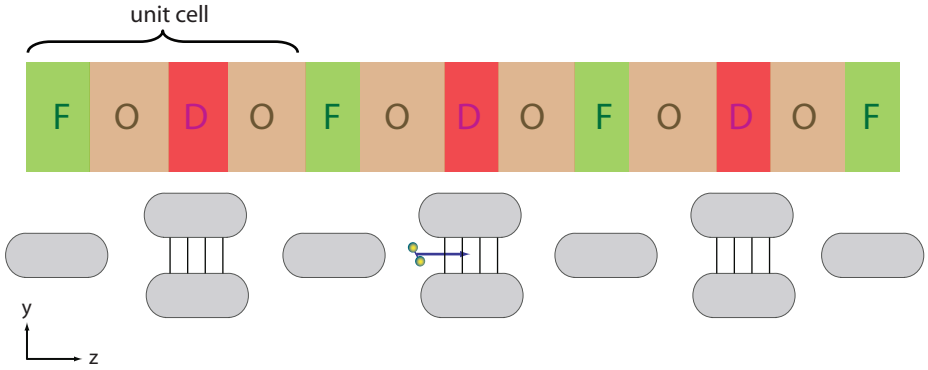

Figure 2.6: Alternating gradient decelerator as a periodic focusing system. The unit cell of this AG decelerator is mathematically described as the product of a focusing **F**, drift **O**, defocusing **D** and drift **O** matrices. The AG decelerator consists of N repeating **FODO** units, thus the transport matrix for the complete decelerator is $(\mathbf{FODO})^N$

matrix form as

$$\begin{pmatrix} x \\ v_x \end{pmatrix} = \begin{pmatrix} \cosh \kappa L & (1/\Omega) \sinh \kappa L \\ \Omega \sinh \kappa L & \cosh \kappa L \end{pmatrix} \begin{pmatrix} x_0 \\ v_{x0} \end{pmatrix} = \mathbf{D} \begin{pmatrix} x_0 \\ v_{x0} \end{pmatrix} \tag{2.26a}$$

$$\begin{pmatrix} y \\ v_y \end{pmatrix} = \begin{pmatrix} \cos \kappa L & (1/\Omega) \sin \kappa L \\ -\Omega \sin \kappa L & \cos \kappa L \end{pmatrix} \begin{pmatrix} y_0 \\ v_{y0} \end{pmatrix} = \mathbf{F} \begin{pmatrix} y_0 \\ v_{y0} \end{pmatrix}, \tag{2.26b}$$

where the defocusing, **D**, and focusing, **F**, matrices operate on the entrance orbit vectors (x_0, v_{x0}) and (y_0, v_{y0}) respectively and transform them to exit vectors (x, v_x) and (y, v_y). L is the length of the lens, and $\Omega = \kappa v_z$.

This matrix representation is very convenient as the full transport matrix for the decelerator can simply be written as the product of the individual lens matrices that make up the decelerator [43]. We will also need the drift matrix, **O**, that transports the molecules through the free space regions. For a drift length, s, it is given by

$$\mathbf{O} = \begin{pmatrix} 1 & s/v_z \\ 0 & 1 \end{pmatrix}. \tag{2.27}$$

The Stark decelerator is a system composed of identical repeating units or *cells*. For motion in the yz–plane, each cell is described by the matrix product **FODO**. This matrix product acts from right to left: an input orbit vector (y_0, v_{y0}) is transported first through a drift region, then through a defocusing lens, drifted once more and finally transported through a focusing lens resulting in an output orbit vector (y, v_y). This is repeated N times and thus the full transport matrix for the decelerator is $(\mathbf{FODO})^N$. A necessary condition for the transverse stability of orbits is derived when we ask that the elements of the matrix

$(\mathbf{FODO})^N$ remain finite when N is arbitrarily large. This stability criterion is

$$-2 < Tr(FODO) < +2. \tag{2.28}$$

This condition is necessary but not sufficient as this formalism so far allows for transverse displacements that are larger than the physical aperture of the electrostatic lenses.

The transfer matrix for one unit cell with length l_{cell} can be re–parameterized according to the formalism developed by E. D. Courant and H. S. Snyder to analyze the orbits of charged particles in accelerators that implemented the strong-focusing principle [33]. In this formalism, the transfer matrix of a unit cell is written

$$\mathbf{M}(z + l_{cell}|z) = \begin{pmatrix} \cos\Phi + \alpha\sin\Phi & \beta\sin\Phi \\ -\gamma\sin\Phi & \cos\Phi - \alpha\sin\Phi \end{pmatrix}, \tag{2.29}$$

where $\alpha(z)$, $\beta(z)$ and $\gamma(z)$ are z–dependent parameters with the same periodicity as the lattice and are known as the Courant–Snyder parameters. Φ is known as the phase advance per cell and is a constant. The Courant–Snyder parameters and the phase advance are related to one another through the following relations

$$\alpha(z) = -\frac{v_z}{2}\frac{d\beta(z)}{dz} \tag{2.30a}$$

$$\gamma(z) = \frac{1 + \alpha^2(z)}{\beta(z)} \tag{2.30b}$$

$$\Phi = \frac{1}{v_z}\int_z^{z+l_{cell}} \frac{1}{\beta(z')}dz'. \tag{2.30c}$$

Equation (2.30b) ensures that the matrix has unit determinant. A particularly useful aspect of this transfer matrix is that the matrix describing N units is identical with the single unit cell matrix but with Φ replaced by $N\Phi$ this time. The phase advance Φ in Equation (2.30c) is an integral taken over one complete period of the periodic function β and it is therefore independent of z. The stability criterion in Equation (2.28) is transformed to the condition that $-1 < \cos\Phi < +1$ and is satisfied when Φ is real.

The trajectory of a molecule moving through this ideal lattice is given by

$$x(z) = \sqrt{\beta(z)\epsilon_i}\cos\left(\phi(z) + \delta_i\right), \tag{2.31}$$

where ϵ_i and δ_i define the initial conditions of this particular molecule, and

$$\phi(z) = 1/v_z \int_0^z 1/\beta(z')dz'.$$

The motion given by Equation (2.31) is a product of two periodic functions; one with a wavelength given by l_{cell} and another with wavelength $2\pi l_{cell}/\Phi$. When $\Phi << 2\pi$ the first

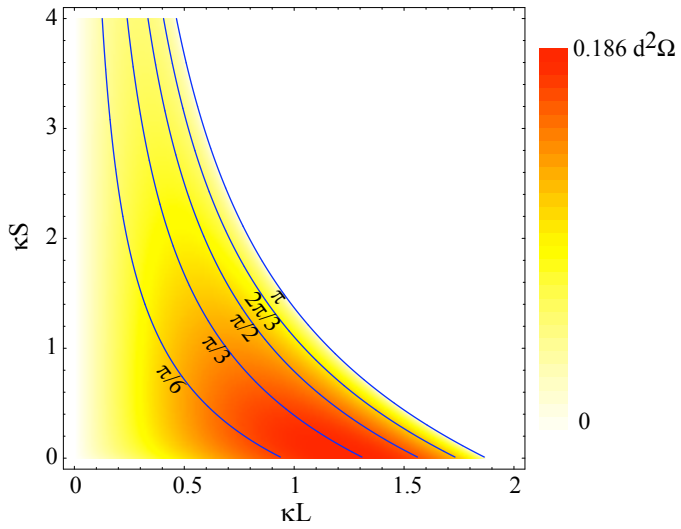

Figure 2.7: Transverse acceptance of a **FODO** lens array.

motion has a short wavelength and is called the micromotion, while the second has a much longer wavelength and is called the macromotion. This motion is identical to that of an ion in an RF trap.

Using the expression for $x(z)$ and the relations that hold between the Courant–Snyder parameters it can be shown that

$$\gamma(z)x^2 + 2\alpha(z)xv_x + \beta(z)v_x^2 = \epsilon_i. \tag{2.32}$$

This equation is identical to that of an ellipse and describes the distribution of molecular orbits with different δ_i but the same value of ϵ_i in the phase space whose coordinates are x and v_x. The shape of the ellipse varies periodically with z, but it's area $\pi\epsilon_i$ remains conserved. Further, if the molecular orbits' values of ϵ_i are distributed in the range $0 < \epsilon_i < \epsilon$ then these will describe a region in xv_x–phase space whose boundary is described by an ellipse and whose area is $\pi\epsilon$. Thus the value of ϵ defines the size of the beam in phase space and is called the emittance of the beam. Equation (2.32) tells us that the transverse displacements of a set of molecules lie within a beam envelope given by the periodic function $\pm\sqrt{\beta(z)\epsilon}$. The velocity spread lies with a beam envelope given by $\pm\sqrt{\gamma(z)\epsilon}$.

The spatial envelope can be used to calculate the transverse acceptance of a $(\mathbf{FODO})^N$ array. If we assume the array has a uniform aperture of size d along the entire length of the decelerator, then the transmittance of the array will be limited to a molecular beam whose envelope everywhere fits inside the aperture $\sqrt{\beta(z)\epsilon} < d/2$. The transverse acceptance is the phase space area occupied by the beam of largest emittance consistent with this criterion. This area is $\pi d^2/4\beta_{max}$. It can be shown that β is always a maximum in the middle of a focusing lens. Knowing this, we can calculate β_{max}, and so the transverse phase space

acceptance using the following procedure. We first calculate the transport matrix for one unit cell starting at the centre of a focusing lens $\mathbf{M} = \mathbf{F}(\frac{L}{2})\mathbf{O}(s)\mathbf{D}(L)\mathbf{O}(s)\mathbf{F}(\frac{L}{2})$. We obtain the value of the phase-advance per unit cell from the trace of the matrix: $\cos\Phi = \frac{1}{2}Tr(\mathbf{M})$. As shown by Equation (2.29) the upper-right hand side of $\mathbf{M}$ is $\beta\sin\Phi$ and since we know Φ, we have β_{max}.

Figure (2.7) shows the transverse acceptance calculated for the **FODO** lattice. The acceptance is plotted as a function of κL and κS, two dimensionless parameters that define the lattice. The acceptance is given in units of $d^2\Omega$ and the highest transverse acceptance is $0.186d^2\Omega$

2.5 Longitudinal Motion of a Single Molecule

The Stark decelerator consists of a series of electric field stages whose switching pattern is chosen in such a way as to decelerate pulses of molecules to rest. The switching pattern is chosen such that there is an ideal molecule that consistently arrives at the correct position between successive electrode pair stages at the time of switching. This molecule loses a constant amount of kinetic energy per electrode stage and is called the synchronous molecule.

The molecules in a pulse enter the decelerator with different velocities and so are at different positions relative to the electrodes at the time of switching. Do molecules close to the synchronous molecule remain nearby in the position-velocity phase space of the pulse? The answer to this question has been known for over 50 years in the acceleration of charged particles and is termed the Principle of Phase Stability. This says that particles near the ideal particle will remain nearby and in fact oscillate about the ideal particle. Accelerator physicists call these synchrotron oscillations.

To qualitatively illustrate this, let us consider the situation in which three molecules enter the decelerator in such a way that when the first pair of electrodes are switched they are at the same position. One of these is the synchronous molecule and by definition will always be at the same relative position at the time of switching the fields and thus will lose the same kinetic energy per stage. The other two however, have slightly higher and lower velocities. The faster molecule arrives at the next decelerating stage sooner and at the time of switching loses the greatest amount of kinetic energy; the opposite is true for the lagging molecule. After multiple occurrences of this sort, the leading molecule will begin to lag the synchronous molecule, whilst the lagging molecule will overtake it. This suggests that there is a region of stability. To develop the idea further a mathematical treatment is necessary.

The Stark decelerator consists of a series of electrode pair stages separated by a distance L. The longitudinal location, z, of a molecule at the time the fields are switched off dictates the amount of kinetic energy that it loses. It is convenient to parameterize this axial location in terms of a phase angle, χ, that has a periodicity of $2L$. The relation between them is given

by $\chi = (\pi/L)z$. The longitudinal velocity of a molecule is $v = \dot{z} = (L/\pi)\dot{\chi}$ where $\dot{z} = \partial z/\partial t$ and similarly for the phase angle χ. The field is switched at time intervals ΔT, which increase as the molecules are decelerated. As already mentioned the choice of switching pattern defines the synchronous molecule. By definition its position relative to the electrodes, z_0, is always the same at the time the fields are switched; the corresponding phase angle is labeled by $\chi_0 = (\pi/L)z_0$. The velocity of the synchronous molecule is indicated by the equilibrium velocity v_0.

The kinetic energy lost by the synchronous molecule per stage, $\Delta K(\chi_0)$, is given by $W(\chi) - W(\chi + \pi)$, where $W(\chi)$ is the potential energy, i.e. Stark shift, of the synchronous molecule in the electric field. It is convenient to expand $W(\chi)$ as a Fourier series. Molecules that are in maximum electric field just prior to the time that the fields are switched are assigned a phase angle $\chi = 90^o$. In this case an expansion in sine functions is most appropriate for $W(\chi)$. This results in

$$\Delta K(\chi) = \sum 2a_{2n+1} \sin{(2n+1)\chi}. \tag{2.33}$$

If the stages are well separated relative to the electrode pair aperture the potential will look like a square wave implying that the higher order terms in Equation (2.33) must be considered. On the other hand if the electrode pair aperture and the adjacent pair separation are similar then the potential will appear sinusoidal. This allows us to only consider the first term in the expansion, $\Delta K(\chi) = 2a_1 \sin\chi$. The maximum kinetic energy lost per stage is $2a_1$. It will be useful to express this instead as $q.(mv_i^2/2)$ where $mv_i^2/2$ is the initial kinetic energy of a molecule entering the decelerator and q^{-1} is interpreted as the minimum number of stages required to bring this molecule to rest.

If we assume that the deceleration is small i.e. that q is small, then we can say that the energy loss per stage is due to a constantly acting force of magnitude $\Delta K/L$. A simple application of Newton's Second Law gives us the equation of motion of a non-synchronous particle in terms of its phase angle

$$\frac{mL}{\pi}\ddot{\chi} - \frac{qmv_i^2}{2L}\sin\chi = 0. \tag{2.34}$$

Replacing χ with χ_0 reduces to the equation of motion for the synchronous molecule. It is more instructive to move into a coordinate system moving with the synchronous molecule and to track the motions of all other molecules relative to this one in this frame. Let us first define the relative phase, $\epsilon = \chi - \chi_0$, and the relative velocity, $h = v - v_0$. This allows us to write the equation of motion of a molecule with respect to the synchronous molecule. To eliminate the time derivatives we use the relationship between relative phase and relative velocity

$$\frac{d^2\epsilon}{dt^2} = \frac{\pi}{L}\frac{dh}{dt} = \left(\frac{\pi}{L}\right)^2 h\frac{dh}{d\epsilon}. \tag{2.35}$$

Thus the equation of motion of any molecule in the frame of the synchronous molecule is

$$h\frac{dh}{d\epsilon} + \frac{qv_i^2}{2\pi}\left[\sin\left(\epsilon + \chi_0\right) - \sin\chi_0\right] = 0. \tag{2.36}$$

Applying the small relative phase approximation, $\sin\left(\epsilon - \chi_0\right) - \sin\chi_0 \simeq \epsilon\cos\chi_0$, and integrating Equation (2.36) yields the relationship between the relative velocity and the relative phase

$$\frac{h^2}{2} - \frac{qv_i^2}{4\pi}\cos\chi_0\epsilon^2 = \frac{E}{m}. \tag{2.37}$$

This equation is an energy equation, where E is the total energy of a molecule and the first and second terms on the left hand side of Equation (2.37) are the kinetic and potential energy of a molecule relative to the synchronous molecule respectively. This equation describes a family of curves in h-$\epsilon-$space; each curve corresponds to a distinct yet constant value for the total energy. Given the initial relative velocity and relative phase of a molecule then Equation (2.37) can be used to plot phase space diagrams describing the oscillatory motion of a molecule's velocity and phase relative to the synchronous molecule's velocity and phase. Figure (2.8) shows phase space plots for the synchronous phase angles $\chi_0 = 0$, $\pi/6$ and $\pi/3$ radian.

The origin of the coordinate system in Figure (2.8) corresponds to the phase angle of the synchronous molecule, and it can be seen that within certain limits any other molecule may perform stable oscillations about this point indicated by the closed contours. As expected, a molecule with positive relative phase will lose more kinetic energy at the time the fields are switched thus reducing its relative velocity. Similarly, molecules lagging in phase relative to the synchronous molecule will lose less kinetic energy, thus the relative velocity will increase. In the limit of small relative phase, the stable orbits are ellipses and the motion can be approximated to that of a simple harmonic oscillator. By comparison of Equation (2.37) with the energy equation for a harmonic oscillator about the spatial point z_0: $\frac{1}{2}h^2 + \frac{1}{2}\omega^2(z - z_0)^2 = \frac{E}{m}$, we find the longitudinal oscillation frequency

$$\frac{\omega}{2\pi} = \sqrt{\frac{qv_i^2\cos\chi_0}{8\pi L^2}}. \tag{2.38}$$

This is 464 Hz for $\chi_0 = \pi/6$ radian, an initial velocity equal to $300\,\mathrm{ms}^{-1}$, $L = 12$ mm and $q = 0.01$.

It is evident from the phase stability diagrams in Figure (2.8) that there are two very different regions; one corresponds to bound motion characterized by closed contours and the other unbound motion for which the contours are not closed. The contour in phase space

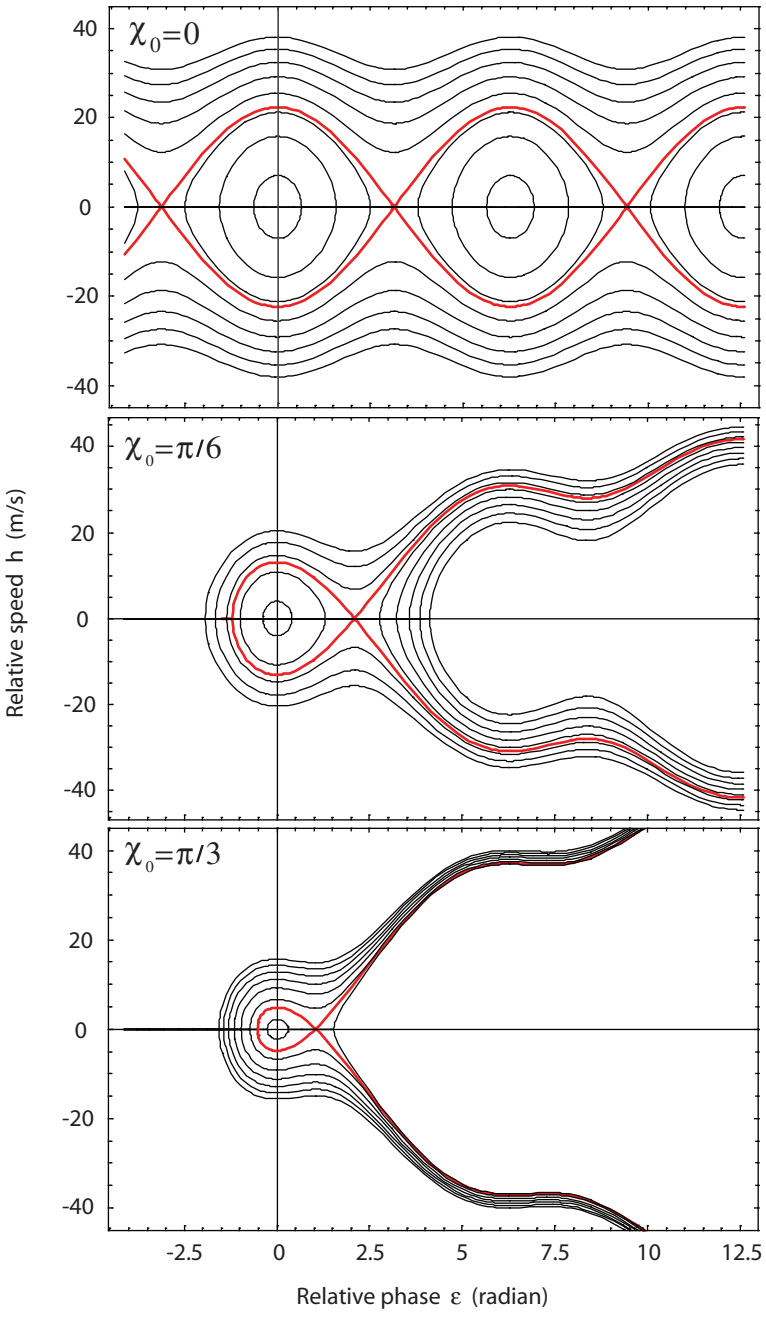

Figure 2.8: Longitudinal phase space of molecules for $\chi_0 = 0$, $\pi/6$ and $\pi/3$. The red curves are the separatrices and are the boundaries between the stable oscillations (closed contours) and the unstable or unbound motion (open contours). The phase space area inside the separatrix decreases as the synchronous phase angle increases.

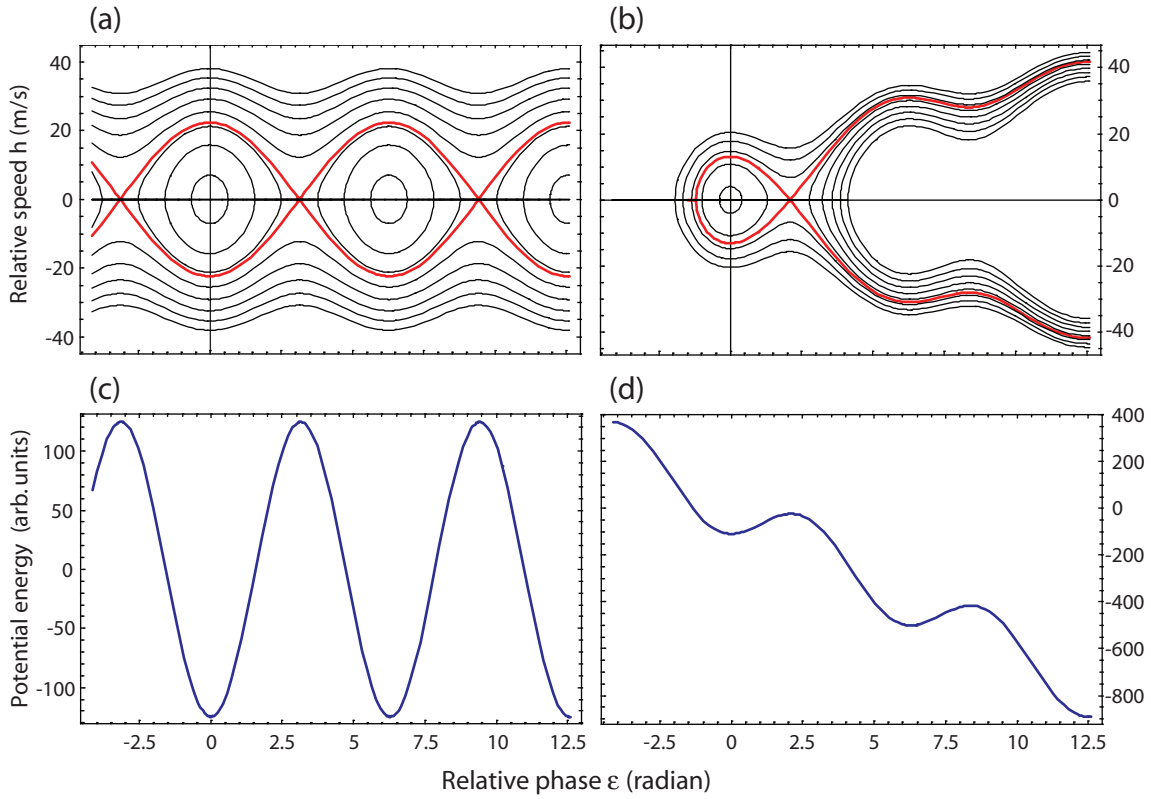

Figure 2.9: The longitudinal phase space and potential energy of the molecules for $\chi_0 = 0$ and $\chi_0 = \pi/6$. The equation of the separatrix defines the maximum total energy of molecules that will decelerate in accordance with the principle of phase stability. (a) $\chi_0 = 0$ radian, the separatrix is largest and (c) the potential energy bucket the molecules move in is deepest. (b) For higher synchronous phase $\chi_{=}\pi/6$ the area of the separatrix is reduced and (d) the potential energy bucket height is reduced. Thus fewer molecules are trapped.

which separates these two regions is called the separatrix and are shown in red in Figure (2.8). The size of the separatrix is dependent on the phase angle of the synchronous molecule: it is largest when $\chi = 0$ radian, the synchronous molecule loses no kinetic energy and thus it's velocity remains unchanged. The region of stable motion is large and admits molecules with relative velocities up to $\pm 22\,\mathrm{ms}^{-1}$ when they are at the same position as the synchronous molecule; and relative phases up to 2.5 radian (which is 8 mm when L=10 mm) when they are moving at the same velocity as the synchronous molecule. To decelerate the pulse we must increase the phase angle of the synchronous molecule. As this is done the region of bound motion decreases; for $\chi_0 = \pi/3$ radian only molecules with relative velocities up to $\pm 5\,\mathrm{ms}^{-1}$ and relative phases between -0.6 radian and 1 radian can perform stable motion in this region. For maximum loss of kinetic energy per stage we make $\chi_0 = \pi/2$ radian, but then no molecules are admitted.

The area enclosed by the separatrix is called the longitudinal acceptance of the decelerator. For particles with total energy less than that of the separatrix, the motion is bounded. The

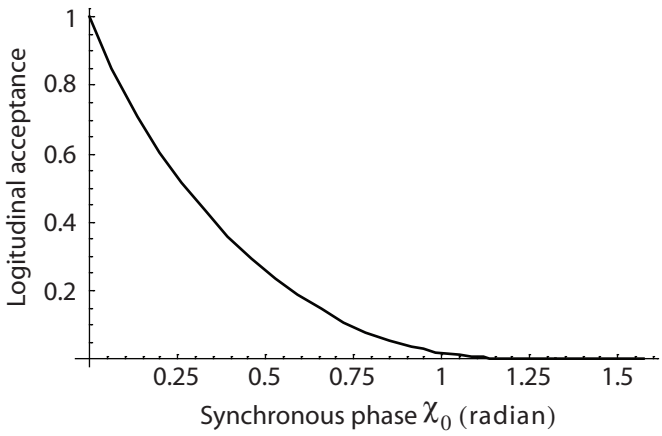

Figure 2.10: Longitudinal acceptance of the decelerator versus synchronous phase angle.

molecules move in an effective potential given by the second term on the right hand side of Equation (2.37). Figure (2.9) shows this potential energy as a function of ϵ, for two different phases, $\chi_0 = 0$ and $\chi_0 = \pi/6$. It is clear that molecules with total energies exceeding the height of the potential do not stay bound and that the equation of the separatrix corresponds to motion with total energy equal to the height of the potential barrier. The equation of the separatrix is given by

$$h = \pm\sqrt{\frac{kv_i^2}{\pi}\left[\cos\chi_0 + \cos\left(\epsilon + \chi_0\right) + \left(\epsilon - \pi + 2\chi_0\right)\sin\chi_0\right]}. \tag{2.39}$$

The positive and negative roots correspond to the upper and lower branches of the boundary. The longitudinal acceptance of the decelerator is calculated by integrating Equation (2.39), to find the area enclosed by the separatrix. Figure (2.10) is the result of this calculation for various values of χ_0 showing the acceptance decreasing as the synchronous phase increases.

The choice of synchronous phase angle clearly involves a compromise between the amount of deceleration we may require and the longitudinal spread in molecular positions and velocities that the decelerator will accept. A synchronous phase angle of $\pi/6$ radian results in 50% of the maximum possible reduction in kinetic energy and a longitudinal acceptance that is 24% of its possible maximum.

An important observation can be made concerning the dynamics of these molecules that is a consequence of Liouville's Theorem [44]. This theorem states that, following the motion a single molecule in phase space, the density of neighbouring molecules is constant. This in turn implies that trajectories in phase space do not cross because if they did their subsequent motion would be identical. Thus molecules whose motion corresponds to that within the separatrix will remain so throughout the entire deceleration process.

Chapter 3

Experimental Apparatus

This chapter describes the apparatus used for the creation of a molecular beam of the diatomic radicals, YbF and CaF. The laser systems employed for the subsequent detection of the molecules and how their frequency is controlled will be explained. This is then followed by a description of the Stark decelerator and its auxiliary equipment. Finally the chapter ends with a description of the computer infrastructure that orchestrates all this equipment.

3.1 The Pulsed Molecular Beam

This section describes the pulsed gas source and how this is combined with laser ablation to make a pulsed beam of the correct molecular species (a complete description of the characterization of the molecular source will be postponed until Chapter 4). First we deal with the vacuum environment necessary to maintain a beam over a length of several meters.

3.1.1 The Vacuum System

Figure (3.1) shows the stainless steel vacuum chambers that house the experiment. This set of chambers is split into two sections, the source and experiment chambers, separated by a gate valve and a conical skimmer with a 2 mm aperture. The chambers are each pumped by 300 l/s turbomolecular pumps, and the exhaust lines of each are backed by rotary pumps.

The pressure in the source chamber is monitored using a Penning gauge whilst that in the experiment chamber is measured using a Leybold Ionivac gauge which combines a Pirani measurement for pressures above 6×10^{-3} mbar and a hot cathode ionization measurement for pressures below 2×10^{-2} mbar. When there is no molecular beam the source chamber pressure is typically 1×10^{-7} mbar and the experiment chamber is at 8×10^{-8} mbar.

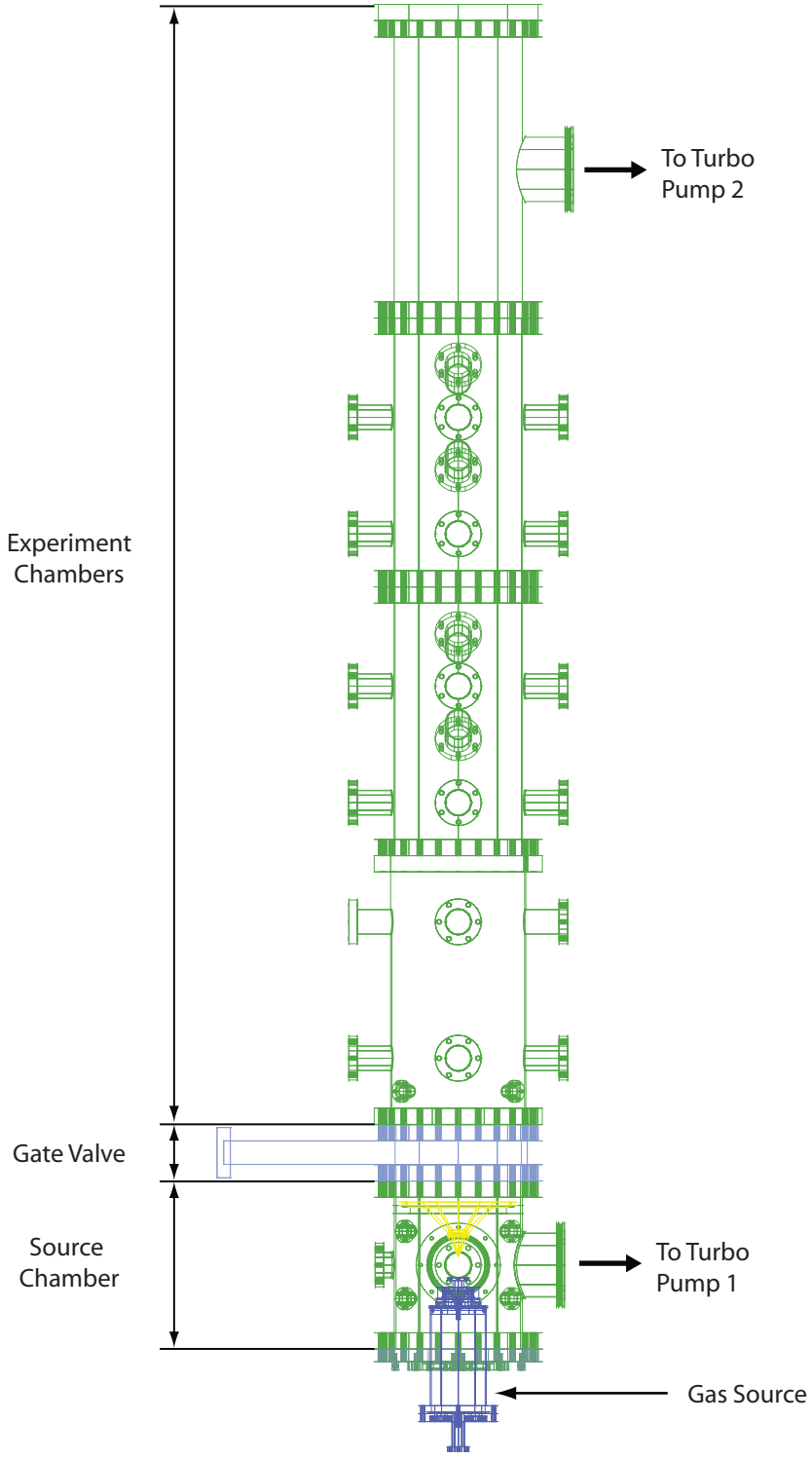

Figure 3.1: Wire frame model of the vacuum chambers that house the molecular beam source and Stark decelerator. The skimmer is shown in yellow outline.

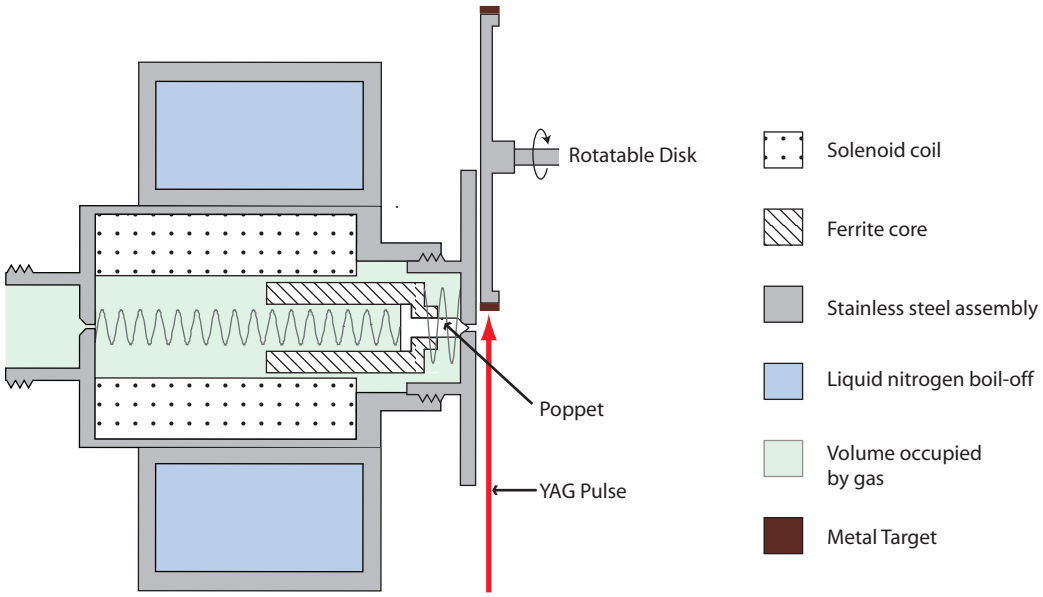

Figure 3.2: Schematic of the pulsed solenoid valve. A spring holds the poppet against the nozzle whilst a secondary spring ensures the poppet and ferrite core maintain contact with each other. A cooling jacket surrounds the solenoid valve and can be used to pre-cool the inert carrier gas using boil-off from a liquid nitrogen dewar.

3.1.2 The Pulsed Gas Source

Gas is released into the vacuum chamber using a pulsed solenoid valve (General Valve Series 9). Figure (3.2) shows a cross-section of this assembly. A teflon poppet, backed by a spring, seals against a short 1 mm diameter channel, known as the nozzle. This poppet sits within a ferrite core which gets pulled back when current is passed through the 50 Ω coil thus releasing gas into the source chamber.

The valve assembly is connected to a high pressure, 2-5 bar, gas line. This line is either sourced by a bottle containing argon and 2% SF_6 gas or by a mixing chamber in which a mix of either krypton or xenon with 2% sulfur hexafluoride gas is manually made.

Voltage is applied to the solenoid valve via a controller which receives trigger signals from the computer. The magnitude and duration of the applied voltage, and the pulse repetition rate all control how much gas is released into the source chamber. The latter two, duration and repetition rate, are controlled by the computer but are normally held fixed at 300 μs and 10 Hz respectively. This leaves the applied voltage which is manually adjusted to improve the molecular signal and is typically 280 V. Together these yield a time-averaged pressure of 1×10^{-4} mbar in the source chamber and 5×10^{-7} mbar in the experiment chamber when the valve is being pulsed.

The gas pulses are detected using a Beam Dynamics fast ionization gauge, placed 1120 mm downstream of the gas source with the detection area aligned to the molecular beam axis. The gauge has a 5 μs resolution enabling it to respond very rapidly to the locally varying pressure

as the carrier gas pulse passes through it. The resulting signal is a time of flight profile of the carrier gas and is primarily used to evaluate how well the gas source is aligned with the skimmer; maximizing this signal ensures good alignment. I refer the reader to Chapter 4 for a description of the optimization and characterization of the gas source.

3.1.3 Laser Ablation

The diatomic molecules of interest are made by laser ablation of either a Yb or Ca target close to the exit of the nozzle, see Figure (3.2).

A Q-Switched Nd:YAG laser is employed for the target ablation and is operated at the same repetition rate as the valve. The output pulses have a wavelength of 1064 nm, have a 10 ns duration and their energy can be varied up to 35 mJ using an in-built variable attenuator. The output is focussed and directed parallel to the face of the valve assembly and onto the rim of the circular target. The target is typically made into the form of a ribbon; 2 mm wide and with a depth of 1-2 mm, and is glued to the rim of a circular disk using Torr-seal.

The hot Yb/Ca atoms and ions resulting from the ablation are entrained in the gas expansion and react with the SF_6 molecules to form YbF or CaF. These molecules continue to expand and thermalize with the inert carrier gas. There is a variable delay between the Q-switch of the Nd:YAG laser and the opening of the valve and it is chosen such that ablation occurs when the carrier gas pulse is at its peak density over the target. The molecules continue 70 mm downstream when they pass through the 2 mm aperture of the skimmer into the experiment chambers.

3.2 Laser System

3.2.1 Basic Internal Layout and Operation

Two continuous wave ring dye lasers are employed to deliver light at 552 nm and 606 nm; a Coherent 899-21 running on R110 dye and a Coherent 699-29 running on R6G dye respectively deliver these wavelengths. They are pumped by an Innova 300C argon ion laser that lases on several lines in the blue-green region of the electromagnetic spectrum and with a typical output power of 7 W. With this pump beam power and after a fresh dye change both dye lasers typically output 200-300 mW.

Figure (3.3) shows a simplified diagram of the internal layout which is common to both dye lasers. The laser resonators have mirrors M1, M2, M3 and M4 arranged in a vertically folded ring geometry. One of the two counter-propagating travelling waves allowed by this geometry is removed using an optical diode. A birefringent filter provides coarse selection of the laser's cavity modes whilst a scannable thick etalon selects one particular mode and is actively locked to it by an electronic servo-loop. The thin etalon prevents mode hops that can occur between adjacent fringes of the thick etalon.

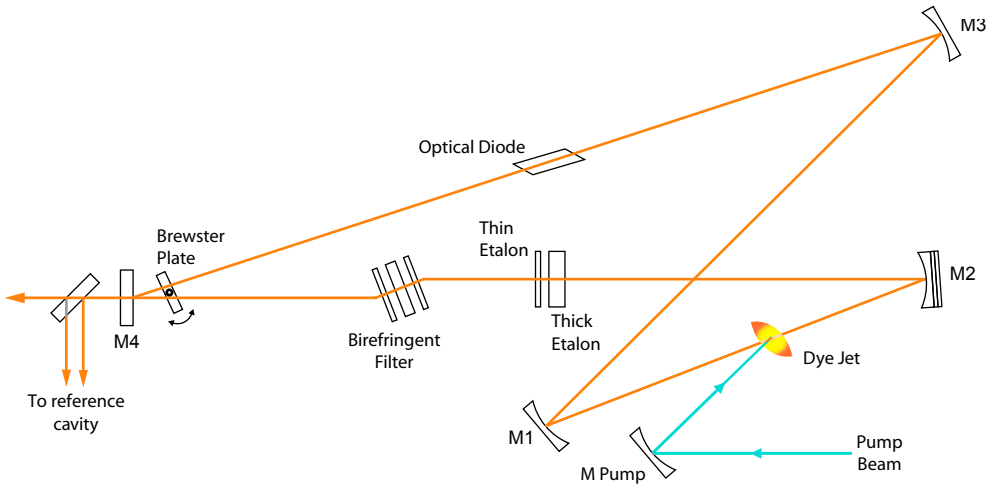

Figure 3.3: Schematic of the resonator geometry employed in the dye lasers.

As the length of the resonator dictates the frequency of the laser light, good length control is required for narrow-band operation. Each laser is equipped with a temperature-controlled, potted and hermetically sealed confocal Fabry-Pérot cavity and will be called the *reference cavity* from now on. Light picked off at the output of the laser is sent to the reference cavity and the transmission is monitored on a photodiode. Fluctuations in the frequency result in fluctuations in the voltage output from the photodiode. This voltage is used to generate an error signal that simultaneously drives the thick etalon, the Brewster plate and the piezo-stack mounted mirror, M2, in order to lock the laser frequency to the reference cavity.

Each laser is equipped with a control unit which is used to actively lock the laser's frequency to the side of a transmission fringe of the reference cavity. The control unit is also used to scan the laser frequency smoothly over several GHz by adjusting a tipping plate inside the reference cavity. At the back of the unit there is an input BNC line that allows the laser's frequency to be externally controlled. On application of a linear ramp in voltage from -5 V to +5 V applied at this point the laser will scan the full frequency range given by the value set by the user on the front of the control box.

Some of the lasers output is picked off and sent to a wave-meter, which allows correct tuning of the frequency to the desired value. Some of this light is also directed into an external home-built temperature and pressure stable cavity that enables us to monitor the change in frequency as the laser is scanned. The absolute frequency stability of the dye laser's own lock is rather poor and on a bad day is approximately 20 MHz/hr. In response to this we use the home-built stable cavity as a stable frequency discriminator in the frequency locking scheme, this will be explained more fully in Section 3.3.

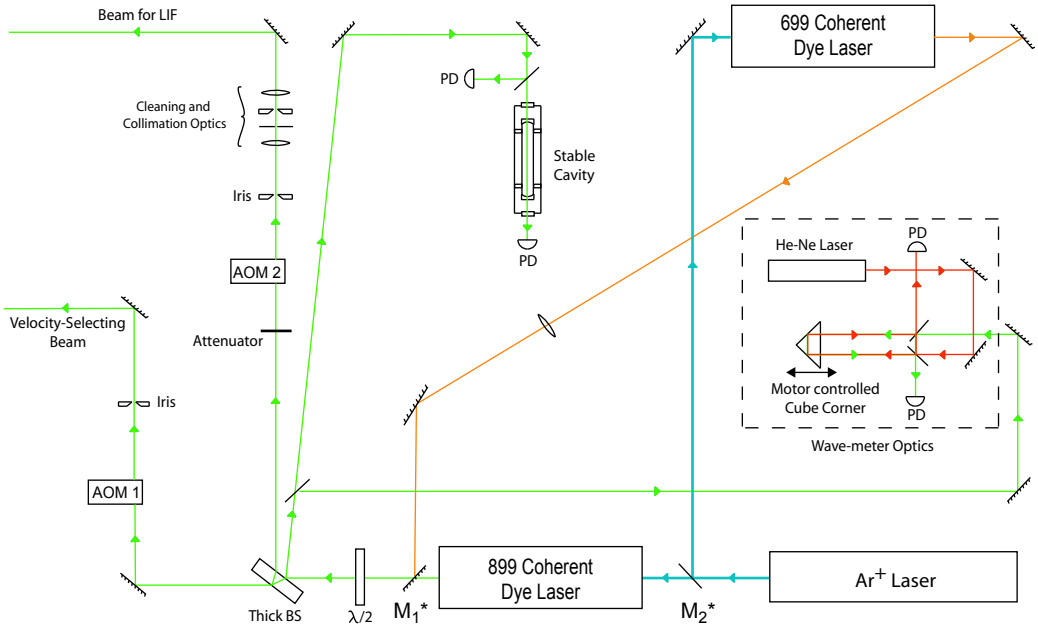

Figure 3.4: The optics table and equipment mounted on the optical table. The acronyms BS and PD stand for beam splitter and photo-detector respectively. $\lambda/2$ represents are half-wave plate.

3.2.2 Optical Table Layout

All the lasers and associated optics are mounted on a 1.5×3 m tapped optical table. Figure (3.4) shows a schematic of this equipment; following the output beam of the Coherent 899 dye laser we first encounter a half wave plate, ignoring the mirror $M_1{}^*$ for now. The wave plate is used to control the linear polarization of the beam coming out of the laser and is useful for minimizing the scatter of the LIF laser beam from the input window of the vacuum chamber. This will be explained further in Section 3.4.

Two beams are needed for manipulation of the YbF or CaF molecules: one is for velocity selection before the decelerator, and the other for the LIF detection after the decelerator. We pass the laser's output through a thick beam splitter and use two of the resulting beams for velocity selection and LIF detection. An added requirement is that we can independently control when these laser beams are incident on the molecules. To this effect, each beam passes through fixed frequency acousto-optic modulators (AOM) which are used as fast optical switches. Only the first order diffraction beam is used and it is shifted with respect to the input beam by 100 MHz, and into resonance with the Q(0) F=1 transition for both molecular species.

A suitably timed switching of AOM 1 can in this way select out the central section of the molecular pulse where the number density of the molecules is greatest resulting in a high density pulse with a reduced velocity spread. The output of AOM 2 passes through cleaning

and collimation optics before entering the vacuum chamber.

Also on the optical table is the stable cavity that is used in the frequency locking scheme mentioned in Section 3.2.1 and a home-built wave-meter that provides continuous real-time measurement of the laser's frequency. The wave-meter is based on a Michelson interferometer. The dye laser beam is split and made to follow two paths: one that goes straight to a photodiode and another that is retro-reflected by a moving corner cube. The latter beam interferes with the former and the changing path length results in interference fringes being detected by the photodiode. Similarly the beam from a stabilized helium-neon laser is made to follow the same path length and the subsequent interference fringes are measured on a second photodiode. Comparing the fringe frequencies of the two lasers determines the unknown laser frequency. A home-built microprocessor unit performs all these calculations automatically and displays the answer on a monitor.

As we have two dye lasers, that are not operated at the same time, a removable mirror, $M_2{}^*$, with a magnetic base is used to direct the argon ion beam from one laser to the other. Similarly another mirror, $M_1{}^*$, is used to make the output of the 699 dye laser follow the same path as the 899 laser beam.

3.3 Laser Frequency Locking

A versatile locking scheme is required to be able to stabilize to an arbitrary frequency within the visible range. A stable confocal cavity used in transmission as a frequency discriminator provides this flexibility. Figure (3.5) shows a schematic of the frequency measurement and control loop that is used to lock the frequency of the laser.

Scanning the frequency of the dye laser causes the intensity of the light transmitted through the stable cavity to periodically go through a series of intensity maxima and minima. The frequency separation between adjacent maxima, known as the free spectral range, is governed by the length of the cavity. By choosing the correct length for the cavity the transmitted output intensity will be half the maximum value for a given frequency of the laser. At this point the laser frequency is said to be on the side of a fringe. Keeping the cavity length fixed, variations in the intensity of the transmitted light correspond directly to variations in the laser's frequency. The output light intensity is measured using a photodiode circuit and its voltage output gives an electronic reading of these frequency variations. The transmitted light intensity is normalized to the input intensity to avoid converting variations in the input light intensity into frequency variations.

Servo electronics compare this voltage to a reference voltage, that corresponds to the required frequency, and from them derives an error signal which is passed back to the dye laser to correct the resonator's length, thus completing the feedback loop.

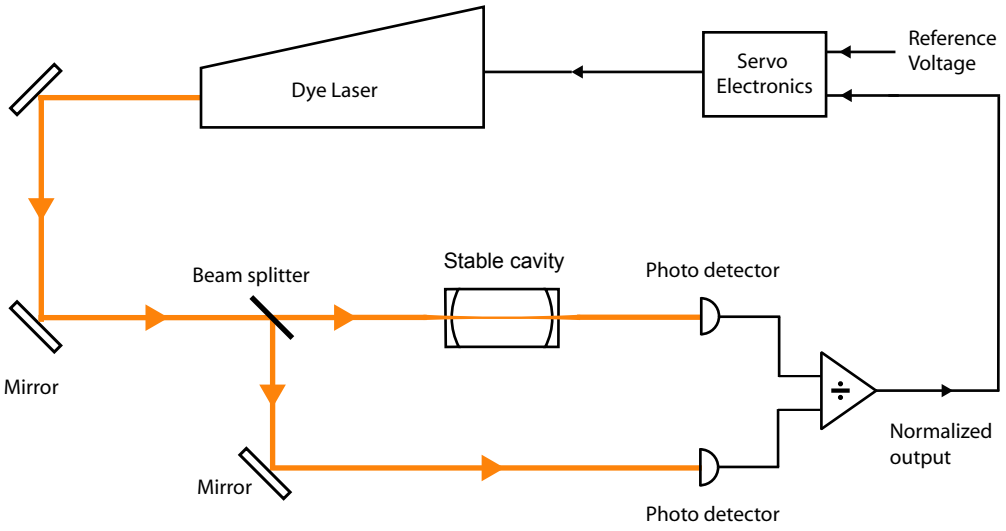

Figure 3.5: Schematic of the control loop for locking the laser's frequency. Light from the dye laser is passed through the stable cavity and the transmitted light intensity is detected by a photodiode circuit. Some of the light incident on the cavity is picked-off and detected using a separate photodiode circuit. The two photodiode circuits are then passed to a divider circuit. The voltage output from the divider circuit is a measure of the laser's frequency and is sent to servo electronics that control the laser's frequency. A separate voltage reference identifies the desired laser frequency. The subsequent error signal is used to correct laser's resonator length.

3.3.1 The Cavity

The cavity is formed by two identical spherical concave mirrors and they each have a radius of curvature of 10 cm. A hollow fused silica cylindrical spacer of length $\simeq$10 cm separates the two mirrors and provides the confocal arrangement. They are glued to the ends of the spacer using Torr-seal.

The key characteristics of a confocal cavity are it's free spectral range, ν_{FSR}, and it's finesse, F. The free spectral range is related to the length of the confocal cavity, L, by

$$\nu_{FSR} = \frac{c}{4L}. \tag{3.1}$$

It has a value of 750 MHz for a mirror separation of 10 cm. Figure (3.6) shows an example of the measured light intensity transmitted by the cavity when the laser frequency is scanned. The finesse, defined as the ratio of the free spectral range to the full width at half maximum of one of the transmission maxima is approximately 4.4. It is also related to the mirror reflectivity, R, through the relation

$$Finesse = \frac{\pi\sqrt{R}}{1-R} \tag{3.2}$$

Each mirror is coated with a layer of aluminium and silicon dioxide to protect against oxidation. The fringes shown in Figure 3.6 indicate a finesse of 4.4 and hence a mirror reflectivity

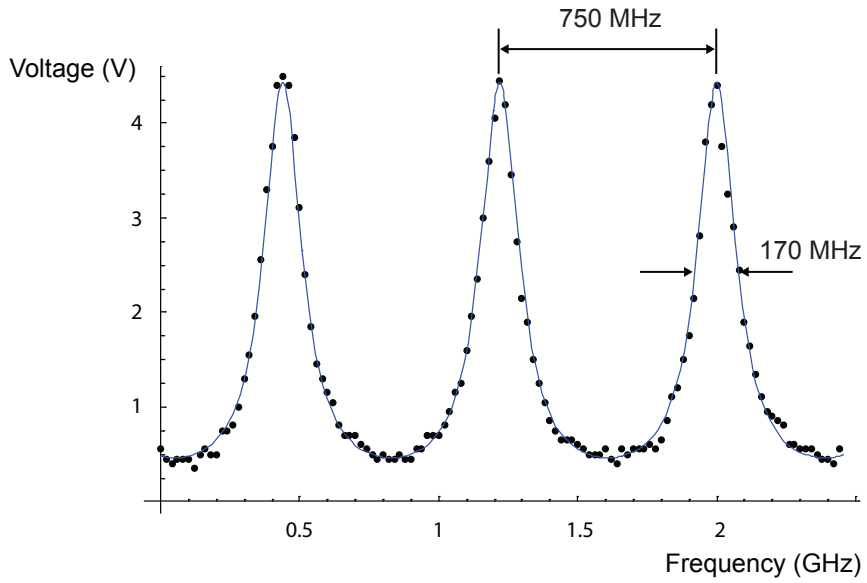

Figure 3.6: Measurement of the laser light transmission through the stable cavity as a function of the laser frequency (black points). The measured voltage corresponds to the light transmission normalized to the input light intensity. The blue curve is a fit of an Airy function to this data.

of 50%.

With the dye lasers locked to their reference cavities, frequency drifts of the order of several MHz/minute were observed. The line widths of the molecular transitions of interest are typically 20 MHz wide and so it would only take 5 to 10 minutes before the laser was completely off resonance. As the required frequency is locked to a point halfway up a transmission fringe of the stable cavity, an estimate of the gradient at that point is $2V_{max}/\Delta\nu$, where V_{max} is the voltage at the maximum transmission of the cavity and $\Delta\nu$=170 MHz is the full width at half maximum of the transmission fringes. Thus the slope at the lock point is approximately 50 mV/MHz and so a drift of 10 MHz shows up as a 0.5 V change in the output of the photodiode circuit.

For this technique to be useful it is important to actively control the optical path length. This ensures that the working frequency is located on the side of a fringe and that the absolute fringe position stays within acceptable bounds for the cavity to be considered a stable frequency reference.

3.3.2 Optical Path Length Control

The condition for maximum transmission of laser light through the confocal cavity is

$$N\lambda_0 = 4nL, \tag{3.3}$$

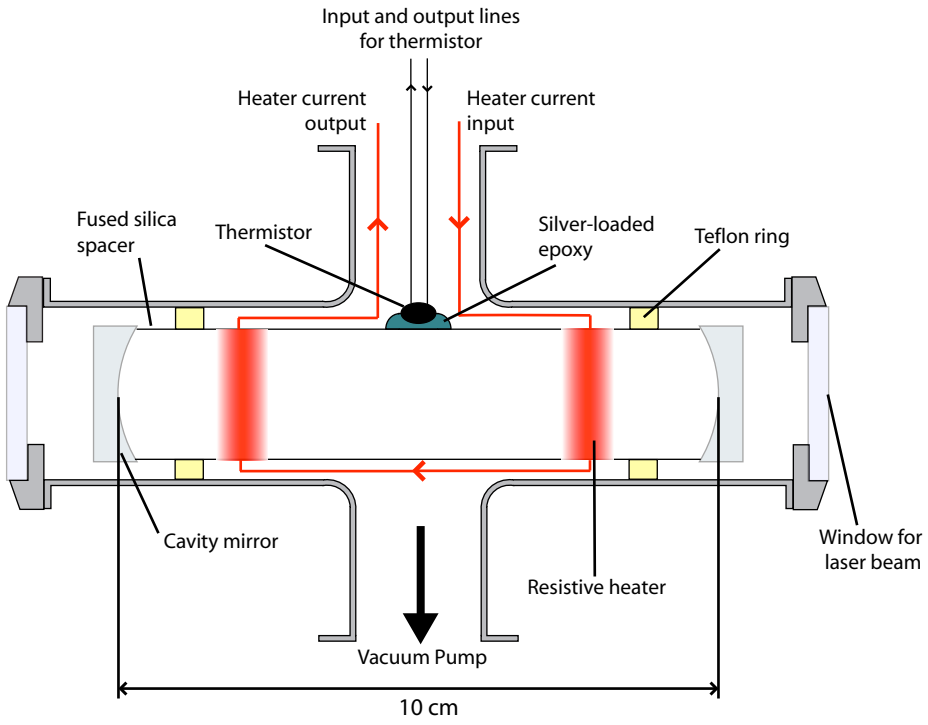

Figure 3.7: A diagram of the stabilized cavity and the KF four-way cross chamber that houses it. Two teflon rings hold the cavity inside the chamber. The chamber is capped off with 1" windows for optical access whilst the other two arms provide access to a vacuum pump and electrical feed-throughs for heater current delivery and temperature measurement.

where λ_0 is the vacuum wavelength of the laser light, L is the length of the cavity, n is the refractive index of the material between the mirrors and N is an integer.

To maintain a side-of-fringe lock both the physical length, L, and the refractive index, n, need to be controlled well. The length of the cavity is controlled by the thermal expansion of the silica spacer under the application of heat and the refractive index is controlled by placing the cavity in an evacuated chamber.

Physical Length Control

As shown in Figure (3.7), heat is applied to the cavity by passing current through two flexible strip resistive heaters, total resistance $160\,\Omega$, that are in series and in thermal contact with the spacer. The temperature is measured using a bead-in-glass thermistor which is glued to the outer wall of the spacer using silver loaded epoxy and is placed midway between the mirrors and heaters.

The thermistor's resistance is a function of its temperature, $R(T)$. The resistance at temperature T is measured using Stanford Research Systems SIM923A temperature monitor. This passes a stable 10μA through the lead wires connected to the thermistor. The voltage

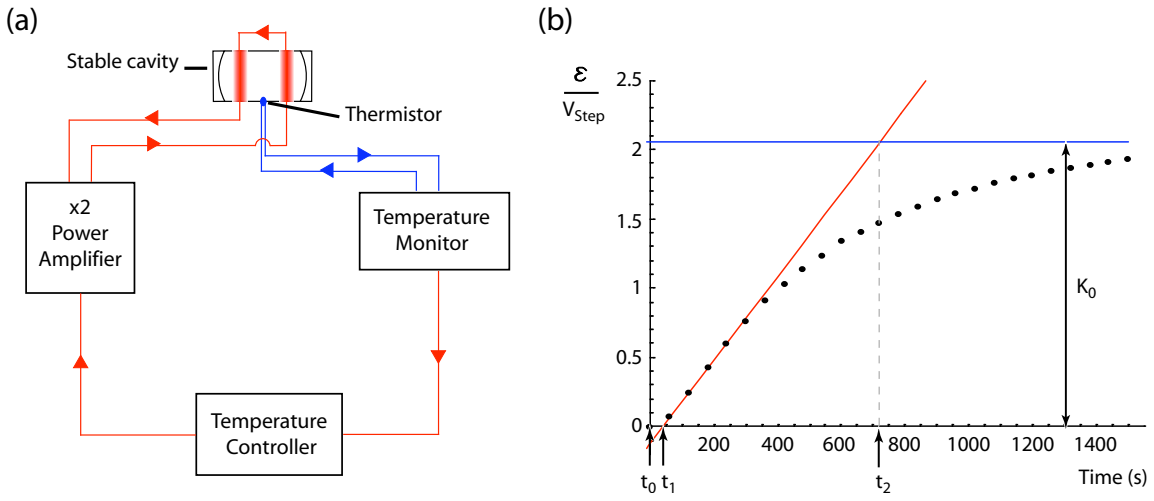

Figure 3.8: (a) The temperature control loop for the stable cavity. (b) The open-loop scaled response of the cavity temperature to an 8 V step change across the heater coils as a function of time. Straight line fits to the response curve for short times (red) and its asymptotic long time behaviour (blue) determine the proportional, integral and derivative gains.

developed across the sensor and the lead wires, $V_{Th} = iR(T)$, is a measure of the resistance and hence temperature of the thermistor. A calibration of the thermistor's resistance, R in Ohms, versus temperature, T in degrees centigrade, yielded the relation

$$R = \frac{4.25 \times 10^6}{T^{1.4}}. \tag{3.4}$$

The SIM923A uses this calibration to calculate and display the correct temperature on the front of the unit. The output consists of the measured voltage and this is fed directly to an analog Stanford Research Systems PID controller (SIM960). The temperature control loop is shown in Figure (3.8) (a). The gain values are: proportional P=9.2, integral I=0.01 s^{-1} and derivative D=21.5 s. These are entered on the front interface of the SIM960. The output of the PID box is then fed to a $\times 2$ power amplifier which drives current through the heating resistors wound around the cavity spacer.

The values for P, I and D were determined from a measurement of the open-loop response of the cavity temperature, to a step change in the voltage V_{Step}=8 V across the heater coils as a function of the time elapsed from the step change. The SIM960 PID box measures the error signal, $\epsilon = \beta(T - T_{sp})$ where the temperature set point T_{sp}=303 K and the proportionality constant β=1 V/K. Figure (3.8) (b) shows the scaled response, ϵ/V_{Step}, as a function of time. The response is characterized by its short-time behaviour, given by the red straight line fit, and it's behaviour at long times, shown by the blue asymptote line. The asymptotic behaviour of the response curve was found by fitting a nonlinear function to the data, which gave an estimate of the asymptotic value for the scaled response, K_0. The initial response time, t_0, measures the time elapsed during which the response is zero. The start and end

of the response are given by t_1 and t_2, where t_1 is the t-intercept value of the red line and t_2 is the time where the red line intercepts the blue asymptote line. These values are t_0=0, t_1=43 s, t_2=720 s and K_0=2.06. These are then used to find the values for P, I and D using the following relations

$$P = \frac{1.2(t_2 - t_1)}{K_0(t_1 - t_0)}, \tag{3.5a}$$

$$I = \frac{1}{2(t_1 - t_0)}, \tag{3.5b}$$

$$D = \frac{t_1 - t_0}{2}. \tag{3.5c}$$

The reader is referred to [45] for a description of this procedure. With the mentioned values for P, I and D, the temperature and hence length stability of the cavity is determined by scanning the laser frequency and comparing the maximum transmission frequency of the stable cavity to the known molecular transition frequency, with the temperature control loop closed. Figure (3.9) shows these measurements repeated over a total period of 7 hours where the ordinate values have been arbitrarily offset to roughly coincide with 0 MHz. The excellent 4 MHz peak-to-peak frequency variations observed in the first 150 minutes are very encouraging as this is much smaller than the line width of the molecular transition which is roughly 20 MHz. Using the relation, $\Delta \mathrm{L} = L(\Delta\nu\lambda/c)$, we find for L=10 cm, λ=552 nm, that a 4 MHz frequency stability corresponds to length stability of 0.7 nm. As the fractional length change per degree Kelvin has been measured to be $\frac{\Delta L/L}{\Delta T}$=$7\times10^{-7}$, then the expected temperature stability ΔT is 11 mK. This is certainly sufficient for the requirements of experiments with the Stark decelerator. Furthermore the larger frequency deviations, observed after 200 minutes, fluctuate about the average observed frequency, indicating that the temperature control loop is correcting the cavity length as it should.

When the laser frequency is locked to the molecular transition, the cavity length is first checked so that the molecular transition frequency is half way up a transmission maximum of the stable cavity. If not, the temperature set point in the temperature control loop is adjusted for this. The cavity typically requires approximately 30 minutes to stabilize to the new temperature, after which the frequency fluctuations are of the order of ≈10 MHz.

Refractive Index Control

Air between the cavity mirrors dictates the refractive index and changes in its value due to pressure changes will also affect the stability of the cavity as a frequency reference. The pressure dependence of the refractive index of air [46] can be found to be $(n-1) = 3.53 \times 10^{-7}P$, where n is the refractive index of air and P is the air pressure in Torr. The output frequency stability of the cavity, $\Delta\nu$, is related to a pressure change, ΔP, through the relation $\Delta\nu = \nu\Delta P(3.53\times10^{-7})$. The chamber is evacuated by a mechanical pump and is continuously

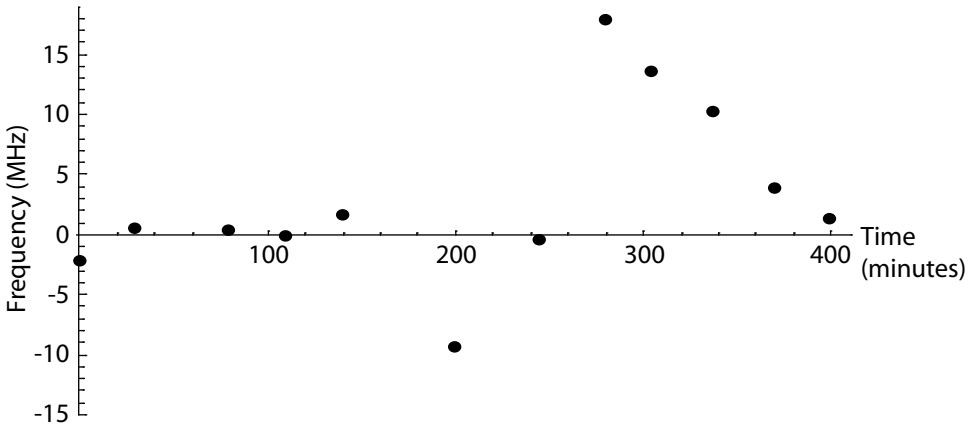

Figure 3.9: Performance of the temperature control lock. The length and hence frequency stability of the stable cavity is calculated by measuring the frequency separation of the molecular detection transition and one of the transmission maxima of the stable cavity.

pumped giving a pressure of 44 ± 1 mTorr. Thus a pressure stability of 1 mTorr implies the frequency stability of 0.2 MHz, for λ=552 nm, again easily within the margins of our stability requirements.

3.3.3 Locking the laser

With the cavity now suitably stable to provide an accurate frequency reference and the ability to change the cavity length for different frequencies, we need to lock the laser.

A separate stable voltage reference source is used to control the dye laser's resonator length. This voltage is manually scanned until the laser's frequency is resonant with the molecular transition. This voltage value is the frequency reference. At this point, the transmission of the stable cavity is half the maximum transmitted intensity, i.e. on the side of a fringe. The normalized photo-detector voltage serves as the real-time measure of the laser's frequency whilst the reference voltage is the desired value. A software-based electronic servo implements PID control of the error signal of these two voltages and provides a frequency stability that is equal to the cavity length stability $\simeq \pm 3.4$ MHz over a period of 1 hour.

3.4 Laser Induced Fluorescence Detection

The molecular beam is detected by the spontaneous emission the molecules emit upon excitation by resonant laser light. The laser is tuned to the correct wavelength to excite the transition connecting the ro-vibrational electronic ground state to the first excited electronic state. A discussion of the spectroscopy of CaF will be given in Chapter 4. The spontaneous emission is collected by intra-vacuum optics that focus the fluorescence onto the active area of a photomultiplier tube (PMT).

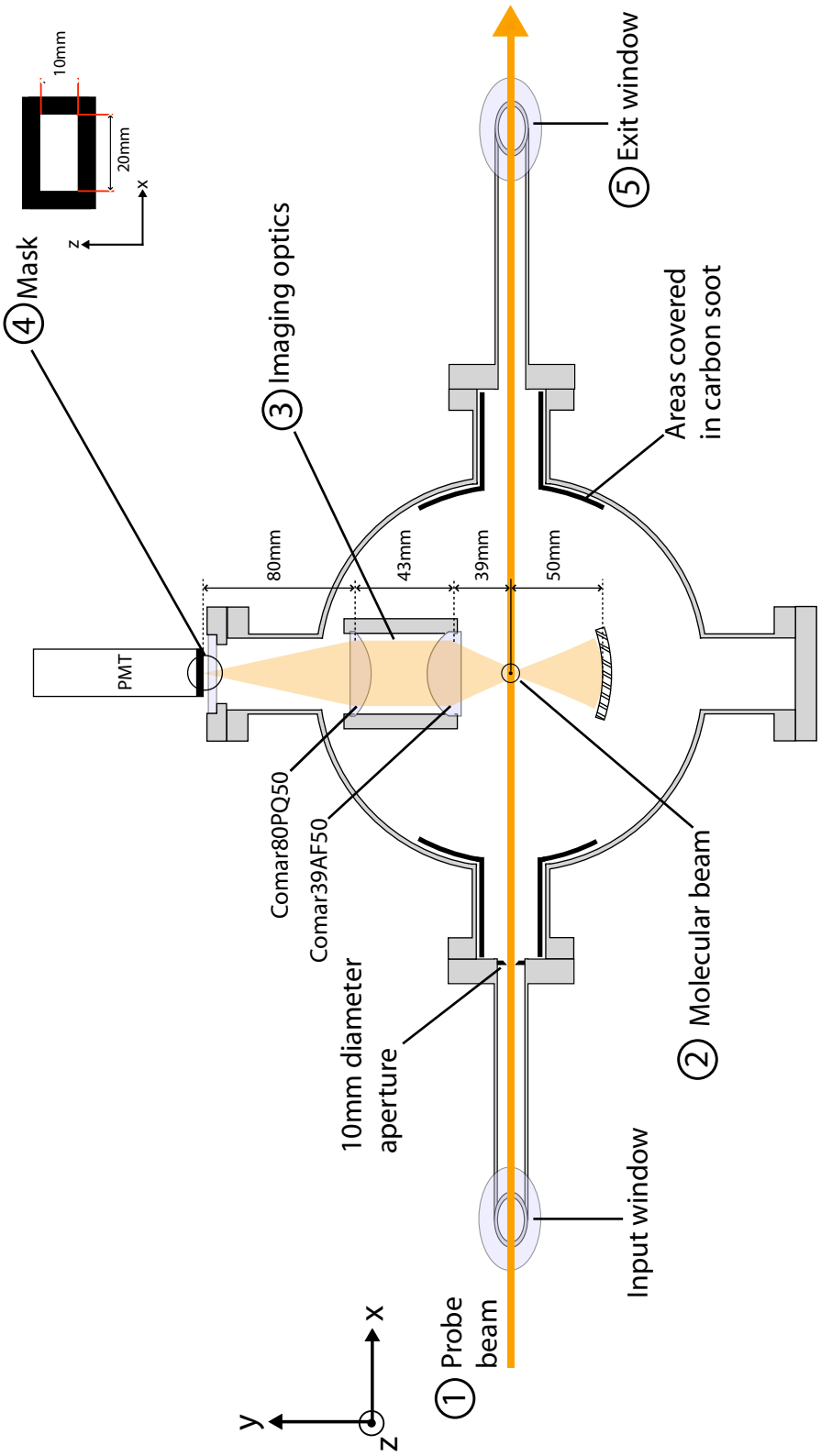

Figure 3.10: The laser induced fluorescence set up. 1. The probe beam enters the vacuum chamber through the input window. 2. The probe beam intersects the molecular beam (directed out of the page) below the LIF optics. 3. The LIF optics and a spherical mirror collect and focus the fluorescence onto the face of the PMT which is masked. 4. The mask helps reduce the contribution of background scattered laser light to the PMT signal. 5. The probe beam continues past the molecular beam and exits through the exit window.

3.4.1 Layout and Optics for Fluorescence Collection

The probe beam is shaped to provide a top-hat-like illumination of the molecular beam. To get the correct profile, the beam is expanded and collimated by a pair of cylindrical lenses. The center of the resultant elliptically shaped beam is then chopped using two rectangular apertures which pass only the central portion of the laser beam. This results in a beam with an approximately flat intensity profile in the yz–plane shown in Figure (3.10) and whose dimensions are 8×4 mm along the y and z directions respectively.

Figure (3.10) shows a plan view of the detection apparatus and setup. The probe beam enters the vacuum chamber through a glass window mounted at Brewster's angle. This beam then crosses the molecular beam axis at right angles to it and 894mm downstream of the molecular beam source.

The laser induced fluorescence is collected through optics that sit above the point of intersection of the laser and molecular beams. An aspheric lens (Comar39AF50) with a focal length of 39 mm collimates the fluorescence light. A second lens (Comar80PQ50) with a focal length of 80 mm focusses the collimated fluorescence light onto the face of an externally mounted photo-multiplier tube whose face is masked by a 20×10 mm aperture in the xz–plane. The lower aspheric lens is located 1 focal length above the molecular beam (39 mm) whilst the upper lens brings the fluorescence to a focus 1 focal length away from it (80 mm) onto the PMT face; thus the transverse magnification factor of this double lens combination is 2 and the effective active area of the photo-multiplier tube corresponds to a 10×5mm area in the plane defined by the laser beam and the molecular beam respectively. This effective aperture easily accommodates the probe beam which is 4mm wide along the direction of the molecular beam.

The intersection of the molecular and laser beams also sits at the centre of radius of curvature of a spherical mirror. The fluorescence retro-reflected by the mirror enhances the amount of spontaneous emission detected by the PMT. The lenses and mirror all have a diameter of 50 mm. The ratio of the total solid angle of detection (optics + mirror) to the full spherical solid angle is 0.16.

The fluorescence emitted by the molecules has the same wavelength as that of the exciting light. The Hamamatsu R374 PMT that is used has a photocathode efficiency of 10% at 550nm and 7% at 600nm. Together with the solid angle ratio and the 80% transmission of light through the optics (20% reflection losses from the six optical interfaces), the overall efficiency for the detector is $0.16\times0.1\times0.8=1\%$.

The probe beam exits the vacuum chamber through another arm with a window again set at Brewster's angle. This maximizes the transmission of light through the window and thus minimizes the level of scattered laser light back in to the vacuum chamber. The exit arm and window are surrounded by a matt black material that prevents room light from entering the chamber and acts as a beam dump for the exiting laser beam.

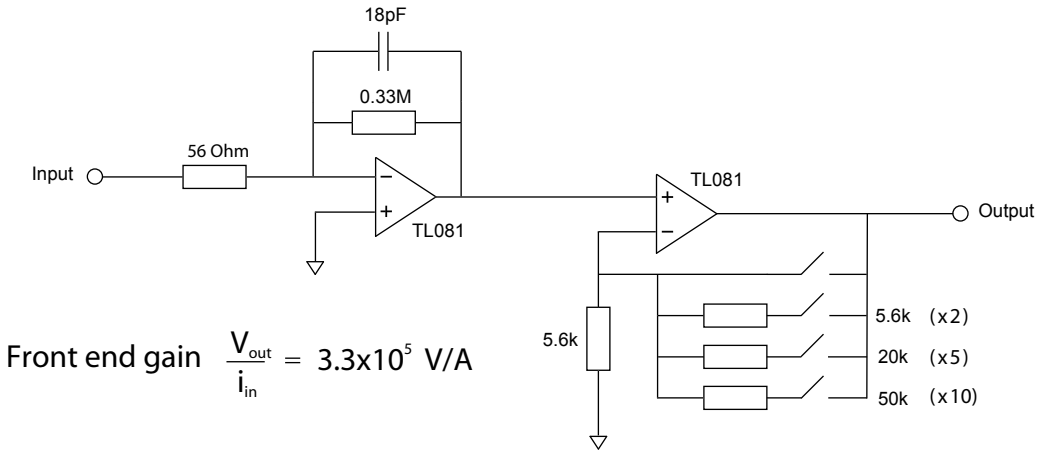

Figure 3.11: The PMT Amplifier Circuit.

3.4.2 The PMT Amplifier

The PMT can be operated in either: current mode, whereby the PMT's output current is proportional to the detected photon count rate; or in pulse counting mode, whereby single photon detection events are counted. For all the data presented in this thesis the PMT is operated in current mode.

The PMT's anode outputs bunches of electrons. Each bunch is the result of secondary emission induced by the detection of a single photon and subsequent release of a photo-electron at the cathode. This current is converted to a voltage and amplified by the circuit shown in Figure (3.11). The voltage developed across the $56\,\Omega$ resistor is inverted and amplified by the first TL081 Op-Amp stage with a time constant of $6\,\mu$s. The second and final Op-Amp stage provides a user-controlled voltage amplification and the total transimpedance gain of this circuit is 3.3×10^6 V/A for the $\times 10$ setting.

The amplifier is calibrated by allowing the probe beam to pass through the vacuum chamber and manually varying the power in the probe beam using a variable attenuator. For a series of different fluorescence powers the voltage output of the amplifier is recorded whilst in current mode and then, keeping the probe beam power constant, running the PMT in photon counting mode and recording the detected photon count rate. For $\times 10$ gain, a straight line fit to this data yielded the calibration curve $R = 1.5V + 0.003$ where R is the detected photon rate in kilo-Hertz and V the amplifier output voltage in milli-Volts. Figure (3.12) shows an LIF scan of the Q(0) region of CaF showing both F=1 and F=0 hyperfine components. Thus a signal voltage of 82 mV when resonant on the F=1 component corresponds to a photon rate of 126kHz.

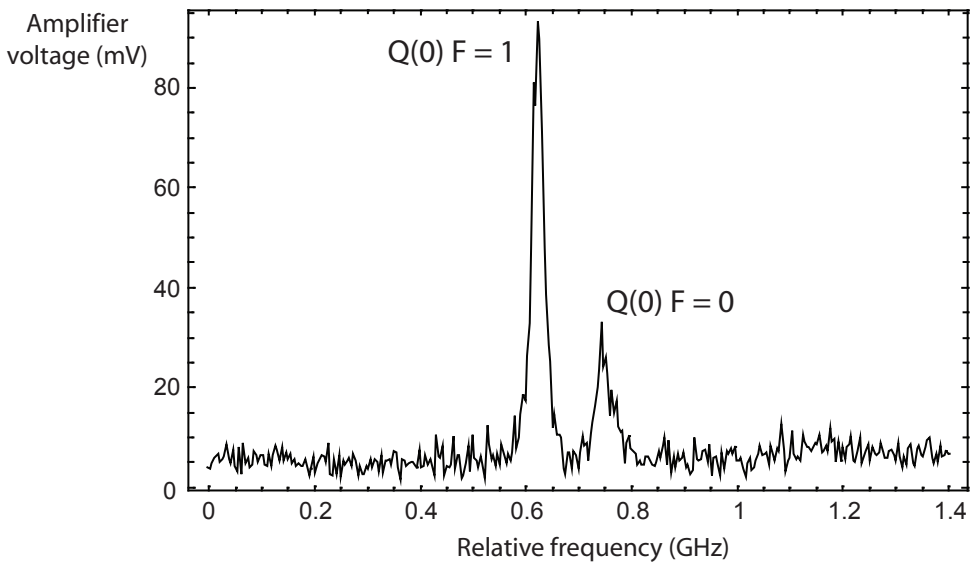

Figure 3.12: LIF spectrum of CaF showing the F=0 and F=1 hyperfine components of the Q(0) transition.

3.4.3 Background Scatter

In our experiments the background seen on the PMT output is almost completely due to either scatter of the laser beam light or room light leaking in through the windows.

Nearly all of the contribution from room light is through the exit window when uncovered. A mat black cloth material that completely covers the exit arm and window prevents room light from entering and serves as a beam dump for the exiting laser beam. This allows the experiment to be operated under full room lighting.

Reflection, and thus scatter, of the probe beam from either input or exit windows is minimized by using a half-wave plate to align the probe beam's polarization direction perpendicular to the plane of the window surface which is set at Brewster's angle. Diffraction of the probe beam by the optics and apertures used to give it the desired profile also contribute to the detected laser scatter. Some of the diffraction is removed using rectangular apertures before the beam enters the vacuum chamber. Any remaining stray light is blocked by a 10 mm diameter aperture inside the input arm of the chamber and absorbed by areas covered in carbon soot, refer to Figure (3.10).

The following breakdown of the contributions to the background is typical for the day to day running of the experiment: the dark count rate contributes 3 kHz; the room lighting contributes 10 kHz and finally with an the input probe beam power of 0.5mW the background due to laser scatter is less than 20 kHz. Thus the total background scatter is approximately 30 kHz.

3.5 The Electrodynamic Guide and Decelerator Apparatus

3.5.1 The Stark Decelerator

Figure (3.13) shows a plan view and photograph of the decelerator. It is a stainless steel structure composed of 21 electrostatic lenses. Each lens is formed by a pair of hemispherically-capped cylindrical electrodes, 6 mm in diameter and 14 mm long, separated by a 2 mm gap. As explained in Chapter 2 proper control over the molecules is achieved by having the plane of adjacent lenses alternate by 90° with respect to each other. The distance between the midpoint of one lens and the next is 24 mm.

All the electrodes are attached to four long rods as is seen in Figure (3.13). Each electrode is in electrical contact with a given rod via two metal dowels. These dowels are pressed into blind flat-bottomed holes drilled into each electrode and then the electrode and dowel sub-assembly is pushed into through-holes drilled into the rod. Each electrode and dowel sub-assembly is pushed a distance that compensates for the intrinsic bend of the given rod at that location.

During operation the horizontal and vertical rods are alternately charged; one set is charged whilst the other is held at ground and vice versa. The bottom and top rods (or left and right rods) are charged with equal and opposite polarity. Each rod is charged via a high voltage feed-through with a spring loaded end tip on the vacuum side. Each rod has a metal collar with a dimple drilled into it which can be placed at the correct point along the length of the rod to match the location of the spring loaded end and hold it securely in the dimple. The rods are supported using two macor ceramic rods connected close to the ends of each rod as shown in Figure (3.13). As the the decelerator is typically operated at ±15kV these macor rods also insulate it from the rest of the vacuum setup. This results in a set of four macor rods forming a cross shape at either end of the decelerator. Each set is held by a stainless steel ring, known as an earth ring, and is also shown in Figure (3.13).

The decelerator sits inside the support structure shown in Figure (3.14), known as the cradle. The earth rings of the decelerator rest on the support rods of the cradle. The cradle position, and hence the axis of the decelerator, can be manipulated from outside the vacuum chamber using a set of linear translation feedthroughs.

Figure (3.15) shows the assembled decelerator and cradle inside the vacuum chamber just before being closed off by the gate valve and then the source vacuum chamber. Next I will explain the high voltage electronics necessary to correctly charge and time the switching pattern.

3.5.2 High Voltage Electronics

The decelerator is repeatedly charged and discharged in such a way as to follow the passage of the molecules through the decelerator. A 300 m/s molecular beam will pass through adjacent

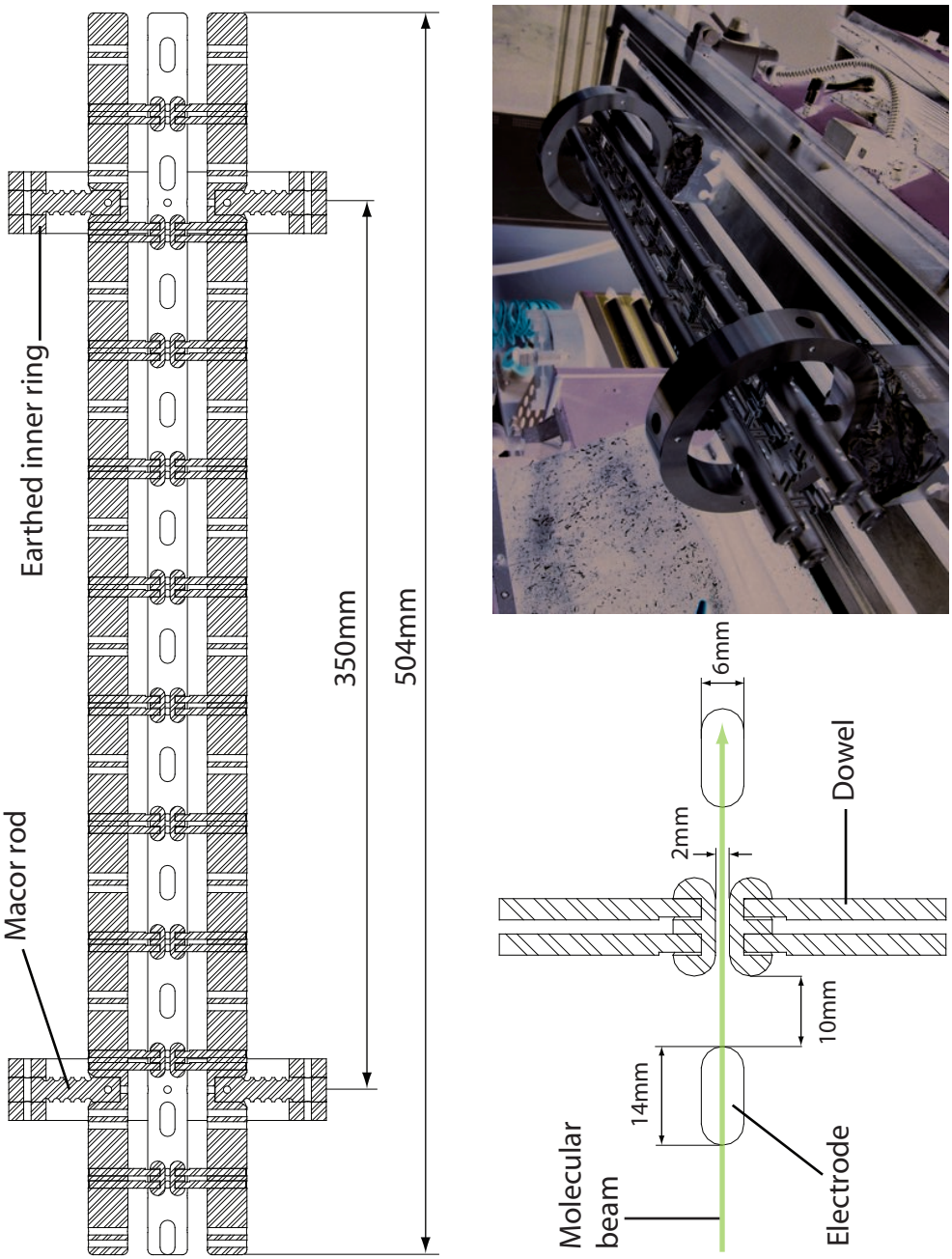

Figure 3.13: Plan view of the decelerator. A close up of the electrode dimensions and separations is also shown along with a photograph of the decelerator.

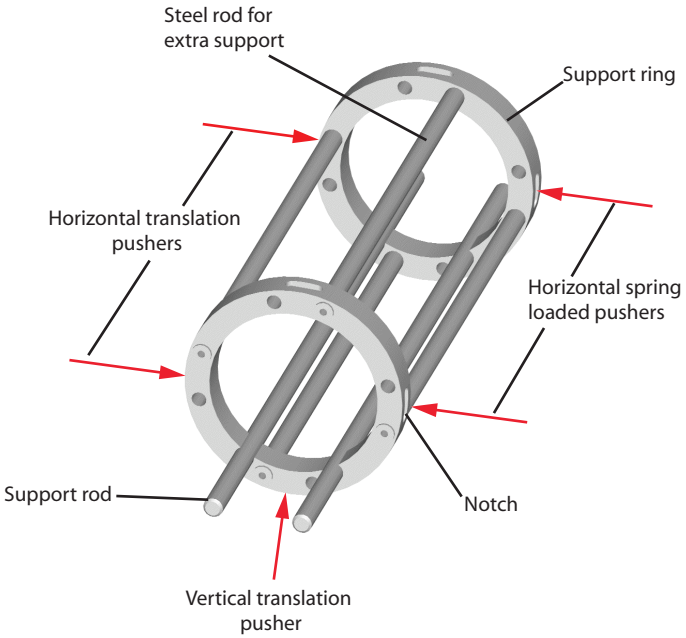

Figure 3.14: The cradle that supports and positions the decelerator inside the vacuum chamber.

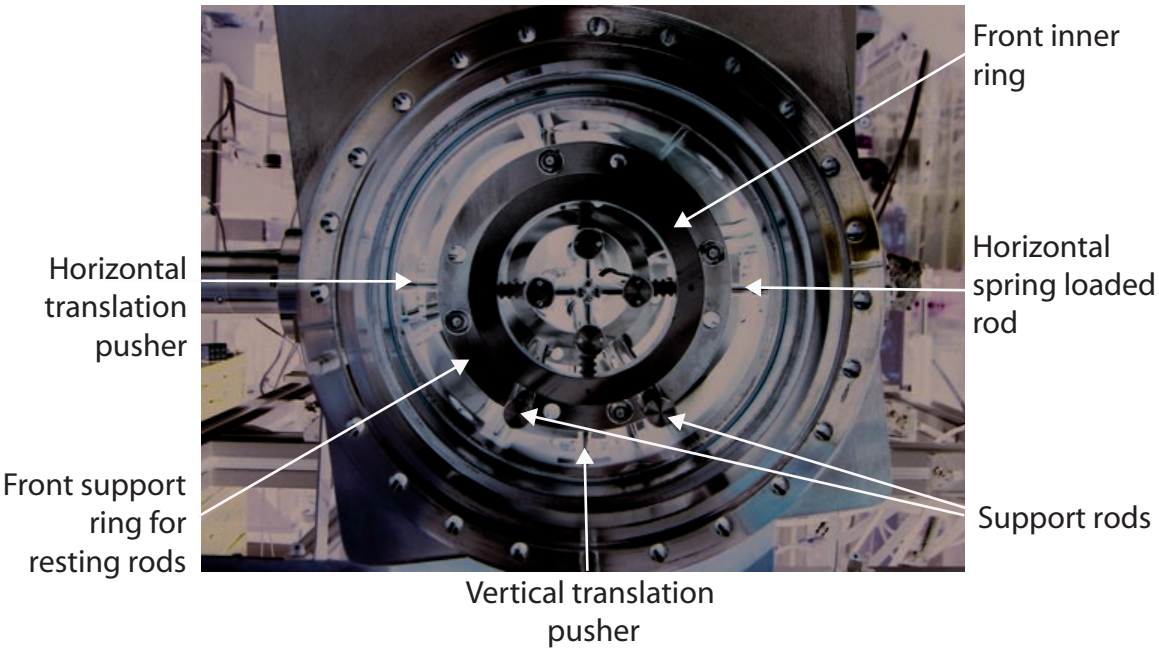

Figure 3.15: A photograph showing the installation of the decelerator inside the experiment chambers including the cradle and linear translation feedthroughs that hold and align it respectively.

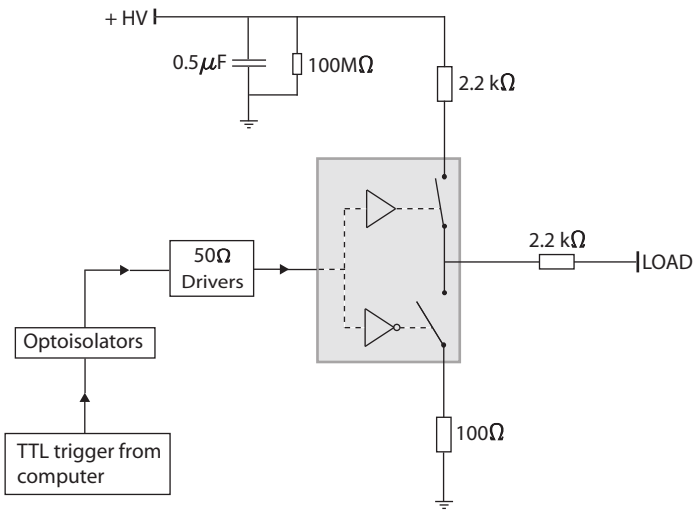

Figure 3.16: A schematic of one of the positive high voltage switches. The shaded box indicates the actual push-pull switch module. High voltage feedback to the computer is avoided using optoisolators along the trigger signal path. The 100MΩ resistor across the charging 0.5μF charging capacitor is used to safely discharge the capacitor when the decelerator is no longer in use.

lenses every 0.08 ms, this corresponds to an approximate 13 kHz burst mode which is repeated every 0.1 seconds to match the 10 Hz operating frequency of the solenoid valve. The correct voltages are applied using two high voltage power supplies (Spellman SL600), one for each polarity. Whilst, four commercially available push-pull solid-state switches (Behlke HTS series), one for each decelerator rod, are used to correctly time the charging. Figure (3.16) shows a schematic of one of the high voltage pulsed circuits.

The decelerator's capacitance was determined by measuring its frequency response when arranged in a low pass filter configuration. A variable frequency sine wave from a function generator was applied to one of the rods with a 9.9 kΩ resistor in series. The amplitude of the voltage on the high voltage feedthrough to the rod was recorded and the ratio of output to input amplitudes is plotted as a function of the frequency of the sine wave in Figure (3.17). The dashed line in Figure (3.17) follows the $3dB$ point of the response curve and occurs at a frequency of 0.18MHz. For a low pass filter, $f_{3dB} = 1/2\pi RC$ yielding a value for the capacitance, $C = 87$ pF when $R = 9.9$ kΩ.

The decelerator has 21 electrostatic lenses and so is charged 21 times every 0.1 seconds. With an applied voltage of 20 kV, the charged stored on one of the rods is 1.7 μC, thus the time averaged current drawn from the supply at this voltage is 0.4 mA. However the charging current associated with the application of a voltage step input is much bigger; a voltage of 20 kV is reached after 1 μs, so the maximum value of the charging current is 1.7 A. As this exceeds the maximum current that can be drawn from the high voltage power supplies, we use a 0.5 μF charging capacitor, rated for 20 kV, to provide the charge. Due to this finite capacitance a drop in voltage is expected as charge is removed. The amount of charge stored

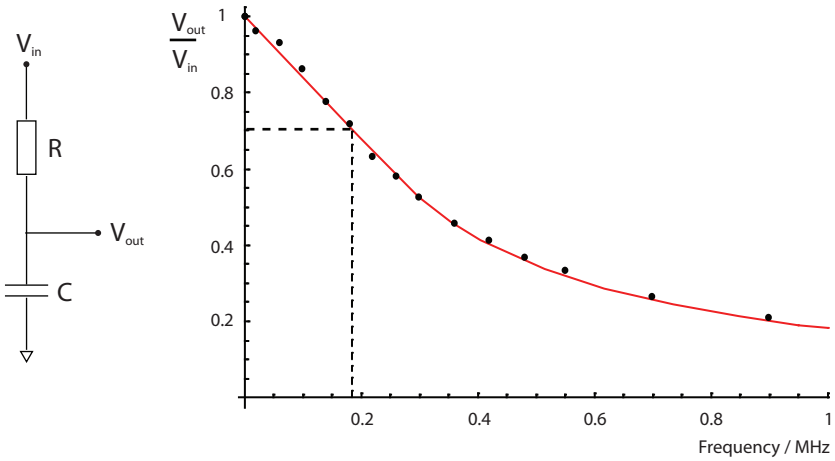

Figure 3.17: Measurement of the frequency response of one of the decelerator rods. The black points (•) are the experiment data whilst the dashed line indicates that $f_{3dB} = 0.18MHz$ and hence $C = 87pF$ when $R = 9.9\text{k}\Omega$. The red curve is the response of a low pass filter with these values of C and R.

will drop an amount $\delta Q = C\delta V$ which is equal to the number of charges of the decelerator, N, multiplied by the total charge stored on a rod at voltage V, $N \times C_{decel}V$. Thus the fractional change in voltage across the burst, $\delta V/V$, is NC_{decel}/C. For 21 charges this comes to a 0.4% drop which is acceptable.

The switches are under the control of a 50 MHz pattern generator which sends the appropriate trigger TTL pulses to the control circuit of the switch modules. This enables precise and real-time, user-controllable timing sequences.

The decelerator is operated using very large electric fields and it is important that no electrical discharges occur between the electrodes that could damage either the external electronics or the electrode's surface. There are two main physical sources of electrical discharge when working with high voltage [47]: breakdown due to ionization of ambient gas between the electrodes and vacuum breakdown due to electrode surface processes. In our setup, the breakdown mechanism is not gas related, as the ambient pressure in the experiment vacuum chambers is very low and is instead dominated by surface effects of the electrodes.

Micron-sized protrusions on the surface of the electrodes can enhance the local electric field. This enhanced local field enables an increased release of electrons. The electrons are accelerated by the electric field and strike the anode's surface, causing sufficient localized heating and vaporization of the electrode surface to initiate breakdown. Alternatively microscopic particles, such as dust particles, that are loosely adhered to either electrode surface may be torn from the surface by the applied field and, because of their charge, accelerated across the gap to impact on the opposite electrode and also cause localized heating and vaporization of the electrode material that may initiate electrical breakdown.

A systematic study of these processes was not undertaken, however steps were taken to

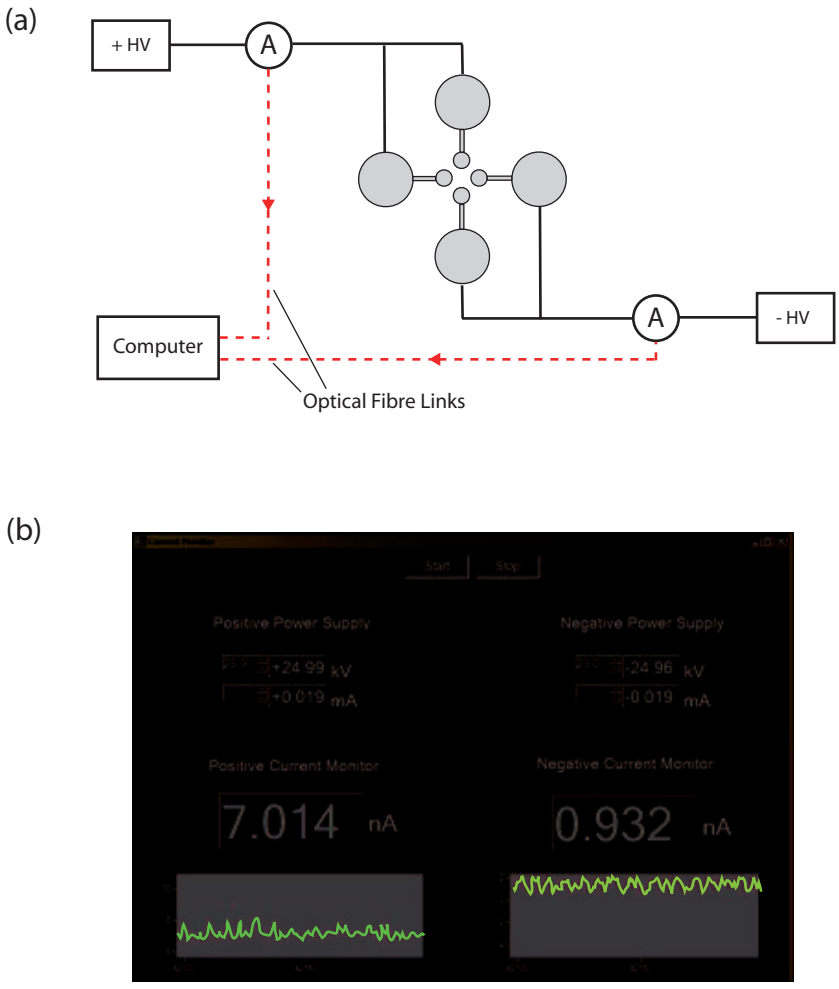

Figure 3.18: (a) The high voltage conditioning apparatus. The ammeters are electrically isolated from the laboratory by powering them with batteries and delivering the measured current value as an optical frequency over an optical fibre to the computer. (b) The front-end computer interface where the voltages can be controlled and the current is displayed as a function of time.

reduce the risk of these occurring and leaving catastrophic damage. Before installing the decelerator in the vacuum chamber all the electrodes complied to having a surface finish of 0.8 μm total peak-to-valley height or better, and were then electro-polished. The assembled decelerator was thoroughly cleaned using an industrial grade detergent, Decon90, and finally placed in an ultrasonic bath of isopropanol.

These alone are not sufficient to guarantee safe operation of the decelerator. A better technique involves conditioning the surface of the electrodes to sustain a value of the voltage that is higher then the working value. This conditioning procedure involves increasing the applied voltage on the electrodes in small steps such that all major pre-breakdown current instabilities are allowed to decay before the next voltage increment is applied. It ends when the applied voltages have reached ± 25 kV has been reached and no more current spikes are seen (the decelerator's switching operation never exceeds an applied voltage of ± 20 kV). This procedure is repeated every time the vacuum chambers are let up to air.

3.6 Computer Control of the Experiment

Much of the experimental hardware is controlled using a standard PC fitted with a National Instruments Pattern Generator (PG) and Data Acquisition (DAQ) board. Software written in-house in the C# programming language oversees the device triggers and manages the incoming fluorescence data.

The digital outputs trigger the valve controller which opens the valve, the flashlamp and Q-switch of the Nd:YAG laser and the gating of the PMT. This pattern is generated and then effected an adjustable number of times at 10Hz to complete what is called a scan i.e. a scan is composed of a number of shots each of which corresponds to the valve opening, the Nd:YAG laser firing and DAQ board being triggered to buffer data from the PMT's amplifier. The timing for these triggers are all measured relative to the Q-switch trigger.

The DAQ board also has analogue voltage outputs. During a scan an analogue output is used, for example, to ramp the laser frequency in discrete steps corresponding to the number of shots. In this way a scan is used to generate the LIF spectrum of the molecules in the beam. Other analogue outputs exist that control other devices, such as the high voltage power supplies that supply voltage to the decelerator. This can be used to ramp up the voltage output applied to the decelerator when used in guiding mode. Monitoring the fluorescence versus applied voltage tells us how well the decelerator guides the molecular pulses as a function of voltage. Alternatively the switches can be operated on every other shot so that in one scan two data sets exist: shots when the decelerator was on and shots when the decelerator was off. This makes it easier to compare the two cases.

3.7 Summary

This chapter has detailed all the equipment that is used to successfully run a molecular beam experiment and a Stark decelerator. The next chapter will explain in greater depth the operation of the molecular source and how it is optimized.

Chapter 4

Cold Supersonic Beams of YbF and CaF Molecules

This chapter describes the production and characterization of pulsed beams of CaF and YbF free radical molecules. Each pulse of molecules is seeded in an inert carrier gas and the cooling undergone by this gas as it expands from the nozzle acts as a cold bath cooling the translational, rotational and vibrational degrees of freedom of the molecules. A brief overview of the theory of supersonic beams is given. This is followed by a how–to account for making and optimizing these beams in the laboratory; beginning with an account on the preparation and optimization of the carrier gas beam, then the molecular signal itself. The gross electronic structure of the ground and first excited electronic states of CaF will be described, and a characterization of the detection transition will be explained. This chapter will end with a brief study of the formation of inert gas clusters in our gas jet, pointing to a link between the presence of clusters and the observed molecular beam intensity.

4.1 Brief Review of Supersonic Beams

A common technique for producing a wide range of cold ($\sim$1K) atoms or molecules is to allow them to expand under high pressure (typically several atmospheres) through a nozzle into vacuum. There are two limiting flow regimes: effusive and supersonic.

An effusive beam results when the nozzle the particles pass through in moving from a high-pressure region to vacuum has dimensions smaller than the mean free path of those particles. These molecules emerge from the nozzle without undergoing collisions and thus the velocity distribution in the beam is the same as that in the container, except with an extra velocity factor in the velocity distribution function that reflects the fact that faster molecules have a greater probability of leaving the source.

If the nozzle dimensions are instead greater than the mean free path of the particles then they will undergo many collisions as they exit the high-pressure gas region. In particular,

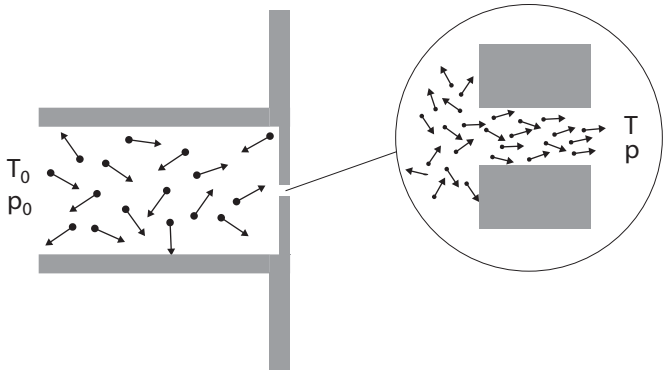

Figure 4.1: Schematic of the expansion of a gas through a nozzle. A stationary gas is held at pressure p_0 and temperature T_0. For a nozzle whose dimensions are smaller than the mean free path of the particles the gas flow through the nozzle is dominated by collisions which are driven by the pressure gradient between the inlet and outlet of the nozzle.

the large pressure gradient between the entrance and exit of the nozzle greatly amplifies the forward motion of those particles closest to the high vacuum region as they are accelerated by the collisions with those particles immediately behind them. This results in a velocity distribution in the beam whose average velocity is greater than the local speed of sound (hence the common usage of the name *supersonic* for these beams). The increased forward motion has come at the expense of the random thermal motion of the particles in the source resulting in a velocity distribution in the beam that is much narrower than that in the source, and has a correspondingly lower temperature. Figure (4.1) shows a simplified schematic of the supersonic gas source, consisting of a reservoir of particles whose temperature T_0 and pressure p_0 are typically room temperature and several atmospheres. These quantities are often termed the stagnation temperature and stagnation pressure. The temperature and pressure of the gas in the flow at the exit of the nozzle are labelled T and p respectively.

A thermodynamic analysis, assuming idealized conditions, can be applied to the gas expansion process to arrive at the key results. These assumptions are that the gas is an ideal gas and that no heat or other viscous effects are present during the expansion, i.e. the expansion is isentropic. The latter approximation is adequate as the time spent in the nozzle by the particles is short in comparison to the time taken for the particles to reach the walls of the nozzle. We begin by considering the total energy transferred across the inlet by the gas. This is given by the sum $U_0 + \frac{1}{2}mv_0^2 + p_0V_0$; where U_0 is the internal energy of the gas, $\frac{1}{2}mv_0^2$ is the kinetic energy of mass m of gas whose flow velocity is v_0, and p_0V_0 is the *flow work* term which is the work required to move the mass of gas against pressure p_0. A similar expression for the total energy transferred across the outlet is $U + \frac{1}{2}mv^2 + pV$. Applying the conservation of energy we can equate these two expressions

$$U_0 + \frac{1}{2}mv_0^2 + p_0V_0 = U + \frac{1}{2}mv^2 + pV. \tag{4.1}$$

We can simplify this equation using the specific enthalpy $h = H/m$ where the enthalpy function is $H = U + pV$ and allow the inlet flow velocity to be zero as the gas behind the nozzle is stationary. Rearranging Equation (4.2) for the outlet flow velocity we find that

$$v^2 = 2(h_0 - h), \tag{4.2}$$

where h_0 and h are the specific enthalpies of the gas at the inlet and outlet respectively. Equation (4.2) shows that with an outgoing flow of mass at the outlet there is an associated decrease in specific enthalpy across the nozzle, and the larger the decrease, the higher the outlet flow velocity becomes. Using $du = Tds - pdV$, we find that the specific enthalpy differential is $dh = Tds + Vdp$. The usefulness of the specific enthalpy for this process is now apparent: as the flow is isentropic, $ds = 0$, we have $dh = Vdp$. Thus the increase in forward motion is brought about by a negative pressure gradient.

Following the treatment in [22] Equation (4.2) can be evaluated further using the specific heat at constant pressure $c_p = \partial h/\partial T$. Thus the outlet velocity v is determined by the integral

$$v^2 = 2\int_T^{T_0} c_p \mathrm{d}T. \tag{4.3}$$

For an ideal gas the specific heat capacity at constant pressure is $c_p = \frac{\gamma}{(\gamma-1)}\frac{k_B}{m}$ where γ is the ratio of specific heats and is fixed by the three translational degrees of freedom of the monatomic carrier gas over the relevant temperature range. Thus the integral in Equation (4.3) is straight forward to perform and the result is

$$v = \sqrt{2c_p(T_0 - T)}. \tag{4.4}$$

If the gas is cooled substantially in the expansion, $T << T_0$, we obtain the terminal velocity

$$v_\infty = \sqrt{\frac{2k_BT_0}{m}\left(\frac{\gamma}{\gamma-1}\right)}. \tag{4.5}$$

If the beam only cools to some finite temperature T after which it ceases to cool any further, then the final beam speed will not have reached the terminal velocity and is given by

$$v = v_\infty\left(1 - \frac{T}{T_0}\right)^{1/2}. \tag{4.6}$$

An important observation from this equation is that the beam velocity cannot exceed the terminal velocity v_∞ even if the beam temperature approaches zero.

The beam temperature is found by re–arranging Equation (4.4) for the temperature. It can be expressed in a concise form by utilizing the *Mach*–number associated with the flow speed v, $M \equiv v/a$, where a is the local speed of sound which for an ideal gas is $a = \sqrt{\gamma k_B T/m}$.

The result is the

$$\frac{T}{T_0} = \left(1 + \frac{\gamma - 1}{2} M^2\right)^{-1}. \tag{4.7}$$

Introducing the *Mach* number has the advantage that the beam temperature can easily be identified as being related to a species–specific quantity, namely γ, and a general property of the flow field M. Equation (4.7) allows for the temperature of the beam, if left long enough to expand, to tend to zero. However as the gas expands, the number density and hence the collision frequency decreases sufficiently fast that the particles no longer collide and no further cooling can occur. This transition between continuum flow where collisions occur and the free molecular flow where no further collisions occur is called the *freezing region*.

In our experiment we deduce the translational temperature of the beam by measuring the width of the time-of-flight profile of the molecules at the detector. Far from the nozzle the velocity distribution has the form

$$f(v)\mathrm{d}v = Nv^3 \exp\left(-\frac{m}{2k_B T}(v-u)^2\right)\mathrm{d}v, \tag{4.8}$$

where N is a normalization factor, u is the average speed, m is the mass of the molecule and T is the translational temperature [48]. If the nozzle allows through an infinitesimally short gas pulse, a detector at a distance L from the nozzle will record the time-of-flight profile

$$h(t) = \frac{NL^4}{t_0^5} \exp\left(-\frac{mL^2}{2k_B T}\frac{1}{t_0^4}(t-t_0)^2\right) \tag{4.9}$$

where $t_0 = L/u$ [23]. This is a Gaussian time-of-flight profile and it will be shown later to be a good fit to the experimental data.

The molecules in our beams are seeded in the inert gas pulses, and the inert gas number density in each pulse well exceeds that of the molecular component. Thus the expansion proceeds as though the carrier gas were expanding alone and the beam speed and temperature can be assumed to be governed entirely by the carrier gas component. In this environment, the number of atom-atom and atom-molecule collisions is much larger than molecule-molecule collisions. Thus, as the carrier gas cools it acts as a cold bath for the molecules, thus cooling the molecules as well. However molecules have rotational and vibrational degrees of freedom that atoms do not have. Typically the temperature associated with the translational and rotational energy of the molecules thermalize early in the gas expansion with the carrier gas atoms, thus achieving temperatures of the order of several Kelvin. However the vibrational degrees of freedom take longer to thermalize with the carrier gas and so tend to freeze out at temperatures of the order of several tens of Kelvin.

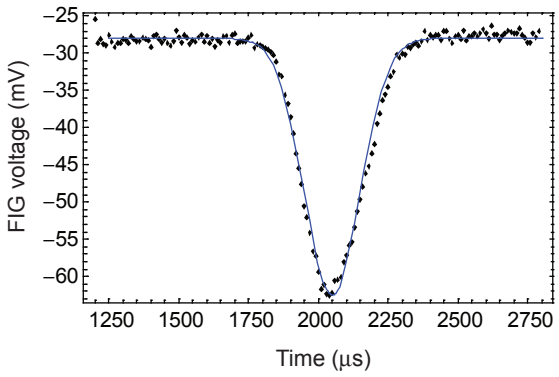

Figure 4.2: A FIG time of flight profile (black points) of a pulsed Ar beam. An approximate fit using a Gaussian function is shown in blue, and from the time of arrival and FWHM of this fit, the mean beam speed is ≈550 m/s and has an upper temperature limit of 3.4 K. In Section 4.2.2 we will see how the temperature is calculated.

4.2 Implementation

4.2.1 The carrier gas

Before we can produce molecules it is important that we make an intense and stable carrier gas beam. This section will describe how we go about this in the experiment.

A simple gas handling scheme delivers the inert gas from it's container bottle to the solenoid valve via a mixing chamber which is used to seed the carrier gas with fluorine bearing molecules. As shown in Figure (3.2) in Chapter 3 the inert gas resides inside the solenoid valve housing and is prevented from being released through the nozzle into the source chamber by a spring loaded poppet. To allow the gas to flow into the source chamber a voltage step is applied across the coil that surrounds the armature, which in turn pulls the poppet away from the nozzle. The amplitude and the duration of the applied voltage pulse, and the pulse repetition rate all control the quantity of gas that passes through the nozzle. The duration and repetition rate of the applied voltage step can be varied but are typically fixed at 300 μs and 10 Hz respectively. This leaves the magnitude of the applied voltage to be used to optimize the carrier gas beam.

The carrier gas pulses move 70 mm downstream to the skimmer aperture and travel a further 1050 mm to the fast ionization gauge (FIG). The FIG outputs a voltage which is directly proportional to the local pressure and it's time resolution enables it to detect the local change in pressure as the carrier gas pulse passes through it. The resulting signal is a time of flight profile (TOF) of the carrier gas and is used to optimize the gas source operating parameters. Figure (4.2) shows a typical time of flight profile of an Ar beam [1]. The blue curve is an approximate fit using a Gaussian function; the time of arrival and the FWHM of

[1] This is a typical FIG signal without the decelerator inside the chamber. With the decelerator present the amplitude of this signal is reduced by a factor of approximately 10.

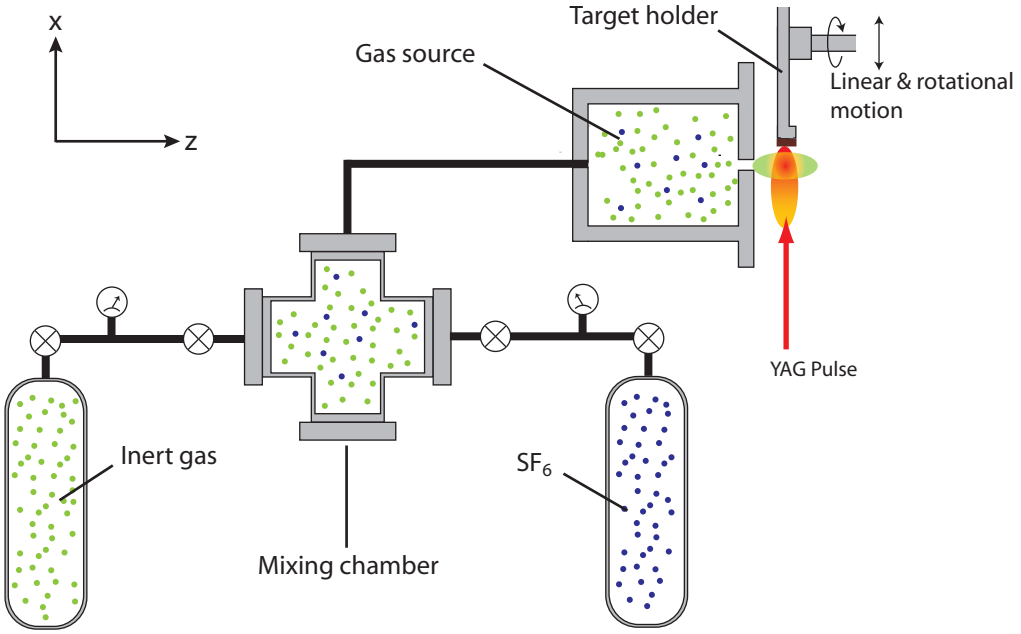

Figure 4.3: Schematic of the setup for gas delivery to the solenoid valve. An inert carrier gas (Ar, Kr or Xe) is delivered to the valve via a mixing chamber which will later be used to make mixes of the inert gas and fluorine bearing molecules.

the distribution of time of arrivals suggest a mean beam speed ≈550 m/s and an upper limit to the temperature of 3.4 K./. The temperature limit is calculated using Equation (4.11), and a discussion of this will be given in Section 4.2.2.

The FIG is predominantly used to check that a carrier gas beam is present and that it is well aligned with the beam axis. At this stage it is important to retract the target holder away from the nozzle along the x–axis (see Figure (4.3)). This ensures that the gas expansion is not interrupted by it and so that the nozzle has a clear line of sight with the FIG. The gas source alignment is controlled using 4 externally mounted screws, 2 for each transverse axis, that can be adjusted without breaking the vacuum. The nozzle is aligned to the beam axis when the amplitude of the TOF signal from the FIG has its maximum value. Next, the applied voltage to the valve is adjusted to maximize the FIG signal. For example, an optimized Ar beam with a backing pressure of 5 bar and the voltage duration and repetition rate at 300 μs and 10 Hz respectively the applied voltage is approximately 280 V and the source chamber pressure is typically 7×10^{-5} mbar. At higher valve voltages the FIG signal reduces in amplitude and exhibits asymmetric structure in the TOF.

In preparation for the production of molecules, the target holder is next translated along the $-x$–axis back into position close to the nozzle (see Figure (4.3)). The target surface is ≃2 mm from the edge of the nozzle orifice before the amplitude of the FIG signal begins to drop. The target is left at this position and we are ready to make YbF and CaF molecules.

4.2.2 The molecular beam

Both YbF and CaF are free radicals which have to made by a chemical reaction using suitable precursors. Our technique involves combining the laser ablation of a pure metal target and the gas expansion of an inert gas containing a small and controlled amount of SF_6. As shown in Figure (4.3) the SF_6 is seeded in the inert carrier gas in a mixing chamber. This gas mixture is connected directly to the valve and upon actuating the solenoid valve it is released into the source chamber. By correctly timing the target ablation with the valve opening, the hot cloud of metal atoms is entrained in the expanding gas mixture. The metal atoms and SF_6 molecules react to form the desired metal-fluoride molecules, which then thermalize with the cold inert gas atoms.

First a target needs to be prepared. The target holder consists of a stainless-steel wheel, and the metal target is glued using Torr Seal onto the rim of this wheel. Yb sheets are machined in–house into thin strips which are approximately 4 mm wide (equal to the rim thickness of the target disk) and have uniform 2 mm thickness. The lengths of these strips is dependent on the size of the original metal sheets, however it is straightforward to glue several segments end-to-end along the circumference of the target holder. A wheel design is implemented so that rotation of the wheel allows a fresh target spot to be exposed to the ablation laser thus prolonging the total lifetime of the metal target.

A Ca target is made in a very similar way except that Ca comes in the form of a block and not sheet form. Thus it needs to be cut and shaped to the desired form before it is ready to be glued to the target holder. During this process Ca has to be handled with care, as it is highly reactive with oxygen (particularly when heated) and water. A thin slice, 2–5 mm thick, is carefully sawed down one side of the block. This is done in a glove bag that has been filled with Ar gas. Furthermore vacuum pump oil is used to lubricate both the handsaw and the Ca block where it is being cut, so reducing the amount of heat generated. From this Ca sheet, a guillotine is then used to cut several strips whose widths are $\simeq$4 mm. This is done in air, however the oil left on the sheet helps protect it from oxidation. If the strips are long enough they can be shaped by hand to match the radius of the target holder. If not, they can be shaped using a roll-bending machine. The curved segments are then glued to the target holder's rim using Torr Seal. A target of this kind typically lasts several months, as the wheel can be removed and the target surface carefully filed down to remove any debris left by the ablation.

The ablation is performed using the 1064 nm light from a Q–switched Nd:YAG laser that is focussed on to the surface of the target. The pulses have 10 ns duration and run at 10 Hz, the same repetition rate as the valve. Two factors control the energy of the YAG pulse: the delay between the flash lamp and Q–switch triggers and the variable attenuator setting at the front of the laser head. With no attenuation, the energy per pulse has its maximum value of 35 mJ when the flashlamp-to-Q–switch delay is 150μs. In practice this delay value

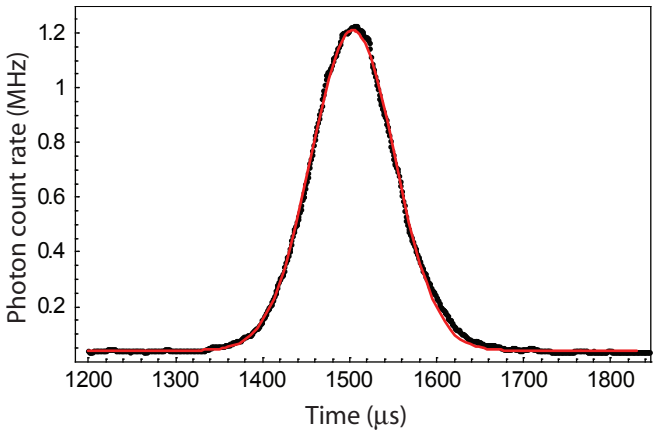

Figure 4.4: A time-flight profile of a CaF beam seeded in Ar. The red curve is a fit of a Gaussian function to the data: the peak arrival time and full width at half maximum give a beam speed and temperature of 594 m/s and 2.5 K respectively.

is not changed and the energy of the YAG pulses is set using the variable attenuator only. The YAG beam is aligned by eye on to the target so that it strikes the target at right angles to both the target's surface and the molecular beam axis. Typically the attenuator is set to 50% before a molecular signal has been detected, however it is reduced later on in the course of the molecular signal optimization. This is discussed later on.

To make cold molecular beams we would like to time the ablation to coincide with the densest region of the gas pulse where the collision rate, and hence the thermalization rate, is likely to be greatest. The time delay between opening the valve and the Q–switch of the YAG determines where the ablated metal atoms are entrained in the gas pulse. The valve-to-Q–switch delay is set at the experiment's control computer. When the correct delay is chosen, which is always in the range between 200 and 500 μs, a notch in the time of flight profile given by the FIG is observed indicating a region of low gas density where the ablation plume has knocked some the gas atoms out of the beam. Small adjustments to the timing shows this notch move relative to the mean arrival time of the gas pulse at the FIG. At this stage, the notch is centered on the peak of the FIG signal.

The molecules are entrained in the carrier gas pulse and thermalize with the inert gas atoms as the expansion proceeds. As explained in Chapter 3 the molecules are detected by the fluorescence they emit when they are excited by resonant laser light. The molecular signal is found by incrementally stepping up the dye laser's frequency for each gas pulse in the region of the desired transition. This transition is labelled $A^2\Pi_{1/2}(\nu = 0, N = 0) \leftarrow X^2\Sigma^+(\nu = 0, N = 0)$ and for CaF is centered on 494451 GHz. A discussion of the relevant spectroscopy and line identification for CaF will be given later. The laser frequency is locked on resonance and time resolved data acquisition from the PMT yields CaF time of flight data. Figure (4.4) shows the time-of-flight profile for an optimized CaF beam seeded in Ar. A very good fit

is found between this data and a Gaussian function (red curve). From the fit we deduce the beam speed and the translational temperature of the pulse of molecules arriving at the detector to be 594 m/s and 2.5 K respectively. The form of this Gaussian function is

$$F(t) = h + A \exp\left(-4 \ln 2 \left(\frac{t - t_0}{\Delta t}\right)^2\right) \tag{4.10}$$

where h is the background, A is the amplitude, t_0 is the arrival time of the peak and Δt the full width at half maximum of the Gaussian function. By equating the arguments of the exponents in Equations (4.10) and (4.9) we arrive at an expression for the beam temperature

$$T = \frac{m(L\Delta t)^2}{8 \ln 2 k_B t_0^4}. \tag{4.11}$$

The distance travelled, L=894 mm, mean arrival time t_0=1504 μs and full width at half maximum Δt=113 μs are then used to calculate the beam speed and temperature as given. Using Equation (4.5), the terminal velocity of an Ar beam whose source is at room temperature is 550 m/s. It is quite typical for the molecular beam speeds to exceed the expected terminal beam speeds by approximately 10%. This discrepancy is most likely due to the molecular beam not having completely thermalized with the carrier gas and that the speed estimate, $u = L/t_0$, neglects the acceleration of the molecules during the early stages of the expansion.

The molecular time of flight data is now used as the beam diagnostic. The relative partial pressure of SF_6 in Ar (Xe) and the total backing pressure for the Ar/SF_6 mix are fixed at 5% and 5 bar (3 bar with Xe) respectively. These values have been found to provide highest amplitude, slowest speeds and coldest beams. It is important to realize that the optimum experimental settings for the carrier gas beam are not the same as those for the molecular beam and so will change. The first of these to change is the valve voltage. The amplitude of the molecular time-of-flight profile is maximized when the valve voltage is increased such that the source chamber pressure is 1×10^{-4} mbar. We may infer from this that the increased amount of carrier gas flowing out of the nozzle captures more of the ablated atoms thus forming more metal-fluoride molecules. Another result of this change is that the beam is slightly ($\sim$5%) faster; the benefit of a larger signal, however, outweighs the cost of a small increase in speed. We next translate the target holder closer to the nozzle so that the metal surface is brought to within $\simeq$1 mm of the nozzle edge. With the target this close a better overlap between ablation plume and expanding gas jet is achieved. It is also necessary to concomitantly decrease the YAG power during this stage from the previous value of 18 mJ (50% attenuation) to about 10 mJ (70% attenuation). The valve voltage may need a slight tweak once this is complete.

As the valve voltage, target position and YAG pulse energy have changed it is now necessary to re-tune the delay between opening the valve and the Q–switch. Previously

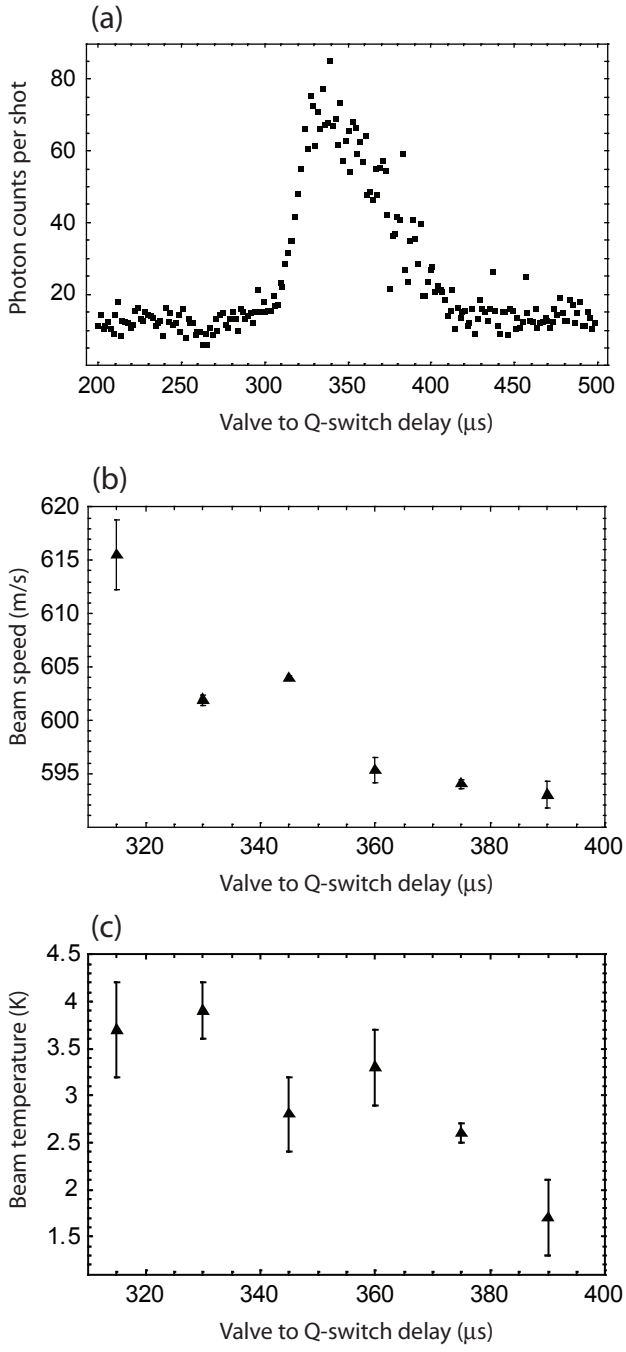

Figure 4.5: (a) CaF beam intensity, (b) speed and (c) temperature for different values of the valve to Q-switch delay, using Argon as the carrier gas.

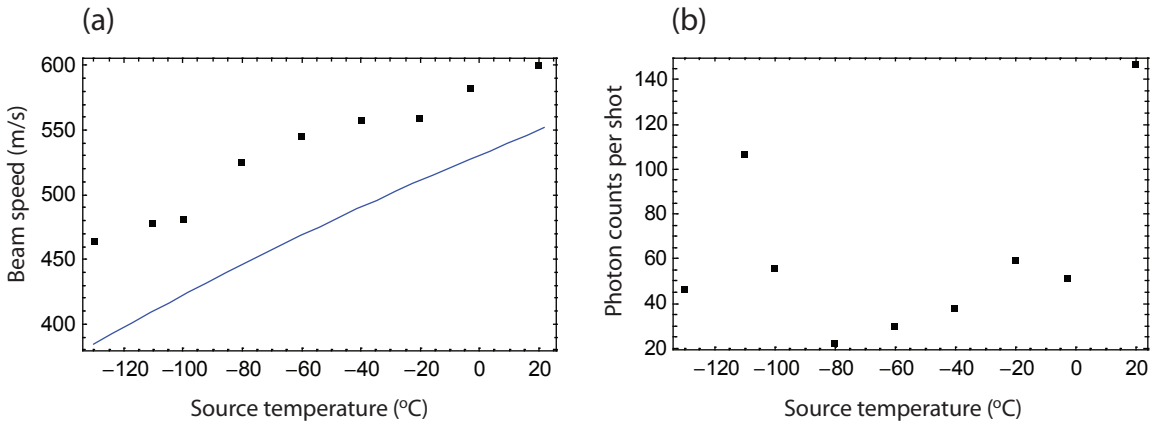

Figure 4.6: (a) CaF beam speed and (b) fluorescence signal as the valve assembly is lowered in temperature. The CaF molecules were seeded in Ar.

this delay had been determined by positioning the notch created by the YAG laser in the carrier gas beam on to the peak of the FIG signal. Now we re-optimize the delay using the molecular signal at the PMT. Figure (4.5) (a),(b) and (c) show the CaF beam intensity, speed and temperature respectively versus the valve-to-Q–switch delay. In graph (a), there is a distinct region of delay values for which molecules are produced, beyond which no molecules are seen at all. This behaviour is also repeated by the other inert gases and these regions also lie within the same range of delay values. Furthermore the speed and temperature of the molecular beam drops as the delay is increased across this region. The minimum speed and temperature are found for a delay of $\simeq$390 μs. This is the same delay value as was used to centre the notch onto the peak of the FIG signal. This indicates that the molecules do indeed cool the most where the carrier gas density is greatest, however this is not where the greatest number of molecules are produced. This is found for a valve-to-Q–switch delay of 340 μs. We do not understand why this the case but we may speculate that the higher temperature of the inert gas atoms in the less dense region may be more suitable an environment for the hot Ca atoms to react with the SF_6 molecules. In practice the value chosen for the valve-to-Q–switch delay is that which maximizes the intensity of the molecular signal.

With the parameters optimized as above we have achieved our goal of an intense cold molecular beam. However the experimenter must bear in mind that the target spot does not have an indefinite lifetime. Typically the molecular signal is greatest when a fresh target spot is initially hit. During the next $\sim$100 shots of the YAG laser the signal decays and the TOFs arrive later at the detector. The signal has decreased in size and speed by approximately 10% and 5% respectively. After this, the signal remains stable, in amplitude and speed, for several thousand shots before decaying completely. The initial drop in signal is attributed to the surface conditions, such as temperature and morphology, changing as the YAG pulses are fired. The slow decay which finally kills the beam after several thousand shots has been

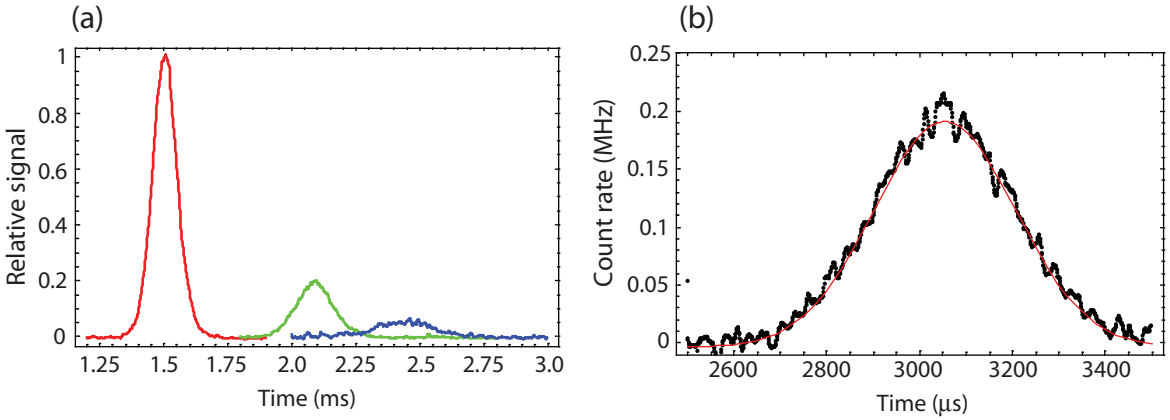

Figure 4.7: (a) Time of flight profiles of optimized CaF beams seeded in Argon (red curve), Krypton (green curve) and Xenon (blue curve). The respective relative beam intensities and speeds based on the mean arrival times are 1:0.29:0.12 and 594 m/s, 428 m/s and 367 m/s. (b) Slowest YbF beam speed is 294 m/s and whose temperature is 5 K.

linked with the accumulation of a black residue that is deposited on the target spot. This residue is thought to be sulfur from the carrier gas [49]. A useful visual diagnostic of the quality of the beam optimization and target health is to verify that when pulsing the valve and the YAG, the end of the ablation plume furthest from the target is swept along by the expanding gas in the direction of the skimmer, and that where the plume and gas collide there is a noticeable orange colour present for CaF beams (or blue/green for YbF beams). These indicate the formation and de-excitation of CaF molecules as they collide with the SF_6 molecules and the inert gas atoms.

A simple and convenient method for making slow molecular beams is to cool the valve assembly directly using liquid nitrogen (LN_2). As shown in Figure (3.2) in Chapter 3, the boil-off from a pressurized LN_2 dewar is passed through a jacket which is in thermal contact with the valve. The inert gas inside the valve thermalizes with the cold walls of the valve thus reducing the terminal velocity of the inert carrier gas as it expands outside the nozzle. Figure (4.6) (a) shows the significant drop, ∼25%, in the speed of YbF beams (black points) as the gas source assembly is cooled. The blue curve in Figure (4.6) (a) is the terminal velocity of an Ar beam over the same temperature range. The discrepancy between the two sets of data agrees with the consistent observation that the molecular beam speeds are always approximately 10% higher than the expected carrier gas terminal velocities.

The YbF signal intensity does not stay constant when the source temperature is changed: Figure (4.6) (b) shows that the YbF beam intensity initially rapidly drops by a factor ∼3 as the valve assembly is cooled from room temperature, reaching it's minimum value at -80 ^{o}C, and then increases as the temperature is reduced even further. The latter behaviour is very desirable as the signal intensities are comparable and yet are much slower than those at room temperature. However, the molecular signals below -80^{o}C were very unstable: upon exposing

a fresh target spot the signal is initially large but it rapidly decayed, within ∼10 shots, into the background. This behaviour was not seen for temperatures above -80^{o}C; these signals remained relatively stable only decaying after several ∼1000 YAG shots. The rapid decay seen below -80^{o}C may be linked to the sublimation of SF_6 onto the target surface, which at 0.1 bar partial pressure is expected to occur at -95^{o}C[50]. The presence of solid SF_6 on the target surface may enhance the production of YbF but as the surface is heated by the YAG, the SF_6 will also heat up and revert back to gaseous form thus taking away this production mechanism. Nevertheless this cooling scheme is a very reliable method for making slow molecular beams. Figure (4.7) (a) shows the time-of-flight profiles of our molecular beams (either YbF or CaF) when seeded in Ar (red), Kr (green) and Xe (blue) gas. These time-of-flight profiles have been normalized in amplitude to the Ar-carried profile. The beam speeds, inferred from the mean arrival times of the molecules at the detector, are 594 m/s, 428 m/s and 367 m/s respectively. Figure (4.7) (b) shows our slowest, 294 m/s, YbF beams using Xe as the carrier gas and cooling the valve assembly to -63^{o}C. This represents a 20% decrease in speed over that at room temperature. Figure (4.7) (a) shows a concomitant decrease of the signal intensity as the mass of the carrier gas increases. The integrated signals always decrease in the same approximate ratio, 1:∼1/3:∼1/7 with Ar, Kr and Xe respectively. A possible reason for this, is the increased production of clusters of inert gas atoms which may trap the molecules and so reduce the molecular beam intensity. A study of the clustering of inert gas atoms in our source will be presented later in the chapter.

The production of YbF by ablation of stationary targets composed of various different solid chemical precursors into a pure inert gas expansion has been investigated[23]. These solid precursors were Yb/AlF_3 and Yb/YbF_2. It was found that the peak YbF signals were the same for each chemical mixture. The production of CaF using different gaseous chemical precursors and the ablation of a pure metal target has also been investigated; these were nitrogen trifluoride (NF_3) and freon (CH_3F). CaF beams were made with each of them and yielded similar beam intensities when seeded in Ar. No molecular signal was observed for the heavier carrier gases. As with SF_6, the highest CaF signals were observed when the NF_3 and CH_3F partial pressures were very low, ∼5% of the inert gas pressure.

4.2.3 Spectroscopy of CaF

The alternating gradient Stark decelerator is designed to decelerate molecules in the ground electronic, vibrational and rotational state. Thus it is important to be able to identify the transitions connected to this ground state energy level. In practice this is done by incrementally stepping the dye laser's frequency for each gas pulse whilst simultaneously measuring the fluorescence emitted by the molecules; the molecules fluoresce when the laser light is resonant on a transition, thus building up a laser induced fluorescence (LIF) spectrum of the molecular beam.

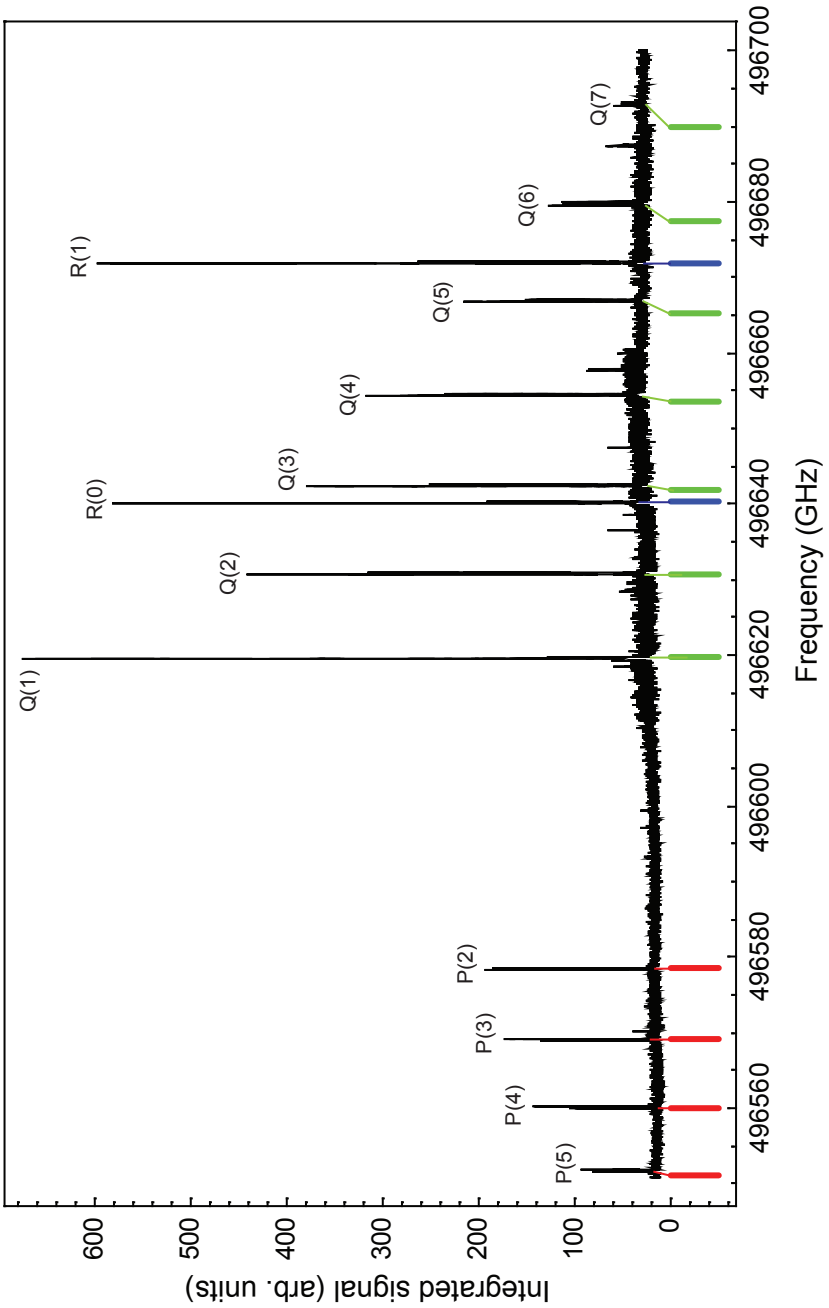

Figure 4.8: The rotational structure (black data) of the $A_2^2\Pi_{3/2}(\nu = 0, N') \leftarrow X^2\Sigma^+(\nu = 0, N'')$ transition in CaF. The expected pattern of lines is shown by the coloured vertical lines and their identity by the labeling written above the observed data. The expected line pattern was calculated from published spectroscopic constants.

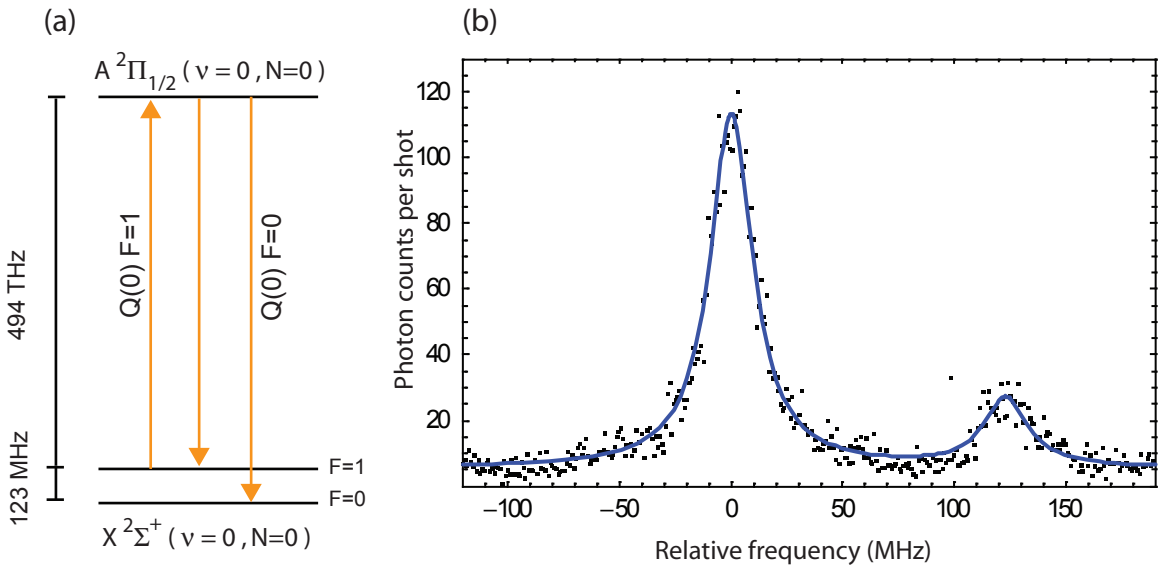

Figure 4.9: (a) The detection transition connecting the ground electronic state to the first excited electronic state, $A^2\Pi_{1/2}(\nu = 0, N = 0) \leftarrow X^2\Sigma^+(\nu = 0, N = 0)$. (b) Experimental data showing the taller Q(0) F=1 and the smaller Q(0) F=0 transitions. The blue curve is a fit of the sum of two Lorentzian functions to the experimental data showing excellent agreement. The fit gives 23.2 MHz and 23.5 MHz for the FWHM of the F=1 and F=0 hyperfine components.

The electronic structure of the YbF molecule has been extensively studied [51] and has provided a detailed knowledge of the ground electronic state [52, 53], the first excited electronic state [54] and their Stark shifts [55]. Furthermore, these studies have led to precise measurements of the electric dipole moment of the electron in YbF [56, 49]. The spectroscopy of the electronic ground state of the CaF molecule has similarly been investigated and I direct the reader to the following references for this information [57, 58]. An introduction to the gross structure of the ground and first excited electronic states of the $^{40}Ca^{19}F$ molecule will be given.

The electronic configurations for Ca and F are $[Ar]4s^2$ and $[He]2s^22p^5$ respectively. The Ca and F atoms form a strong ionic bond as the Ca atom donates a 4s valence electron to the F atom. The remaining 4s electron remains centered on the metal atom and interacts with a core, which includes two closed shell ions Ca^{2+} and F^-, in much the same way as the s-valence electron does in an alkali atom. In the rotational, vibrational and electronic ground state, $X^2\Sigma^+(\nu = 0, N = 0)$, the spin of the 4s electron interacts with the spin 1/2 of the fluorine nucleus to form singlet and triplet hyperfine levels F=0 and F=1. This splitting is approximately 123 MHz. In the first excited electronic state there is a large fine structure interaction that splits this level into two, labelled A_1 and A_2. The full term symbols of these levels are $A_1^2\Pi_{1/2}$ and $A_2^2\Pi_{3/2}$. We are interested in the $A_1^2\Pi_{1/2}(\nu = 0) \leftarrow X^2\Sigma^+(\nu = 0)$ and the $A_2^2\Pi_{3/2}(\nu = 0) \leftarrow X^2\Sigma^+(\nu = 0)$ transitions. Here, $\nu = 0$ denotes the lowest vibrational level in each of the two electronic states. The upper state has hyperfine structure as well;

though the magnitude of the splitting is unknown it is likely to be much smaller than the 123 MHz ground state hyperfine splitting and so the upper state is treated as a single state. Later, when we consider the line width of the $A_1 \leftarrow X$ transition, we will see that this is an acceptable assumption.

To find the desired transition, wide frequency LIF spectra were measured and compared against theoretical predictions of the line positions. Figure (4.8) shows a wide frequency scan showing the rotational lines in the $A^2\Pi_{3/2}(\nu' = 0, N') \leftarrow X^2\Sigma^+(\nu'' = 0, N'')$ electronic transition (black data). This graph is obtained from many partially overlapping scans, each approximately 15 GHz wide. The absolute frequency stability is measured with an accuracy of ± 0.5 GHz using a home-built wavemeter. The relative frequency scale is determined using a confocal cavity described in Section 3.3.1, whose free spectral range is 750 MHz$\pm$5MHz. The expected pattern of lines, based on the published spectroscopic constants of CaF [58], are shown below the experimental data as coloured vertical lines. We find there to be a significant discrepancy between the absolute frequency of our spectral lines and that determined from the spectroscopic constants given in the literature. This discrepancy is still being investigated. In the figure I have simply shifted the entire pattern of lines obtained from the literature so that it matches well our experimental data. The labeling above the observed transitions identifies them. The P,Q and R labels refer to the change in rotational quantum number $\Delta N = -1, 0, +1$. The number in the brackets refers to the rotational quantum number of the lower state in that transition.

Overall, the agreement between the observed and expected pattern of lines is very good. However, an increasing discrepancy between observed and expected line positions arises, which is seen more clearly with the Q lines, when we move up the frequency axis starting from the Q(1) line. This is believed to be the result of an inaccurate value for the rotational constant in the published literature. This value was the result of a fit to rotational transitions in CaF produced in a hot furnace. The high rotational quantum numbers associated with the molecules in this furnace will distort due to the centrifugal effect and this is added to the fitting procedure. However it is feasible that the best fit values for the rotational constant and the centrifugal distortion parameter may be sufficiently incorrect to result in the discrepancy observed in Figure (4.8). Similar LIF spectra were obtained for the rotational lines in the $A_1^2\Pi_{1/2}(\nu' = 0, N') \leftarrow X^2\Sigma^+(\nu'' = 0, N'')$ electronic transition. From these, the Q(0) transition was identified.

Figure (4.9) (a) shows the relevant energy levels for our experiment. The LIF laser beam excites the CaF molecules into the first excited electronic state $A^2\Pi_{1/2}(\nu = 0, N = 0)$, which we treat as a single state. The transition from the F=0 state is labelled Q(0) F=0. Similarly, the transition from the F=1 state is labelled Q(0) F=1. These transitions require laser light at around 606 nm. Figure (4.9) (b) shows a narrow frequency scan across the Q(0) F=1 (larger) and Q(0) F=0 (smaller) transitions with 0.3 mW incident laser power. In all our experiments

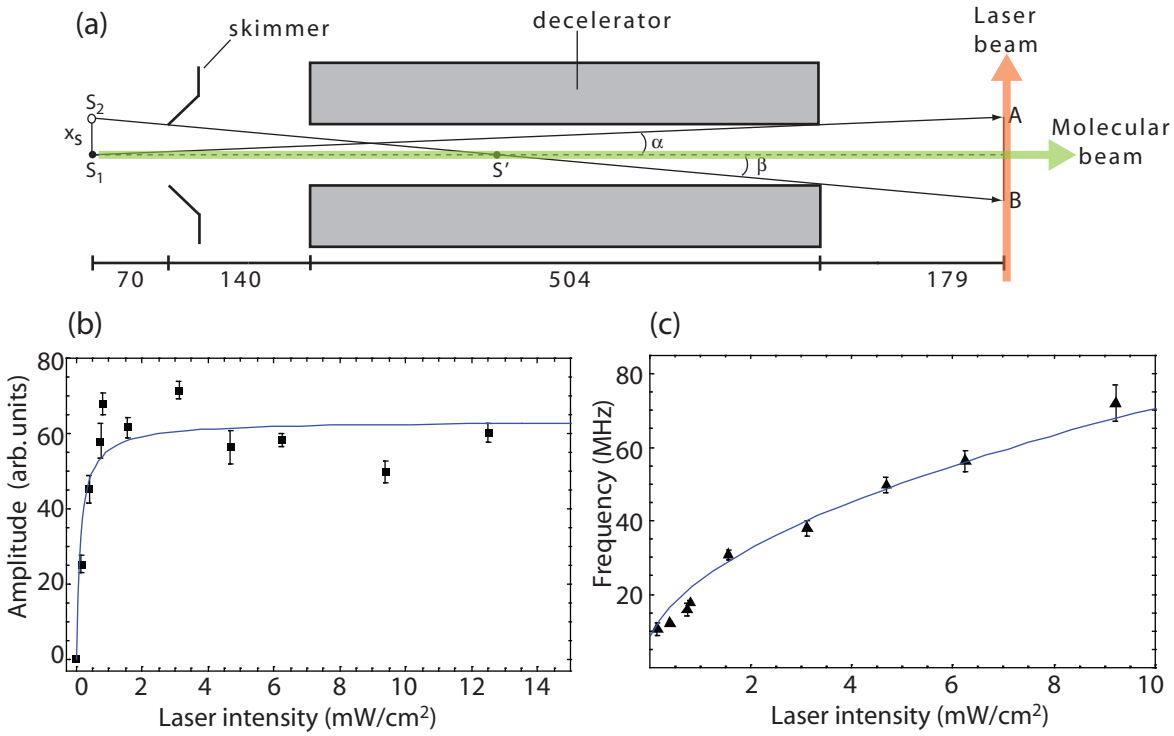

Figure 4.10: Spectral broadening of the Q(0) F=1 transition. (a) The maximum Doppler spread along the laser beam axis is 4.1 MHz given a 600 m/s mono-energetic beam that traces the ray S_2B from a source with transverse extent $2x_s$=2.4 mm. The strong dependence of the (b) Q(0) transition amplitude and (c) full width at half maximum on the laser intensity demonstrates power broadening. The blue curves are derived from the power broadening in a idealized two-level atomic system, see main text for details.

we tune the dye laser frequency on to the Q(0) F=1 transition as this provides the most signal. The resonant frequency of this transition is 494451±0.5 GHz which was determined using our wavemeter readings.

The Q(0) F=1 and Q(0) F=0 line shapes agree very well with the sum of two Lorentzian functions (the blue curve in Figure (4.9) (b)). Using the known hyperfine splitting of 123 MHz to calculate the frequency scale, the full width at half maxima for the Q(0) F=1 (Q(0)F=0) transition is determined from this fit to be 23.2±0.4 MHz (23.5±2.2 MHz). Lorentzian function fits to the Q(0) F=1 transition show consistently good agreement with the observed line shapes over a wide range of incident laser powers. I will from now on refer to the Q(0) F=1 detection transition as simply the Q(0) transition and ignore the F=0 component as it is never used in the experiment. The Q(0) line width has been measured [59] and predicted using *ab initio* calculations [60] giving the values 7.3±1.3 MHz and 8.2 MHz respectively. These are smaller than the width of the Q(0) transition in Figure (4.9) (b).

There are several factors which contribute to the line width: the natural line width, the Doppler width of the transverse velocity distribution, power broadening by the incident laser beam, hyperfine structure in the first excited electronic state and transit time broadening due

to the finite width of the laser beam in the direction of the molecular beam axis. Fitting the Q(0) line to Gaussian functions, shows consistently worse agreement than a Lorentzian fit in particular in the wings of the observed transition and for low laser powers, <0.5 mW. The Doppler contribution may be estimated by consideration of the geometry of the experiment shown in Figure (4.10) (a). The transverse Doppler width is given by $\Delta\nu = 2v\sin(\theta)/\lambda$, where λ=606 nm is the wavelength of the resonant laser light, $v\sin(\theta)$ is the velocity component that is parallel to the laser beam axis and whose axial speed is v. A 600 m/s mono-energetic beam originating from a point source at the origin, S_1, has $\theta = \alpha$ and the Doppler width is 2.7 MHz. This value increases to 4.1 MHz if the source has transverse extent $2x_s$ at the origin, as it may very well do in the actual experiment. These are smaller than the expected natural line width.

The Q(0) line amplitudes and widths exhibit a strong dependency on the incident laser power. In Figure (4.10) (b) the observed Q(0) line amplitudes (black data points) rapidly rise as the laser power is increased and then saturate to a constant value as the laser power is increased further. This saturation behaviour can be modeled if we consider an idealized system composed of atoms whose sole energy levels are E_1 and E_2 where $E_2 > E_1$ and have equal statistical weight factors $g_1 = g_2$ [61]. Furthermore there are N_1 atoms per unit volume in level 1 and N_2 atoms per unit volume in level 2, and the total atom density $N = N_1 + N_2$ is constant. Atoms may be excited from levels 1 to 2 if the photon energy of the incident laser light matches the energy difference between levels 1 and 2, $h\nu = E_2 - E_1$, where ν is the frequency of the laser. This stimulated absorption occurs with a probability $P = B_{12}\rho(\nu)$ where B_{12} is the Einstein coefficient for stimulated absorption and $\rho(\nu)$ is the energy density of the laser field and is proportional to the laser intensity. Atoms in level 2 may de-excite to level 1 either by stimulated emission, with the same probability as excitation P, or by spontaneous emission which occurs with a probability A_{21} known as the Einstein coefficient of spontaneous emission. During the time that the atoms are irradiated, the populations N_1 and N_2 will change. The rate equation for level 2 is $dN_2/dt = PN_1 - PN_2 - A_{21}N_2$. After some time the energy level populations will have reached steady-state and the population density in level 2 is

$$N_2 = N\frac{P}{2P + A_{21}}. \tag{4.12}$$

For low laser intensity, $P << A_{21}$, or equivalently when spontaneous emission depopulates level 2 faster than it is populated by stimulated absorption then $N_2 << N$ and N_2 is proportional to the laser intensity. The same behaviour is seen in Figure (4.10) (b) for very low incident laser powers $< 0.5\,\mathrm{mW/cm^2}$, the fluorescence signal is approximately linear with laser intensity. For very high laser intensity where the repopulation of level 2 far exceeds the losses due to spontaneous emission, $P >> A_{21}$, then $N_2 \to N/2$ and does not change any further. The populations in levels 1 and 2 are now equal and no further absorption takes place. Equation (4.12) can be recast in terms of parameters more relevant in our experiment

as

$$A = A_0 \frac{I/I_{sat}}{1 + I/I_{sat}}, \tag{4.13}$$

where A is the Q(0) line amplitude, I is the laser intensity (mW/cm^2), A_0 is the saturation Q(0) amplitude, and I_{sat} is related to the Einstein coefficient of spontaneous emission in Equation (4.12) and governs how quickly saturation is reached as the laser intensity is increased. A fit of Equation (4.13) to the Q(0) amplitude data in Figure (4.10) (b) is shown in blue with I_{sat}=0.14 mW/cm^2.

Figure (4.10) (c) shows the observed line width (FHHM) increasing as the laser intensity is increased. This continues for higher laser intensities i.e. it does not saturate as the transition amplitude does. This behaviour is another characteristic of power broadening. It can be shown that the saturation of a homogenously broadened transition with width Γ_0 is also a Lorentzian function with an increased width Γ given by

$$\Gamma = \Gamma_0 \sqrt{1 + \frac{I}{I_{sat}}}. \tag{4.14}$$

The broadening comes about because the absorption coefficient, $\alpha(\nu) = \alpha_0(\nu)/(1 + I/I_{sat})$, decreases by a factor $(1 + I/I_{sat})$ on resonance. However as I/I_{sat} has a Lorentzian profile, its impact on the absorption coefficient $\alpha(\nu)$ is felt most on resonance and less away from resonance. This has the effect of widening the transition width. Thus at low powers the width is the natural line width and it increases as the laser intensity is increased. Using the value of I_{sat}=0.14mW/cm^2, we can then fit Equation (4.14) to the transition width data with only one free parameter, Γ_0, the frequency axis intercept. In Figure (4.10) (c), this fit is the blue curve and has Γ_0=8.4±0.2 MHz. This value agrees very well with published measurement and theoretical value for the natural line width. Other contributions to the line width are all small. They are: 4 MHz Doppler broadening as already discussed, 0.5 MHz line width of the dye laser, as given in the dye laser's manual, and 0.02 MHz from transit time broadening as the laser beam has a finite width (4 mm) along the molecular beam direction. The final contribution is from the hyperfine splitting in the upper electronic state. The ground state hyperfine splitting for YbF (170 MHz) is similar to that for CaF and it is therefore reasonable to assume that the upper state splitting of CaF is also similar to that for YbF which is ≃3 MHz.

The closed two-level system for which photons are repeatedly absorbed and emitted between the same two levels is an unrealistic model of the excitation process occurring in CaF (or indeed for any molecule). This is because the upper excited electronic state in a molecule decays to many other rotational and vibrational levels. A more realistic model involves an optical pumping process between two energy levels where the upper state population is allowed to decay to a third level representing the other rotational and vibrational energy levels.

In this model, the population in the ground state can become arbitrarily small as more and more is pumped into the upper state which rapidly decays to the third state. This more complex optical pumping model, which more closely modeled our molecular energy levels, gave the same behaviour for the transition width and amplitude versus laser intensity as the simpler closed two-level model did.

4.3 Clustering

The characteristics of our molecular signal correlate very well with the dynamics of cluster formation from our gas jet source. We desire high molecular beam intensities with low speeds so that we may decelerate more molecules and eventually be able to trap a useful fraction of these for further experiments. I will briefly summarize the relevant details pertaining to the molecular signal intensity before discussing cluster formation. Figure (4.7) (a) shows that the molecular signal is most intense for Ar carried beams and least intense with Xe carrier gas. The relative molecular signals between the different carrier gases are consistently in the ratio 1:∼1/3:∼1/7 (Ar:Kr:Xe). In Section 4.2.2 it was given that the coldest and most intense molecular beams are achieved when the backing pressure is 5 bar for Ar carried beams and 3 bar for Xe carried beams. When directly cooling the valve, to achieve slower beam velocities, the molecular signal rapidly drops as the source temperature decreases.

At high enough pressures or low enough temperatures, inert gas atoms expanding from a nozzle condense to form clusters, held together by van der Waals forces. It is believed that these clusters limit the molecular flux we observe from our source because the molecules become trapped on or inside these clusters. The dynamics of cluster formation is approximately characterized through scaling laws that have been determined empirically. These employ a scaling parameter Γ^* known as the Hagena parameter [62] and given by the following relation

$$\Gamma^* = k\frac{(0.74d/\tan\alpha)^{0.85}}{T_0^{2.29}}P_0, \tag{4.15}$$

where d is the nozzle diameter (μm), α the expansion half angle (degrees), P_0 the gas source pressure behind the nozzle (mbar), T_0 the gas source temperature (Kelvin), and k is a species-specific constant characterizing bond formation. Relevant values of k are: k_{Ar}=1650 and k_{Xe}=5500. Cluster formation becomes significant for large values of Γ^*. This happens when the backing pressure is high, the source temperature is low and a gas such as Xe is used. The threshold for cluster formation depends sensitively on the type of nozzle source, however cluster formation is generally found to occur for Γ^* >100-300, with the mean cluster size N_c (mean number of atoms per cluster) given by [63]

$$N_c = 33\left(\frac{\Gamma^*}{1000}\right)^{2-2.5}, \tag{4.16}$$

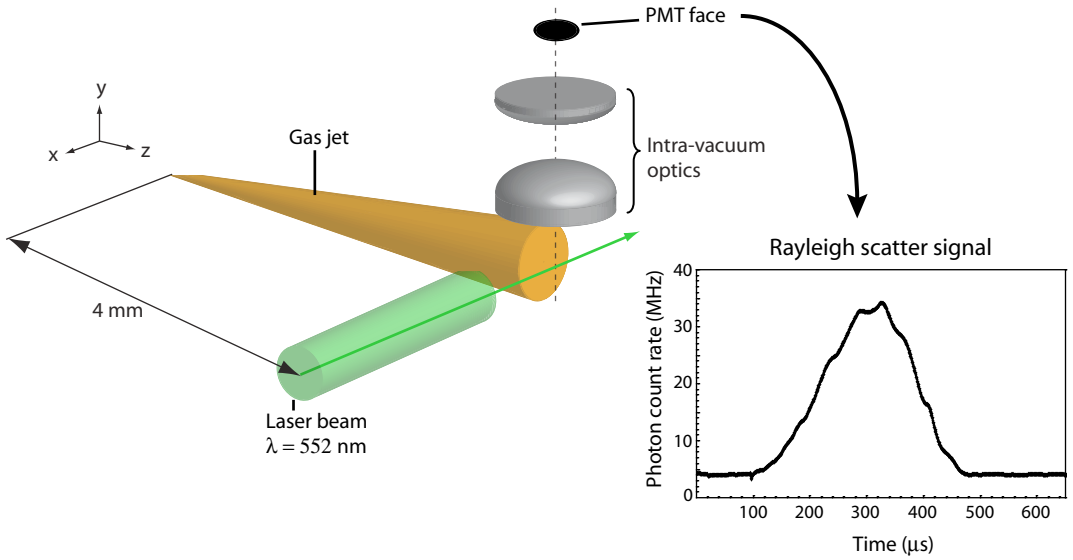

Figure 4.11: Experimental setup for the detection of laser Rayleigh scatter from the inert gas clusters. Lower right inset shows the scatter signal from cooled Xe clusters detected by the PMT.

where the exponent, $2 - 2.5$, is a range. Thus the mean cluster size is very sensitive on the source parameters P_0 and T_0. Substituting parameters applicable to our pulsed jet source into Equations (4.15) and (4.16): 1 mm nozzle diameter, 5 bar stagnation pressure and assuming an expansion half angle of 30^o gives Hagena parameters 8100 and 27000, for Ar and Xe, respectively at 293 K. These values for the Hagena parameter suggest we are well within the clustering regime. The mean cluster sizes for room temperature Ar and Xe are N_c= 4.5×10^3 and 7.6×10^4 atoms, respectively. For Xe at 193 K the mean cluster size becomes 4.7×10^5. Molecules trapped in these clusters will be inaccessible to the experiment; the increased predominance of clusters in jets using heavier inert gas atoms is consistent with the observation that the molecular yield is always lower with Xe carrier gas than with Ar. Furthermore the observed loss in molecular signal as the source temperature is lowered, Figure (4.6) (b), is also consistent with the increased formation of clusters at lower temperatures.

4.3.1 Rayleigh Scatter

We probe the clusters in our apparatus using Rayleigh scattering of laser light. The wavelength of the laser light is much longer than the cluster diameter and the laser induces an oscillating dipole in the clusters which re-radiate at the same wavelength as the applied field. The total Rayleigh scattering cross-section for a spherical scatterer σ is [62]

$$\sigma = \frac{8\pi r^6}{3\lambda^4}\left(\frac{n^2-1}{n^2+2}\right)^2, \tag{4.17}$$

where r is the particle radius, λ is the wavelength of the incident laser light and n is the refractive index of the scattering medium. As the inert gas clusters have no permanent dipole moment, the re-radiated light has the same polarization direction as the incident laser beam. Figure (4.11) shows a schematic of the Rayleigh scattering and detection setup: a 552 nm laser beam crosses the gas jet at right angles, with their intersection 4 mm downstream of the nozzle. With the laser beam polarized in the xz–plane, the intensity of the Rayleigh scattered light will be zero along the direction of the gas jet and greatest in the xy–plane. The scattered light is collected and focussed, by intra-vacuum optics, on to the face of a PMT. A half-wave plate is used to adjust the incident laser beam polarization such that the scattered light signal is maximized. The PMT signal is passed via an amplifier to the experiments control computer and time-resolved data is acquired. The inset to the lower-right of Figure (4.11) shows a real Rayleigh scatter signal from a Xe gas jet that has been pre-cooled to -50^{o}C. The horizontal axis shows time relative to when the valve first opens and the vertical axis gives the detected photon count rate. These latter values are determined from the voltage output of the PMT amplifier using the known calibration between output voltage and detected photon count rate.

To maximize the signal-to-noise on the Rayleigh scatter signal it was very important to block stray light from room lights and prevent the scatter of the incident laser beam off metal surfaces inside the source chamber. The former was achieved by covering all windows attached to the source chamber, except to allow the detection laser beam into and out of the vacuum chamber. Due to the close proximity of the laser beam to the face of the valve, it was vital to remove the ablation target holder, so that the laser beam would not strike it and scatter light into the PMT, as this would have completely masked the Rayleigh scatter signal. Unfortunately this precluded the simultaneous detection of Rayleigh scattering at the source and molecular detection further downstream.

We measured the Rayleigh scatter signal as a function of the source parameters P_0 and T_0 and confirm that we do indeed see clustering that scales in accordance with Equations (4.15) and (4.16). Figure (4.12) shows the observed Rayleigh scatter signal (black data points) increasing as the source pressure is increased for (a) Xe and (b) Ar gas jets. Comparing these two data sets we see that, as expected, the scatter signal for Xe jets is considerably larger than for Ar jets at the same backing pressure. The red curves shown in Figure (4.12) are the expected dependence of the cluster scatter signal as a function of the backing pressure. The total scatter signal S is proportional to the scattering cross-section σ and the cluster number density n_c, $S \propto \sigma n_c$. For our source parameters we expect to be well within the clustering regime so that the average number of atoms per cluster N_c follows the scaling in Equation (4.16). Assuming that the majority of the atoms in the beam condense into clusters, then the cluster number density is $n_c \approx n_0/N_c$ where n_0 is the monomer density before clustering. For spherical clusters, N_c is proportional to the volume of the cluster $\sim R_c^3$

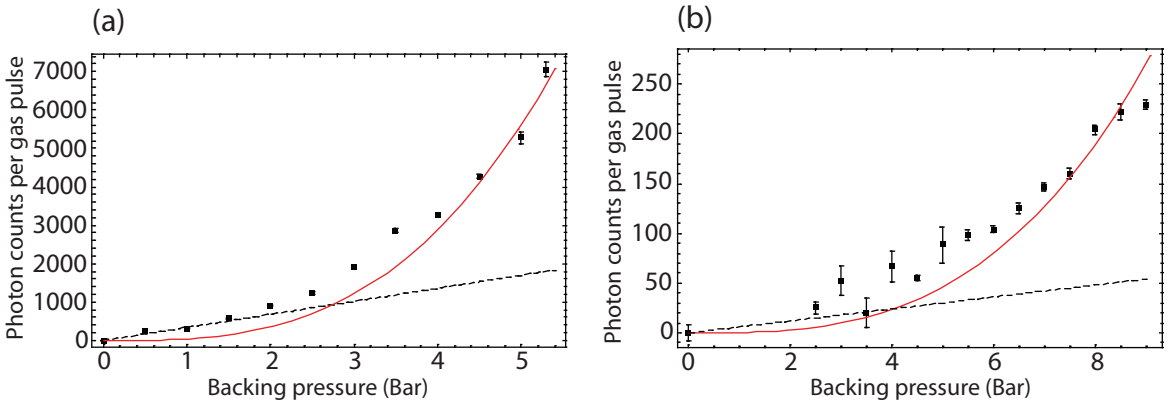

Figure 4.12: Detection of Rayleigh scattering of laser light by carrier gas pulses as a function of stagnation pressure. (a) Scatter signal from Xe gas jet (black points). The red line scales as $S \propto P^3$, and shows good agreement with the cluster signal data above 4 bar. The dashed line follows the linear increase in scatter signal for low source pressures. (b) Scatter signal from Ar gas jet (black points). The red curve, $S \propto P^3$, is the expected relation for the scatter signal from clusters and the dashed line is the expected linear increase in scatter for low source pressures. The lack of clear transition between linear and cubic suggest that atoms and clusters are simultaneously present in the beam over a wide range of source pressures. All this data was taken with the source at room temperature, 22^{o}C.

where R_c is the cluster radius. Using Equation (4.17) and $n_c = n_0/N_c$ we find that the scatter signal from clusters is $S \propto N_c n_0$. At a fixed point downstream of the nozzle the monomer density for an ideal gas is proportional to the gas density behind the nozzle and so $n_0 \propto P_0$ and so we have $S \propto N_c P_0$. Using Equations (4.15) and (4.16) the scattered light signal scales with the backing pressure as $S \propto P_0^{3.0-3.5}$, where (3.0-3.5) is a range.

Figure (12) (a) shows that a $S \propto P^3$ dependence is a good fit to the observed Xe cluster signal for source pressures above 4 bar. However, the scaling suggests a much more rapid decline than was observed in the scatter signal as the source pressure is reduced below 4 bar. This pressure dependence was derived assuming all monomers in the beam had condensed into clusters. In reality, in the limit of no clustering the beam solely consists of monomers and the scatter signal in this case would depend linearly on the backing pressure. Indeed, up to 2 bar the scatter signal follows a linear relation with source pressure, shown by the dashed line in Figure (12) (a). Between 2 and 4 bar the scatter signal goes through a transitionary period during which the scatter signal originates from atoms and clusters. The very good agreement between the experimental data and a linear relation for P_0 <2 bar (monomer beam) and a cubic relation for P_0 >4 bar (cluster beam) suggests that the onset of clustering for Xe atoms occurs rapidly and at a backing pressure of 3 bar. Figure (12) (b) shows an approximate fit of $S \propto P_0^3$ (red curve) to the observed clustering of Ar (black points). The agreement is not as good as it was for Xe at high backing pressures. This suggest that we are seeing a beam composed of atoms as well as clusters at P_0= 9 bar. The lack of a clear transition between linear and cubic dependence suggests that transitional period for the onset of cluster

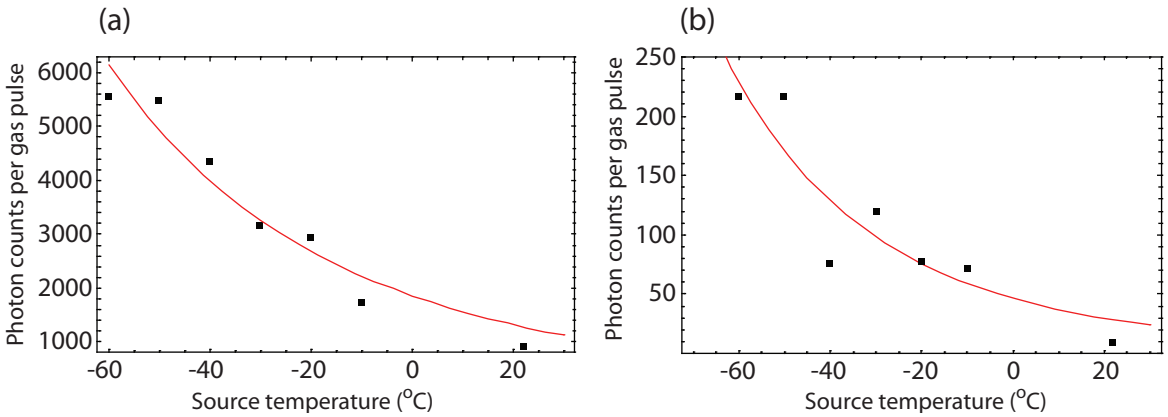

Figure 4.13: Detection of Rayleigh scattering of laser light by (a) Xe and (b) Ar gas pulses as a function of source temperature. The red curves are best fits to the experimental data: for Xe gas jets the scatter signal is well described by $S \propto T_0^{-5}$ and for Ar gas jets the scaling is $S \propto T_0^{-6.4}$. The source pressure was kept the same for Xe and Ar and was 4 bar.

formation in an Ar beam is very much wider than for Xe. The source pressures characterizing the threshold for significant cluster formation are the same as those used when maximizing the molecular beam intensity: 3 bar when seeded in Xe and 5 bar when seeded in Ar.

Clustering in our gas jet was measured as a function of source temperature too. Figure (4.13) (a) and (b) show the Rayleigh scatter signal for (a) Xe and (b) Ar beams as the source temperature is reduced. As expected, the cluster signal in a Xe beam is much larger than that for an Ar beam at the same temperature. As the temperature is reduced from room temperature to -60^{o}C the scatter signal increases by factor $\sim$3 for both Xe and Ar beams. Following the same procedure as for the scatter signal versus P_0, but observing that the monomer density for an ideal gas in the beam is inversely proportional to the source temperature, we find the expected scatter signal scales as $S \propto T_0^{-(5.6-6.7)}$, where $(5.6 - 6.7)$ is a range. Different best fit curves were found for the Xe and Ar scatter signals: for Xe good agreement is found for the scaling $S \propto T_0^{-5}$ and for Ar this is $S \propto T_0^{-6.4}$. It is unknown why the Xe and Ar cluster beams should follow different scalings but they nevertheless lie within or close to the expected range.

We see the observed Rayleigh scatter follow the expected behaviour of a beam composed of clusters as a function of the inert gas used, the source pressure and the source temperature. The observed cluster formation dynamics correlate with our molecular signal intensities and this correlation lends support to the idea that molecules are trapped by the clusters in our beam, thus limiting the molecular flux.

Chapter 5

Guiding and Deceleration of YbF and CaF

In this chapter I discuss and present the guiding and deceleration of YbF and CaF molecular beams using our Stark decelerator.

The Stark decelerator's guiding properties are studied here under a wide range of beam parameters. In particular, the voltages applied to the decelerator electrodes were continuously tuned from zero to high-voltage values. This effected an increase in the transverse acceptance of the decelerator, however, the rise in transmission of molecules through the decelerator was not as large as expected. Several simulations, with varying degree of complexity, reveal why this is so.

Next I present the results of decelerating YbF and CaF molecular beams. With the decelerator turned on, the observed time-of-flight profiles reveal a peak of molecules bunched around the expected arrival time of the synchronous molecule that is delayed with respect to the mean arrival time of the molecules with the decelerator turned off; a subset of the original pulse of molecules has been bunched and decelerated. Our setup allows us to program in any desired timing sequence for the switched applied voltages, yielding accelerated packages of molecules as well as decelerated ones. As explained in Chapter 2, by operating the decelerator at higher phase angles, i.e. using a switching pattern for which the synchronous molecule is further up the Stark potential hill when the voltages are turned off, not only yields slower bunched molecules, but also leads to less intense beams as the longitudinal acceptance decreases. Velocity distributions of the molecular beams are also shown to help understand and properly identify structure in the time-of-flight profile data.

5.1 Guiding

When operating the Stark decelerator as a guide, the lens electrodes are charged in such a way that the mean beam velocity on exiting a lens is equal to the entry beam velocity. The

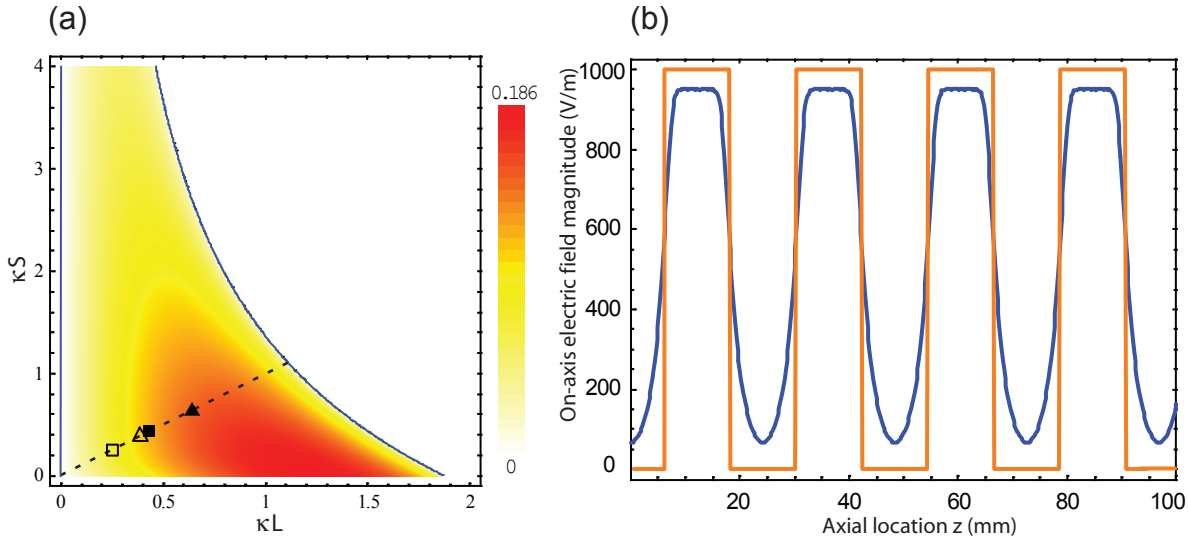

Figure 5.1: (a) Acceptance in one transverse direction of an infinitely long **FODO** array as a function of κL and κS. The acceptance is in units of $d^2\Omega$. The blue contours indicate the boundary of the acceptance where $|Trace(\mathbf{FODO})| = 2$. The dashed line corresponds to the case of equal lens and drift lengths. The operating points represented by the filled and unfilled boxes and triangles are explained in the text. (b) The axial electric field magnitude when the lenses are charged to ± 1 kV is shown by the blue curve and the orange curve is a step-like approximation to the actual electric field pattern with L=S=24 mm.

lenses are approximately harmonic, giving rise to transverse motion that is characterized by two frequencies; a micromotion superimposed on a macromotion. The wavelength of the micromotion is fixed by the lens periodicity whilst the wavelength of the macromotion is dependent on the focusing strength κ of the lenses and their length L. In Chapter 2 it was observed that $\frac{\kappa}{2\pi}$ is the number of transverse oscillations per unit length of lens; a stronger lens brings about more ocillations per unit length of lens. For ease of reference I repeat the equation for κ here

$$\kappa = \sqrt{\frac{\mu_{eff}}{m v_z^2} \frac{2\eta E_0}{r_0^2}}, \tag{5.1}$$

where μ_{eff}/m is the dipole moment-to-mass ratio of the molecule, v_z the axial velocity, E_0 the on axis electric field, η an electric field expansion coefficient and r_0 half the gap between the electrodes in a lens. The amplitude of the macromotion and micromotion is governed by the focusing strength of each lens. As κ is increased the amplitude of the macromotion decreases and the amplitude of the micromotion increases. However, if κ is too high the motion becomes unstable. By choosing an optimum κ and lens length the transverse acceptance of the Stark decelerator can be maximized and thereby increase the flux of molecules through the decelerator.

The AG array has a fixed periodicity, so by appropriate choice of beam velocity and

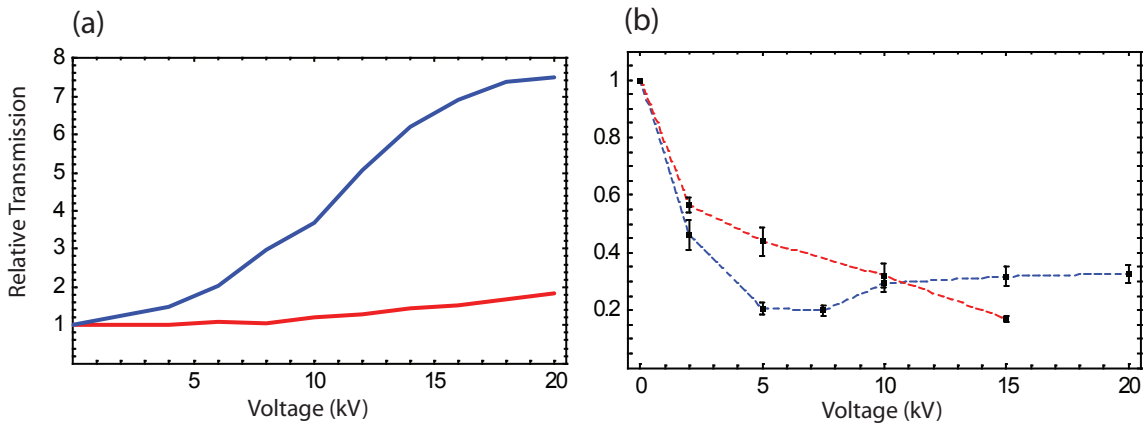

Figure 5.2: Focussing of YbF molecules. (a) Results of a matrix calculation simulating the transmission of YbF molecules through an ideal set of lenses when travelling at 350 m/s (blue curve) and 590 m/s (red curve). (b) Experimental results of the transmission of YbF molecules travelling at 350 m/s (data joined by blue dotted line) and at 593 m/s (data joined by red dotted curve).

applied voltage for a given molecule, one can optimize the value of κ for maximum acceptance. Figure (5.1) (a) shows these operating conditions as points on a plot of the transverse acceptance of an infinitely long $FODO$ lens array. The background theory explaining how this is calculated is in Section 2.4 of Chapter 2. The square points represent beams of YbF whilst the triangular points are for beams of CaF molecules. An unfilled point is used for a fast beam of 590 m/s, whilst a filled point is used for a slow beam of 360 m/s. All the points were calculated with an applied voltage of ± 15 kV. All these points lie on the dashed line for which the lens length, L, and the drift length, S, are equal. The magnitude of the electric field on the molecular beam axis is plotted as the blue curve in Figure (5.1) (b). The orange curve indicates our approximating the electric field pattern to the case where $L = S = 12$ mm, which corresponds to the maximum possible lens length in this decelerator. Of course we can shorten the lenses by switching the high voltage off, with a corresponding increase in the drift length; however this would mean working in regions of relatively low transverse acceptance above the dashed line and so was not pursued.

By scanning the applied voltage for a given molecular beam, the value of κ and hence the transverse acceptance of the decelerator can be continuously varied thus sampling points along the entire dashed line. The effect of changing κ in this way can be measured by the change in fluorescence signal at the detector. Applying this experimental procedure for different beam velocities and molecular species forms the basis of all the experimental guiding data shown in this chapter.

For an infinitely long AG array the transverse acceptance, Figure (5.1) (a) is zero at the origin when zero volts are applied and slowly rises as we progress away from it with increasing voltage. However, the actual decelerator is not infinitely long and at zero volts there will be a set of molecules whose initial conditions are such that they pass naturally through to the

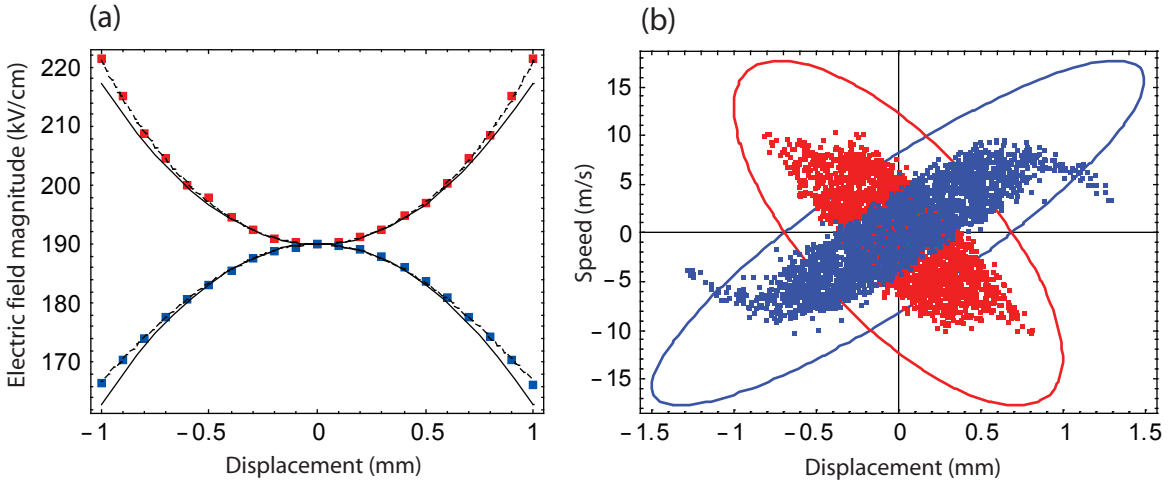

Figure 5.3: (a) The electric field magnitude along the x–axis (red points) and y–axis (blue points) for applied voltages of ±20 kV/cm. The full lines represent the electric field expansion evaluated up to second order whilst the dashed lines up to fourth order. (b) The transverse acceptance of the decelerator for YbF molecules with ±56 kV applied to the electrodes. The accepted (x, v_x) and (y, v_y) coordinates are plotted as red and blue points. The two ellipses represent the boundary of the transverse acceptance in the case of ideal lenses using the same colour coding as with the aberrant lenses.

detector. As the voltage is raised, the net focusing effect of the lenses increases the number of detected molecules. Figure (5.2) (a) shows the calculated transmission of a beam of YbF molecules by the Stark decelerator for two different beam velocities, 350 m/s (blue curve) and 590 m/s (red curve). The transmission increases more slowly for the faster beam because these molecules spend less time inside the lenses and so their effect is consequently smaller. This is consistent with Figure (5.1) (a); the transmission of a 590 m/s YbF beam as a function of voltage terminates at a point (empty box) that has a smaller value of κ and transverse acceptance, than does an identical voltage scan for a slower 350 m/s beam (full box).

Figure (5.2) (b) is experimental data showing the relative YbF signal, normalized to that at zero volts, for the same beam velocities as in the simulation. For both beam velocities the transmission rapidly decreases as the voltage is increased. In the case of a 350 m/s beam of YbF the transmission briefly rises when the applied voltage increases above 6 kV reaching a plateau afterwards. For a 593 m/s beam, the transmission simply decreases over the same voltage range. The rather large discrepancy between the experimental data and the theory indicates the calculation is too simple.

The calculation shown in Figure (5.2) (a) utilizes the transfer matrix formalism to project a distribution of molecular coordinates from the beam source to the decelerator via a skimmer. The known total transfer matrix for the decelerator, $(FODO)^{10}F$ in the yz–plane and $(DOFO)^{10}D$ in the xz–plane, projects these coordinates through to the exit of the decelerator where they finally drift to the detection region. The initial distribution of transverse coordinates is randomly assigned within fixed limits, chosen wide enough to fill the accep-

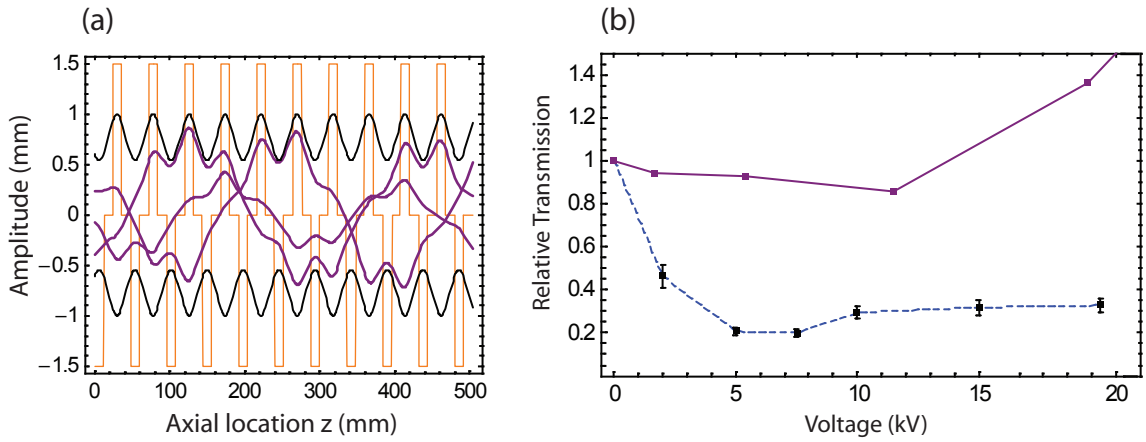

Figure 5.4: (a) A collection of trajectories of molecules (purple curves) inside the decelerator with aberrant lenses exhibits the same behaviour as with ideal lenses: they have their maximum amplitude in the middle of the focusing lenses (positive going orange steps), minimum amplitude in the middle of the defocusing lenses (negative going orange steps) and the micromotion component of the trajectories closely matches the beam envelope (black curves) calculated in the ideal case. (b) Transmission of a 350 m/s beam of YbF molecules by the decelerator with aberrant lenses (data joined by purple line). The experimentally observed transmission of a 350 m/s beam of YbF (data joined by dashed blue curve) is included.

tance of the decelerator, whilst the axial velocity v_z and position z are the same for all the molecules.

Deriving the transverse acceptance of an ideal AG lens array rests on the assumption that the transverse electric field is harmonic, $E(x, y) \propto (x^2 - y^2)$. This ensures that the equations of motion for the transverse coordinates have the form, $\partial^2 x/\partial z^2 \pm \kappa^2 x = 0$, the signs of which correspond to linear focusing and defocusing forces respectively. However, as seen in Chapter 2, the expansion of the electric field magnitude for an infinitely long two–electrode electrostatic lens contains higher order terms as well. Written up to order $\mathcal{O}(x^4, y^4, x^2y^2)$, this expansion is repeated here

$$E(X, Y) = E_0 \left(1 + \eta(X^2 - Y^2) + \eta^2(X^4 + Y^4 - 4X^2Y^2)\right), \tag{5.2}$$

where η is an expansion coefficient and the x and y displacements have been written as $X = x/r_0$ and $Y = y/r_0$, r_0 being half the gap between the electrodes.

I will now improve on the matrix calculation for the transmission of molecules through the decelerator by paying attention to the higher order term in Equation (5.2). Figure (5.3) (a) shows the electric field magnitude along the x axis (red points) and along the y axis (blue points) inside a lens. This data was derived from the output of a finite element model of the decelerator lens [42]. Also plotted is the electric field expansion $E(X, 0)$ and $E(0, Y)$ assuming only harmonic contribution (full lines) and then with terms up to fourth order included (dashed lines). Away from the molecular beam axis, the transverse force is not

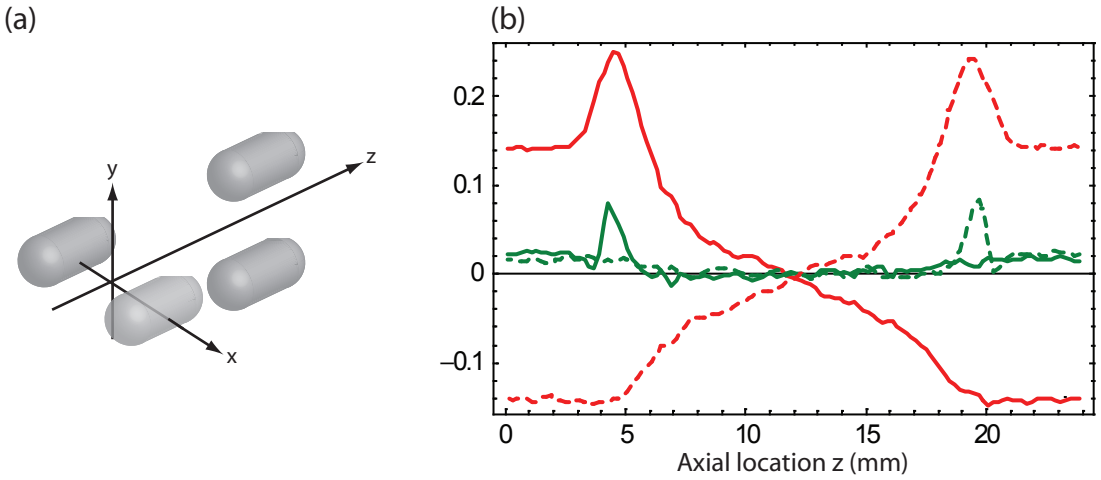

Figure 5.5: Fringe field between two lens stages. The electrodes are arranged as in (a) and the origin of the coordinate system is at the centre of the first lens. A polynomial of the form $f(q) = 1 + aq^2 + bq^4$ is fitted to the transverse electric field along the x and y axes. The variable q denotes transverse displacement. (b) Variation of the fitting variables a (red curves) and b (green curves) beginning at the centre of one lens 24 mm to the centre of the next lens. Full (dashed) lines are fits to the electric field magnitude along the $x(y)$–axis.

harmonic: the actual strength of the electric field is higher in the defocusing plane and lower in the focusing plane than that expected from the harmonic approximation. It is evident that the harmonic approximation of the transverse electric field has limited validity and that an evaluation of the field up to fourth order accurately describes the transverse field up to the electrode surfaces.

Numerically solving the equations of motion with the electric field written up to fourth order and in the strong field limit, yields the transverse phase space acceptance of the decelerator. This simulation was repeated for various values of the applied voltage and Figure (5.3) (b) shows the acceptance at the decelerator's entrance for an applied voltage of ±56 kV; the x-v_x coordinates in blue overlay the y-v_y coordinates in red. For the same applied voltage, the boundary of the transverse acceptance of a decelerator composed of harmonic lenses is also shown by the blue and red ellipses, derived analytically using the Courant–Snyder formalism. The reader is directed to Chapter 2 for details of this calculation. This figure shows that the lens aberrations induced by the higher order terms in the transverse electric field have the effect of reducing the transverse acceptance and distorting the shape of the accepted area away from the ideal ellipse. The ±1 mm spatial limits of the xv_x–ellipse are consistent with the electrodes of the first lens being in the xz–plane. As this lens is focusing in the yz–plane there are no obstructions to the molecules trajectories in this plane and so the spatial limits of yv_y–ellipse can exceed ±1 mm. Some points lie outside the elliptical boundary in (y, v_y)–phase space; these are an artefact of the finite length of the decelerator and disappear as the decelerator is made longer.

Figure (5.4) (a) shows the x–component of these trajectories as a function of axial location within the decelerator. Superimposed on the trajectories is the spatial pattern (orange) of the lenses in the xz–plane; a positive going step indicates that the lens is focusing at that axial location, whilst a negative going step indicates that the lens is defocusing. The trajectories of the accepted molecules still exhibit a micromotion superimposed on the macromotion, and the collection of all the accepted trajectories still has its maximum in the middle of the focusing lenses.

Having run this simulation for several different voltages, we plot the transmission of a 350 m/s YbF beam as a function of the voltage in Figure (5.4) (b); simulated data is joined by a purple line and experimental data is joined by a blue dashed line. This model shows improved agreement with the experimental findings; it now indicates that up to ± 11 kV, the relative transmission indeed drops below unity, after which it begins to increase as the voltage is raised further. To recapitulate, this model is for a finite length decelerator whose transverse electric field profile uses the same electric field expansion as for infinitely long electrodes with anharmonic terms included. Using this electric field expansion, the equations of motion for an initial distribution of molecules has been numerically solved and those that pass through the decelerator kept. Molecules that are kept are taken to represent the transmission that we are expecting to see. Implicit, is the assumption that the source emittance is sufficiently large that it is obstructed by the skimmer aperture. This is true in our experimental apparatus as the Doppler contribution $\approx$4 MHz, necessary to explain the observed line width of the Q(0) transition, is due to a source with transverse extent $\approx$2.4 mm (see Chapter 4 Section 4.2.3). This is larger than the 2 mm skimmer aperture. Thus, calculating the overlap between the acceptance of the decelerator and the skimmer aperture is sufficient to determine the transmission.

Including the non-linear terms into the electric field has reduced the expected transmission of molecules relative to the case of harmonic fields and is in better agreement with the observed transmission. However the experimentally observed drop in signal at low voltage suggests that these non-linear terms might be stronger in reality. Up till now, the lenses, whether harmonic or anharmonic, terminated at the edge of the lens after which the molecules drift to the next lens. An important feature that has not been considered so far is the behaviour of the transverse electric field in the fringe field region of a lens. In this region we have seen, Figure (2.6) in Chapter 2, that the effective transverse spring constants do not smoothly drop to zero as we move away from a lens. In fact, the defocusing spring constant rapidly increases and peaks in these regions before subsequently dropping to zero. This "kick" is a significant loss mechanism, as it disrupts what would otherwise be stable periodic trajectories out of the decelerator.

The role of the various terms in the electric field expansion, Equation (5.2), are now

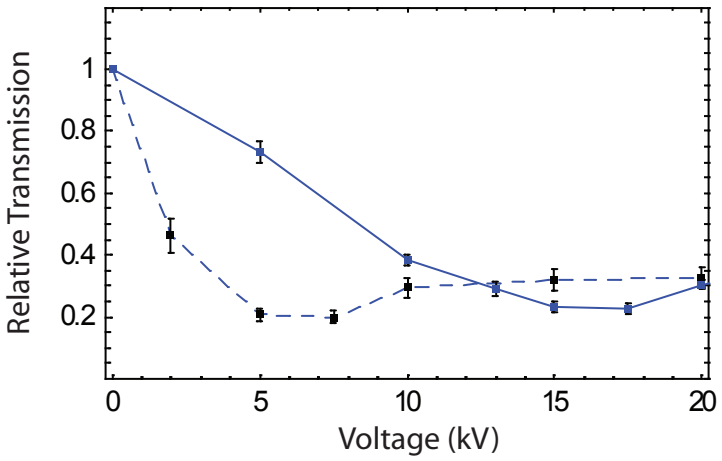

Figure 5.6: Improved simulation of the transmission of YbF molecules through the decelerator when travelling at 350 m/s (full blue curve) that includes non-linearities in the field and the effect of the fringe fields. Experimental results of the transmission of YbF molecules travelling at 350 m/s (data joined by blue dotted line).

considered in the fringe field region [1]. Two adjacent lenses are arranged as in Figure (5.5) (a). The function $f(q) = 1 + aq^2 + bq^4$, where $q = x$ or y, is chosen to represent the electric field along the x–axis and along the y–axis. Comparison with the electric field expansion shows that in the middle of the first lens $a = +\eta$ in the xz–plane and $a = -\eta$ in the yz–plane, and $b = \eta^2$. As adjacent lenses are at right angles to each other, the sign of a switches inside the next lens. Figure (5.5) (b) shows how the fitting parameters a (red curves) and b (green curves) vary as we move from the middle of the first lens 24 mm to the middle of the next lens. The full lines indicate the fit in the xz–plane whilst the dashed curves indicate the fit to the field in the yz–plane. The values of a and b inside a lens agree with those for the infinitely long rods, $\eta = 0.143$ and $\eta^2 = 0.02$ respectively, whilst the large increase in a, and also b, in the defocusing direction of both lenses in the fringe field regions is also evident. The localized increase in the harmonic and higher order coefficients along the defocusing direction comes about because the electric field is non-uniform along the z–axis. As the total electric field is divergence-less, $\nabla \cdot \mathbf{E} = 0$, the field gradients in the transverse plane must rapidly change to accommodate the non-zero axial gradient. At the exit of the lens it is the field gradient along the defocusing axis that significantly increases. Later on we will see how modifying the electrode geometry to include four charged rods rather than two substantially improves this situation.

A third generation model that includes the fringe fields of the lenses, most accurately simulates the transmission of molecules through the decelerator. Due to the complexity of the fringe field, the complete 3–dimensional electrostatic field of a lens is calculated using a

[1] This form for the electric field expansion is only valid when there no field gradients in the z–direction. Nevertheless we find it useful to fit the electric field distribution on a given xy–pane to this form.

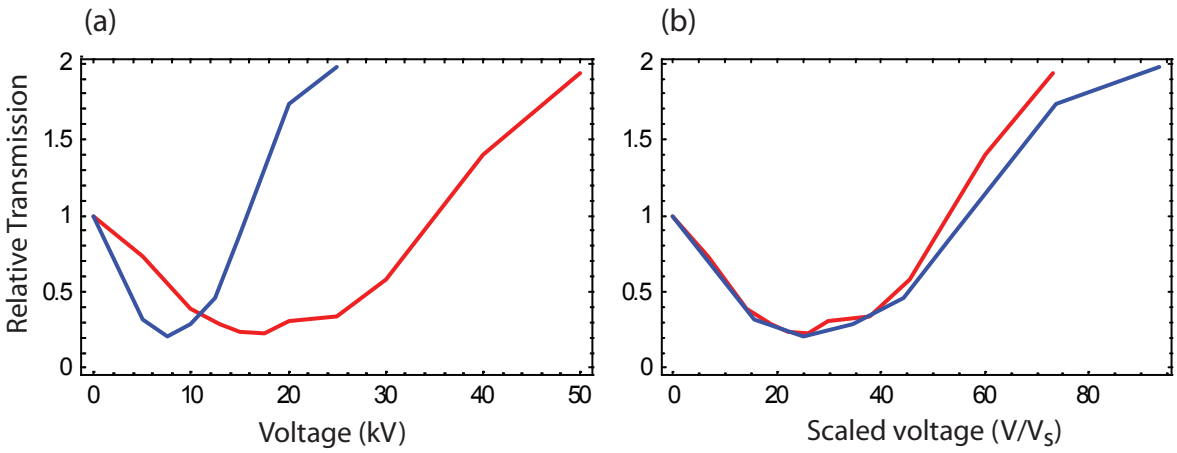

Figure 5.7: (a) Simulated transmission curves for 350 m/s beams of YbF (red) and CaF (blue) as a function of applied voltage. (b) Transforming the voltage axis of the previous transmission curves into dimensionless units using $V_s = (2 \times 10^{-7}) m v_z^2 r_0 / \mu_{eff}$ brings the two transmission curves on top of one another.

finite-element program. The Stark shift is calculated at each grid point of the electric field map and the force on a molecule is determined by the gradient of the Stark shift at that location, thus the trajectory of a molecule is constructed. This calculation also includes the higher order terms present in the real electric field between the electrodes. The coordinates of the molecules are assigned at the source and occupy the full 6–dimensional phase space (x, y, z, v_x, v_y, v_z). Those trajectories that make it through the decelerator are kept and determine the transmission of the decelerator. Figure (5.6) shows the transmission of a 350 m/s beam of YbF molecules (blue full curve) as a function of the applied voltage based on this 3–dimensional trajectory simulation. The resulting transmission curve is now very similar to the observed one (blue dashed curve). By including the fringe fields the simulated transmission curve now exhibits the same significant drop in transmission with increasing voltage and the 20% minimum transmission is in agreement with the experimentally observed value, although they occur at different applied voltages. The source for this discrepancy will be discussed later on.

The low YbF transmission at high voltage is undesirable; however, it does improve as the voltage is raised further above ±20 kV. The focusing strength of the lenses can also be increased by reducing the beam speed. The lowest YbF beam speed, using pre-cooled Xe, is 294 m/s. For this speed, the transverse acceptance is maximized at ±29 kV. This voltage is still rather large and difficult in practice to work with, as the risk of discharges between the electrodes is high. Accessing the high transverse acceptance of the decelerator is still possible if a different molecule is guided; as seen by Equation (5.1), a molecule that has a larger dipole moment-to-mass ratio than YbF, will have a larger value of κ. Figure (5.7) (a) shows the expected transmission for 350 m/s beams of YbF (red) and CaF (blue) both calculated

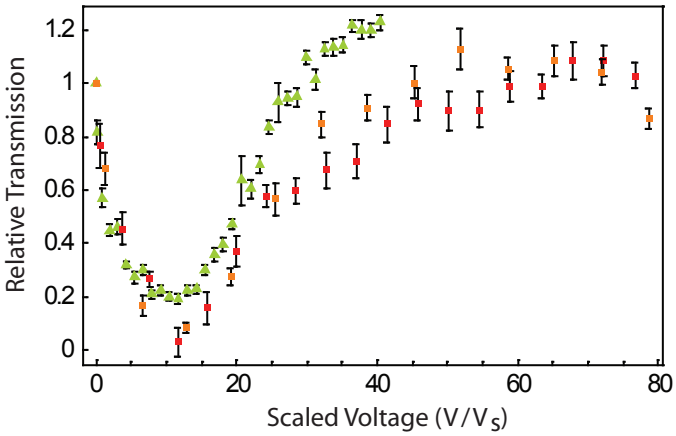

Figure 5.8: The transmission of 364 m/s beams of CaF molecules as a function of the scaled applied voltage, detected using 0.5 mW (orange data) and 5 mW (red data) laser probe beam powers. The green triangles are the transmission of a faster, 599 m/s, beam of CaF molecules detected using 0.5 mW of laser probe beam power.

using the 3–dimensional trajectory simulation that includes the non-linearities inside the lenses and the fringe field effects. Above ±12 kV, the transmission of CaF is higher, rising above 1 at ±16 kV. This primarily comes about because CaF has a significantly lower mass than YbF, and consequently a larger dipole moment-to-mass ratio. Using the dipole moment and mass of YbF and CaF given in Figure (2.3) in Chapter 2, the ratio $\frac{(\mu/m)_{CaF}}{(\mu/m)_{YbF}}$ is 2.6, and is approximately the scale factor that interchanges the two transmission curves.

We can use κ, a fundamental property of the transverse motion in an AG lens array, to relate all the transmission curves regardless of the molecular species, beam velocity or applied field. This is brought about by re-arranging Equation (5.1) into the dimensionless form

$$(\kappa r_0)^2 = \eta \frac{\mu_{eff} E_0}{\frac{1}{2} m v_z^2}, \tag{5.3}$$

The left hand side of this equation is proportional the ratio of the characteristic interaction energy, $\mu_{eff} E_0$, and the forward kinetic energy, $\frac{1}{2} m v_z^2$, of the molecule. This dimensionless form for κ reveals it's importance as a measure of the strength of the lenses. Equation (2.22) in Chapter 2 shows that the on-axis field E_0 is $\sim V_0/r_0$. Using this and Equation (5.3) we define a scaling voltage $V_s \sim m v_z^2 r_0 / \mu_{eff}$. This result is used to scale all the transmission curves onto the same abscissa scale, regardless of voltage, molecular species or beam velocity. Figure (5.7) (b) shows this scaling implemented on the simulated transmission data for YbF (red curve) and CaF (blue curve) beams with equal velocities. The good agreement suggests that this scaling law is appropriate even when the simulated data includes the effects of aberrant lenses and fringe fields. At high values of κ the CaF and YbF transmission curves slightly deviate from each other, indicating that the effect of anharmonic lenses and the fringe

fields is forcing the dynamics of the molecules away from the ideal case where this scaling applies.

Figure (5.8) shows experimental data for guiding slow and fast beams of CaF molecules. The orange and red data points show the relative transmission of 364 m/s CaF beams detected using 0.5 mW and 5 mW laser power respectively, whilst the green triangular points show the transmission of a 599 m/s CaF beam using 0.5 mW of laser power. As the voltage is raised from zero, the transmission decreases and reaches a minimum at $V/V_s \simeq 10$, above which the transmission increases as the voltage is raised further. Regardless of beam velocity, the transmission curves exhibit similar behaviour, demonstrating the velocity scaling also works with the experimental data.

Different laser powers were used to detect the transmission of slow CaF beams, to improve the detection efficiency. As the voltage increases the focal length of the lens become shorter and there is a consequent increase in the spread of transverse velocities of the molecules. The resonant frequency of some of these molecules may be sufficiently Doppler shifted, due to their larger transverse velocity, that they are no longer resonant with the incident laser beam; these molecules do not get detected. However, by power broadening the Q(0) transition (as discussed in Chapter 4), the line width increases, thus enabling molecules with large transverse velocities to be detected. Using 0.5 mW laser power, the Q(0) FWHM is equal to 30 MHz. This frequency width approximately matches the ±5 mm spatial aperture of the LIF optics along the axis of the laser beam; this is the maximum detection volume allowed by our detection scheme. However, the relative transmission did not change. Raising the laser power even more did not improve the detection signal either.

The observed relative transmission of a fast CaF beam in Figure (5.8) is unexpected; as in theory there should not be any increase in relative transmission for applied voltages in the range 0–±24 kV with such fast beams. The explanation for this discrepancy was revealed when we scanned the laser frequency with the voltage on and with the voltage off. It was found that the Q(0) detection transition is shifted to lower frequencies when the voltages to the decelerator are turned on relative to when they are turned off. All the transmission curves discussed in this chapter are the ratio between the Q(0) resonant amplitude with volts on to the Q(0) amplitude line with volts off; the observed frequency shift makes this ratio frequency dependent, and thus difficult to interpret when the voltage is varied. Figure (5.9) (a) shows a frequency scan across this transition whilst also modulating the lens voltages between zero (red curve) and ±20 kV (blue curve). In each case both hyperfine components are resolved and a function composed of the sum of two Lorentzian functions is fitted to the data (black curves). The frequency shift between the volts on and volts off Q(0) line positions is 11.3±0.5 MHz (approximately one third of the FWHM of the observed line width), and the peak signal intensity is lower when the voltages are turned on relative to when they are off. Figure (5.9) (b) shows the effect on the observed transmission when the laser's frequency

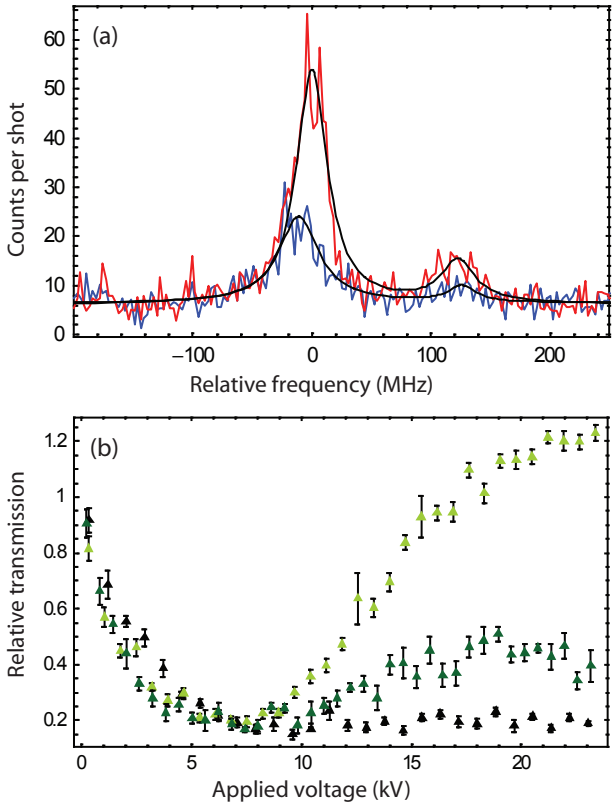

Figure 5.9: The dependence of the transmission curves on laser frequency. (a) Scanning the laser frequency whilst also modulating the applied voltages between zero (red curve) and ±20 kV (blue curve) shows a 11.3±0.5 MHz shift to lower frequency relative to the volts off Q(0) transition. Furthermore the ratio of the peak transition height is 0.36 (volts on/volts off), suggesting 36% transmission of fast molecules through the decelerator. (b) The transmission of 599 m/s CaF beams with the laser frequency locked on resonance (black points), locked $\simeq -5$ MHz (dark green points) and $\simeq -10$ MHz (light green points) relative to the volts off Q(0) line.

is locked on resonance (black triangles), and locked $\simeq -5$ MHz (dark green triangles) and $\simeq -10$ MHz (light green triangles) below resonance for a CaF/Ar beam.

It is clear from the transmission curves in this figure that the frequency shift in the molecular transition makes it difficult to accurately interpret the transmission curves at high voltage. An identical frequency scan with the voltage modulated between ±20 kV and zero volts using a CaF/Xe beam also indicated, although less clearly, a frequency shift to lower frequencies. An important observation from Figure (5.9) (a), is that the relative transmission based on the resonant amplitudes is ≈0.35 (and 0.15 for the CaF/Xe voltage-modulated frequency scan). Thus the real transmission at high voltage is low and not 1 as indicated by the data in Figure (5.8). This may also apply to both sets of CaF/Xe data shown in this figure; the relative transmission is the combined result of the laser frequency being sufficiently below resonance, and the frequency shift to lower frequencies, to yield a molecular signal that comes back to approximately the same value at high voltage.

There are two possible causes that can bring about the observed frequency shift: a Stark shift due to the decelerator's weak electric field in the detection region, or a Doppler shift due to a non-zero centre of mass motion of the molecules along the axis of the laser beam. For all the transmission experiments, the voltage to the decelerator, remained on whilst the molecules moved through the detection region. A weak electric field in the detection region, due to the charged decelerator, would Stark shift the molecular transition. Such a shift, however, would have been to higher frequencies not lower ones as was observed and it would have been voltage-dependent which was not observed.

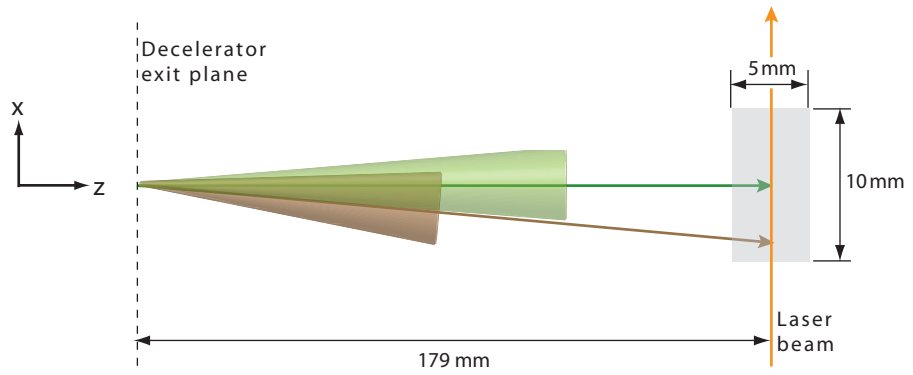

Figure 5.10: Detection geometry for a molecular beam source mis-aligned to the entrance of the decelerator. Deflected (un-deflected) molecular beam is shown in brown (green). The 5×10 mm rectangular aperture is an image of the mask projected from the plane of the PMT face onto the xz-plane.

Alternatively, the Doppler effect, brought about by a non-zero transverse centre of mass motion that is moving antiparallel to the laser beam's axis, is a more likely candidate. This is schematically shown in Figure (5.10). Using $\delta\nu = v_\perp/\lambda$, a Doppler shift $\delta\nu$ of 11.3 MHz corresponds to a transverse velocity $v_\perp$ equal to 7 m/s, where λ=606 nm. This speed is typical of the transverse speeds of molecules inside the decelerator. Given this, we may speculate that the cause of the non-zero transverse motion could be the result of a misalignment between the molecular beam source and the entrance to the decelerator. The alignment of the decelerator with the beam axis was checked and found to be good, and the alignment of the molecular beam source was varied in the vertical plane as well. However, the effect of these changes on the frequency shift was unclear.

A Doppler shift would also imply that only a fraction of the guided molecules are being detected as some may miss the detection area altogether, see Figure (5.10). A deflected molecular beam with 7 m/s transverse speed, will cross the the laser beam 3.6 mm (2.1 mm) from the un-deflected molecular beam axis, assuming the axial speed is 350 m/s (590 m/s). The first displacement misses the detection area altogether and the latter lies close to the boundary of the detection area. This suggests that we are not detecting all the molecules that exit the decelerator. However, when the molecular beam source was translated in the vertical

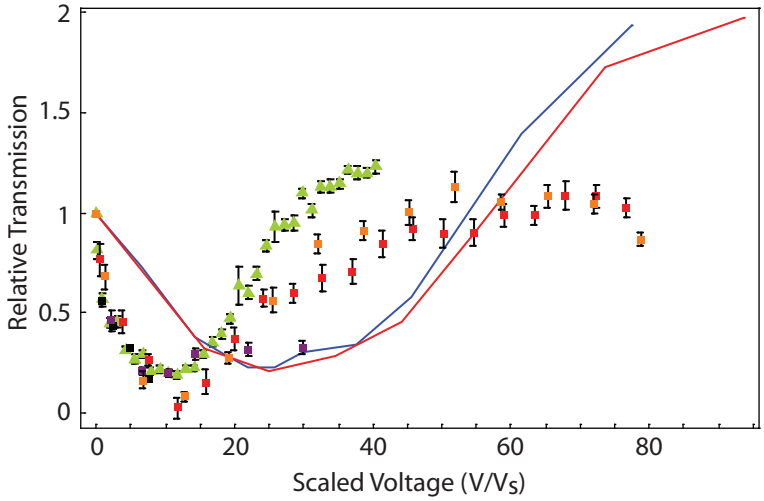

Figure 5.11: Comparison between all the experimental and simulated transmission curves for CaF and YbF molecules using the universal voltage scaling parameter. Experimental data points: YbF/Ar (▪), YbF/Xe (▪), CaF/Ar (▪), and CaF/Xe (▪,▪). Simulated transmission curves: YbF/Xe (—) and CaF/Xe (—).

plane, the relative transmission of CaF beams did not change and remained ≈20%. Thus referring back to the relative transmission curves shown in Figure (5.8), the transmission of CaF/Ar at ±20 kV is ≈20% and it is likely that the transmission of CaF/Xe is also ≈20% at ±20 kV.

In summary, all the experimental transmission data (coloured points) and the 3–dimensional simulations (full curves) are plotted together in Figure (5.10). They all show the same prompt decrease in signal as the voltage is increased and then a rise thereafter, regardless of beam velocity or molecular species. The use of the universal scaling voltage in Figure (5.10) is seen to work remarkably well over a wide parameter range, demonstrating its general applicability even with anharmonic lenses and fringe field effects present. The 3–dimensional trajectory calculations, show that the effects of the fringe field of the lenses has a significant impact on the observed transmission. Above $V/V_s = 10$, the frequency dependence of the relative transmission influences the observed transmission, making direct comparison with the simulated data difficult. The cause of the Q(0) frequency shift remains unknown, however the voltage-modulated frequency scans suggest that the actual relative transmission of CaF/Ar and CaF/Xe is in fact lower than 1 at ±20 kV, they are 0.3 and 0.15 respectively. Although great progress has been made in achieving a quantitative understanding of the transmission, it remains unclear why the experimental minima occur at lower voltages than the theoretical minima. Further work is planned both on the experiment and on the simulation to resolve this question.

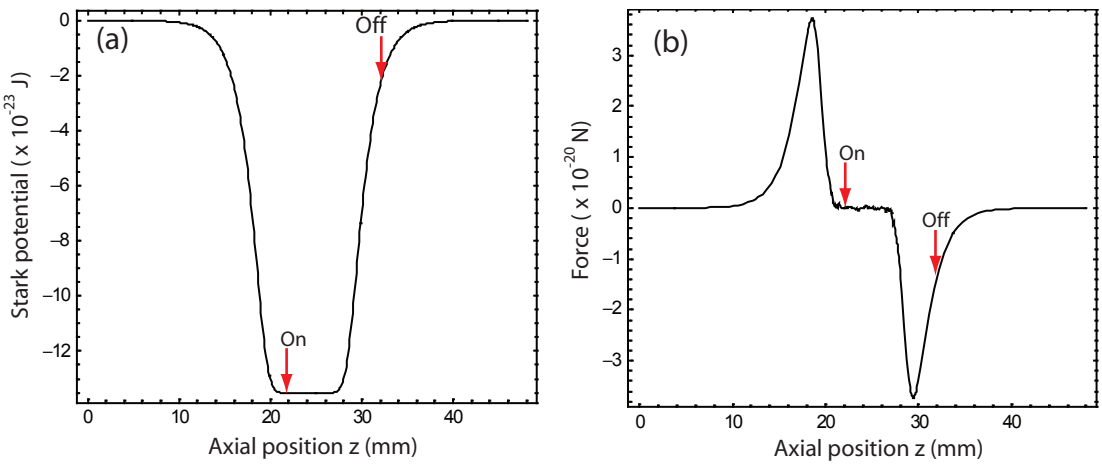

Figure 5.12: Building a timing sequence for the Stark decelerator; (a) The axial Stark potential, $W(z)$, is calculated knowing the Stark shift of the molecule and the axial electric field magnitude for a given applied voltage. (b) The force is calculated using $F(z) = -dW(z)/dz$. The desired *turn on* and *turn off* positions are chosen for the synchronous molecule and due to the translational symmetry of the lens array a full force map along the length of the decelerator is formed. This is used to solve the equation of motion for the synchronous molecule.

5.2 Deceleration

The molecular beam can be decelerated by correctly timing the charging and discharging of the lens electrodes. As the molecules leave the lens, the decreasing field strength produces an axial force which slows them down. The voltage is switched off to avoid re-accelerating the molecules as they enter the next lens. To account for the change in velocity subsequent lenses are switched at time intervals ΔT which gradually get longer as the molecules are decelerated. The variation of ΔT is chosen in such a way that one particular molecule, the synchronous molecule, loses a known and constant amount of energy at each stage. The timing sequence is derived from the requirement that the synchronous molecule is at the same relative position inside all the lenses when the field is switched on and off.

The timing sequence is derived by solving the axial equation of motion for a single molecule $d^2(z(t))/dt^2 = F(z(t))/m$. Knowing the electric field magnitude and Stark shift of the molecule, as shown in Figure(5.12) (a), the axial force is calculated and is defined everywhere along the molecular beam axis, as shown in Figure (5.12) (b). The final form of the axial force $F(z)$ is determined by the desired spatial switching sequence which is defined by two parameters, *turn on* and *turn off* positions. These coordinates dictate how much kinetic energy is lost or gained and are defined within a coordinate system in which the first lens is centered on the position z=24 mm. As the lenses are equidistant from each other, with a period of 24 mm, the turn on and off positions at each lens are simply extrapolated from those values at the first lens. The spatial switching pattern is converted to a time sequence by noting the values of t for which the solution $z(t)$ is equal to the required turn on and turn

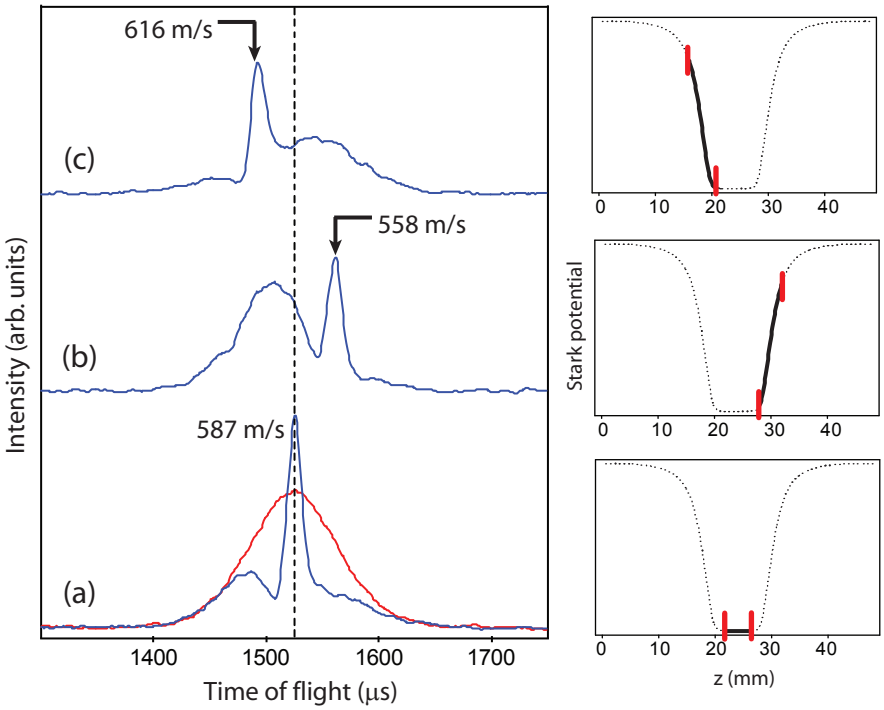

Figure 5.13: Bunching, deceleration, and acceleration of a CaF molecular beam. (a) Based on the mean arrival time (dashed line) of the time of flight distribution with the decelerator turned off (red curve) a switching sequence is chosen that leaves the mean speed of the molecules (587 m/s) unchanged when the decelerator is turned on (blue curve). The narrow central distribution in arrival times demonstrates longitudinal bunching. Using this arrival time, other switching sequences are implemented that (b) decelerates and (c) accelerates the bunched molecules. All the time of flight data have been normalized to the volts off time of flight profile, and the decelerated and accelerated profiles have been offset for clarity. The axial Stark potential seen by the molecules in each case are shown as insets to the right of figure where the red vertical lines indicate the turn on and off positions.

off positions.

The timing sequence is automatically generated by the experiment's control computer after being given the initial velocity, the turn on/off positions and the applied voltage values by the experimenter. The initial velocity of the molecules is determined from the observed time-of-flight distribution with the decelerator off. Figure (5.13) (a) shows an observed time-of-flight distribution of a CaF beam with no voltage applied to the decelerator (red curve); a Gaussian fit to this distribution of arrival times indicates a mean speed of 587 m/s, distributed with a FWHM of 36 m/s. The observed time of flight profiles when the decelerator is charged to ± 15 kV and switched as indicated by the insets to the right of the main figure are shown in blue and demonstrate (a) bunching, (b) deceleration and (c) acceleration of CaF molecules. The expected arrival times of synchronous molecules under these experimental conditions are shown by black arrows which are also labeled by the expected final speed.

With the decelerator turned on, the observed time-of-flight profiles reveal a narrow peak of molecules bunched around the expected arrival time of the synchronous molecule. This

is longitudinal bunching. In Figure (5.13) (a) the speed of the synchronous molecule is equal to the average speed of the molecules when the decelerator is turned off, 587 m/s. The electric fields are switched at equal time intervals such that the synchronous molecule arrives at the same relative position inside the next lens when the fields are turned on again. The synchronous molecule thus sees the same field at each lens, indicated between the red marks in the inset, and it's velocity remains unchanged. A molecule that is further ahead will be decelerated by the rising potential hill, whereas a molecule that lags behind is accelerated. Consequently, they approach the synchronous molecule and eventually the situation is reversed. Thus these molecules oscillate in phase and velocity about the synchronous phase and velocity. These molecules form a bunch around the synchronous molecule and remain trapped in this effective potential well travelling at the velocity of the synchronous molecule. Molecules whose phase and velocity deviate significantly from the synchronous phase and velocity will not be trapped in this travelling potential well and arrive at times on either side of the bunched peak shown in Figure (5.13) (a).

The molecules are decelerated in Figure (5.13) (b) because the synchronous molecule has travelled further up the Stark potential hill before the field is switched off, and has lost kinetic energy. Successive time intervals increase such that the synchronous molecule is at the same relative position inside each lens, shown by the red lines in the inset to the right, and so loses the same kinetic energy at each stage. Other molecules continue to oscillate in phase and velocity, about the synchronous molecule and are also decelerated as the velocity of this effective potential well is lowered. Similarly, by turning the fields on when the synchronous molecule is on the downward slope of the Stark potential and by reducing the time intervals between switching the fields off and on, the bunched molecules accelerate as shown in Figure (5.13) (c). Based on the expected energy loss per stage, shown by the the on/off positions inside the Stark potential, the time of arrival and final speed of the synchronous molecule at the detector is calculated. For a synchronous molecule whose initial velocity is 587 m/s, the final decelerated (accelerated) speed is 558 m/s (616 m/s). This represents a total kinetic energy loss (gain) of 10%.

So far, the presented deceleration data corresponds to molecules moving through a fixed region of the axial electric field, however this region can be continuously scanned so that the molecules move through regions that gradually move up the Stark potential. Figure (5.14) shows the bunched molecules get increasingly slower as they sample a window of the Stark potential which moves along as the time delay between the Q–switch and the start of the deceleration switching sequence increases. The delay is written alongside the corresponding time of flight profile. For short delays, the synchronous molecule has not yet reached the on position when the voltages are applied and sees a flat axial electric field magnitude i.e. it is primarily guided by the decelerator. This is shown by the first time of flight profile (orange data) vertically offset from the time of flight profile when the decelerator is switched off (red

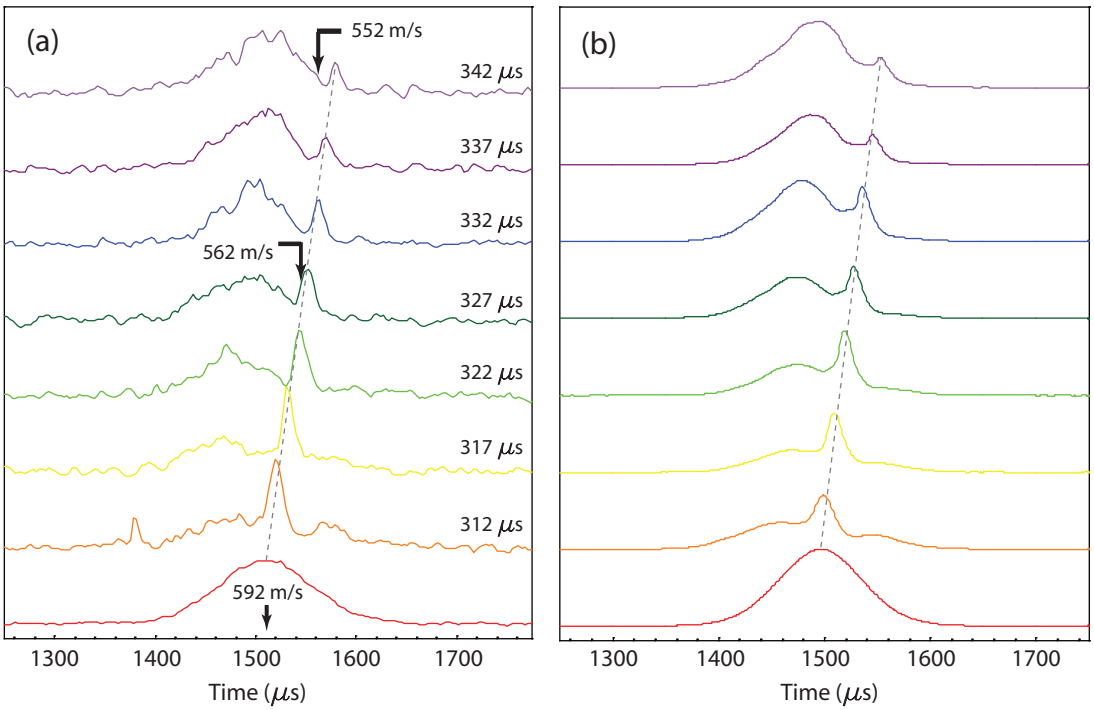

Figure 5.14: Using the decelerator to continuously tune the speed of (a) CaF and (b) YbF molecular beams.

data). As the delay is increased the synchronous molecule sees more of the Stark potential hill and so is decelerated more. Eventually, it arrives at the on position, when the fields are switched on and moves through the intended portion of the electric field; this delay is 327 μs. At this point, the velocity of the synchronous molecule is 562 m/s, and represents a 10% reduction in kinetic energy. The time of arrival of the synchronous molecule is indicated by the arrow drawn in Figure (5.14) and agrees with the observed arrival time of the decelerated bunch. As the delay is made even longer, the synchronous molecule is ahead of the on position when the electrodes are charged and is consequently further up the potential hill when they are discharged, thereby losing more kinetic energy per stage and arriving later in time. The final time of flight profile, with a delay of 342 μs, has moved up the full height of the Stark potential. This corresponds to a 13% loss of the initial kinetic energy, where the final beam velocity of the synchronous molecule is 552 m/s and it's expected time of arrival is shown by the arrow. For this data, the expected arrival time does not agree very well with the observed arrival time of the decelerated bunch of molecules. This model, however, is a very simple one which assumes the energy loss at each lens occurs at one axial position, after which it coasts at the reduced velocity. This is certainly untrue in the experiment as the deceleration force on the molecules act over a finite distance. A more detailed look at the time of flight profiles using calculations of the 3–dimensional trajectories of the molecules will be given shortly.

The above discussion refers specifically to the CaF deceleration data of Figure (5.14) (a).

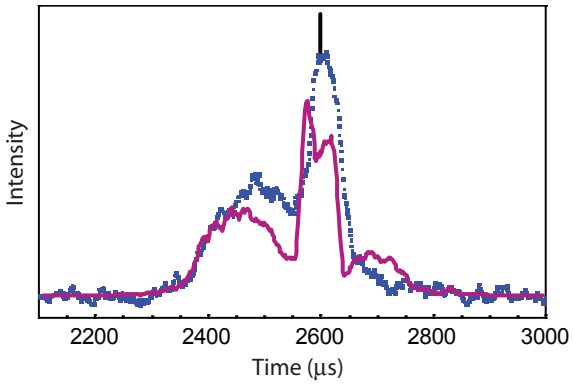

Figure 5.15: Comparison of the experimentally observed deceleration of YbF molecules (blue points) with a 3–dimensional trajectory simulation of the same experiment (purple curve). The expected arrival time of the synchronous molecule whose initial and final speeds are 351 and 332 m/s respectively (for applied voltages ±14 kV) is shown by the vertical black line.

In Figure (5.14) (b) the same experiment is performed for beams of YbF with very similar results obtained.

One other aspect of Figure (5.14), is the loss in intensity of the decelerated bunch of molecules as they move further up the Stark potential. As the synchronous molecule travels further up the potential hill the maximum phase and velocity oscillations of the molecules about the synchronous molecule decrease as they become increasingly limited by the height of the Stark potential. In particular, when the synchronous molecule is very close to the top of the potential hill, those molecules that are ahead will be lost into the next potential well, and be accelerated away. Furthermore those molecules that initially lagged behind the synchronous molecule will eventually pass it, as they lose less kinetic energy per stage, and also leave the travelling potential well.

The observed deceleration data can be looked at more carefully by comparison to the output given by the 3–dimensional trajectory simulations. The simulations use the same operating parameters as are used in the experiment: the initial speed, applied voltage, and on and off positions. The initial coordinates of the molecules in phase space are found in the simulation by replicating the observed time-of-flight profile when no voltage is applied to the decelerator. The deceleration of YbF has been investigated for a 12-stage proto-type alternating gradient decelerator [35] which implemented a $(FO)^3(DO)^3$ lens array. Figure (5.14) shows the experimental (blue points) and simulated (purple curve) deceleration of a slow beam of YbF molecules for the current 21-stage $FODO$ lens array and with applied voltages ±15 kV. Each time-of-flight profile has been normalized to its corresponding zero voltage time-of-flight profile.

Comparing the experimentally observed data with that obtained by simulation we find that the overall shapes are similar and that the arrival time of the decelerated peak coincides in the two cases. However, the simulation shows that the decelerated peak split into two

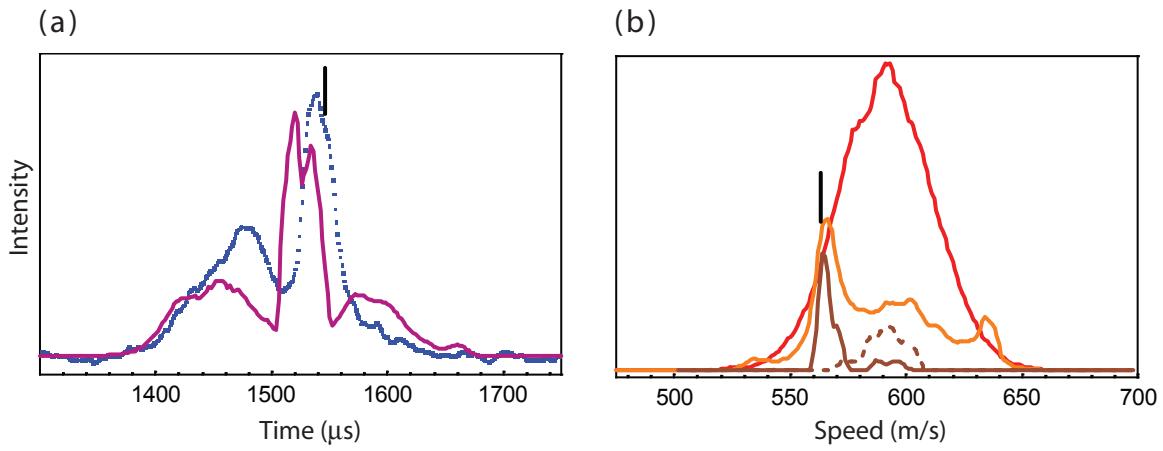

Figure 5.16: (a) Comparison of experimental (blue points) and simulated (purple curve) time-of-flight distributions of decelerated CaF molecules. (b) Velocity distributions derived from the simulations: the red (orange) curve is the complete velocity distribution without (with) applied voltages to the decelerator. The velocity distributions of those molecules arriving inside the left and right peaks are shown separately by the dashed and full brown curves respectively.

parts, a feature not reproduced by the experimental data. The integrated signal is also slightly greater in the experiment than in the simulation. The split in the peak for the simulated data is a reproducible feature. The time of arrival of the peak in the experiment coincides more clearly with the peak on the right, however it is larger and wider. Also shown in Figure (5.15) is the expected arrival time (vertical black line) of the synchronous molecule whose initial and final speeds are 351 m/s and 332 m/s respectively. As already remarked, the integrated signal under the experiment time-of-flight profile is approximately 10% higher than that of the simulation time-of-flight profile. This indicates that when the decelerator is switched at high field, the transmission is better than the simulation predicts. This is in marked contrast to the case of DC high-voltages considered in Section 5.1, where the transmission comes out far smaller in the experiments than in the simulations. The reason for this is unknown at present.

Further understanding of the split peak structure can be obtained by considering the velocity distribution of the molecules emerging from the decelerator. Figure (5.16) (a) shows the experimental and simulated time-of-flight profiles of decelerated CaF molecules. The same features and comparisons can be drawn between these data sets as has been done with those in Figure (5.15) for YbF; principally that the decelerated peak exhibits a split structure which is not evident in the experimental data. On this occasion the observed arrival time of the decelerated peak coincides almost exactly with the right-hand peak in the simulation, the left peak clearly arriving outside this region. This implies that the left peak may well correspond to molecules which do not belong to the phase stable decelerated bunch as was previously assumed. Figure (5.16) (b) shows the calculated velocity distribution of all the molecules that exit the decelerator when the volts are turned on (orange curve) together

with that for no applied voltage (red curve). The orange curve clearly shows the formation of a peak close to the expected final velocity of 562 m/s, which is also indicated by the vertical black line. The specific velocity distributions of those molecules that arrive inside the left and right peak structures are shown by the dashed brown (right) and full brown (left) curves. It is clear that those molecules arriving within the time window of the left peak do not belong to the phase stable decelerated bunch and in fact have an average exit speed equal to the initial beam speed before entry into the decelerator. On the other hand those molecules that arrive within the time window of the right peak have a velocity distribution that coincides very well with the expected final velocity.

These velocity distributions prove very useful in aiding us to understand and interpret the time-of-flight profiles. In particular they discriminate those molecules that have been phase-stably decelerated from those that simply arrive at the same time at the detector. The experiment is currently being modified to allow for a counter-propagating laser beam along the molecular beam axis which will be used to measure directly the axial velocity distributions of our molecular beams. In addition to this, the split peak structure has been recently observed for a small number of deceleration stages, and seen to disappear as the number of deceleration stages is increased. Further detailed work is being carried out to understand this and the deceleration of slow beams of CaF molecules.

Chapter 6

Conclusions and Outlook

6.1 Conclusion

An alternating gradient Stark decelerator has been used to guide and slow beams of YbF and CaF. Using this decelerator I have demonstrated an increased amount of deceleration for the case of YbF, and for the first time, have also decelerated a beam of CaF molecules.

I have developed a new molecular beam source for producing a cold supersonic beam of CaF molecules. The source has been characterized well as a function of carrier gas, source pressure, temperature and the relative timings between opening the valve and ablating the target. This characterization showed that the gas jet and molecular beam translational temperatures are both low, $\sim$3 Kelvin, and that the terminal velocity of the molecular beam is close to the theoretical value. With the appropriate carrier gas and/or by directly cooling the valve, we can tune the velocity of the beam anywhere between 600 m/s and 294 m/s.

Using this molecular source, spectroscopy of the CaF molecule showed the rotational structure of the ground and first excited electronic states of CaF, which compared favourably with the expected pattern of lines based on the published spectroscopic constants. This allowed us to identify the ground ro-vibrational and electronic state, $X^2\Sigma^+(\nu = 0, N = 0)$, necessary for Stark deceleration studies. Both hyperfine components of the ground electronic state, the Q(0) F=1 and Q(0) F=0 transitions, were observed. The Q(0) F=1 transition line shape was studied and measurements of the power broadening of this transition gave a natural line width that agreed very well with the published values.

A study of cluster formation, by the detection of laser Rayleigh scatter close to the nozzle, confirmed that clusters are formed in our gas jet beams, and the dependence of the Rayleigh scatter signal on gas species, source pressure and temperature agrees with the expected scalings. Cluster formation is less prevalent in an Ar beam than in a Xe beam. For Xe, a clear transition from a monomer to a cluster beam occurs at 3 bar, and a similar transition occurs for Ar at 5 bar. The formation of clusters is observed to increase as the source temperature decreases. These results point to a link between the presence of clusters

and the observed molecular beam intensity, as the optimum molecular beam intensity is obtained when the source pressure is 3 bar and 5 bar when using Xe and Ar as the carrier gas respectively, and the molecular signal decreases as the source temperature decreases. These observations lend support to the idea that molecules are being trapped by the clusters in the beam, thus limiting the molecular flux.

Operating the Stark decelerator as a guide, we have tuned the strength of the lenses to measure the transverse acceptance of the decelerator. Using the full length of the lenses, the transmission of molecules through the decelerator was measured as a function of the lens voltage, for different beam speeds and molecules. A dimensionless scaling was found using the strength of a lens, κ, that included the voltage, beam speed and the molecule dipole moment-to-mass ratio. This scaling worked remarkably well over a wide range of parameters, showing it is applicable even when the lenses are anharmonic and the fringe field effects are present. The molecules were guided by the decelerator using the full length of lenses, as such, the molecules moved through the full 3–dimensional electrostatic field of the lenses, and several calculations were developed to explain the observed transmission. The first calculation was for a finite length decelerator with harmonic lenses. The expected transmission increased as the voltage was increased, because the focusing effect of the lenses becomes increasingly stronger than the defocusing effect as the voltage is raised. However, the observed molecular transmission decreased as the voltage was increased. This calculation was improved, taking into account the higher order terms in the transverse electric field expansion for an infinitely long lens. This electric field is stronger in the defocusing plane and weaker in the focusing plane than that given by a purely harmonic field. As a consequence, the focusing force only becomes stronger than the defocusing force above a certain voltage at which point the relative transmission increases above 1. This calculation showed better agreement with the experimental data. However, the best agreement was found when the fringe fields of the lenses were also included in the calculation. In these regions the gradient of the axial electric field magnitude is non-zero, and the transverse field gradients change to accommodate this. In particular, the field gradient along the defocusing axis increases in the fringe field and produces a strengthening of the defocusing force, whilst the gradient in the focusing plane remains relatively unchanged. This has a detrimental effect on the transmission of molecules, it causes the transmission to significantly drop to 20% as the voltage applied to the decelerator is increased, in agreement with the observed transmission. However the observed drop in transmission is faster than that expected from the simulations. This discrepancy remains unsolved and is the subject of continuing experimental work.

CaF molecules have been decelerated for the first time showing a 10% reduction in the kinetic energy. We have demonstrated that we can calculate and implement timing sequences for the synchronous molecule so that it loses/gains a controlled amount of energy per stage. The time of flight data also demonstrated the longitudinal bunching of molecules about the

arrival time of the synchronous molecule. This arises due to the potential well that molecules with small phase and velocity, relative to the synchronous molecule, move in. The depth of the potential well is largest when the speed of the synchronous molecule is unchanged by the timing sequence. More molecules are trapped by this potential barrier, as those that are ahead of the synchronous molecule are decelerated, whilst those that lag behind are accelerated back into the central region of the well. To decelerate the molecules, the velocity of the potential well (synchronous molecule) is lowered by increasing the time intervals between switching the fields off and on so that the synchronous molecule moves up the Stark potential hill. Now, the relative phase and velocity oscillations of the molecules are limited by the height of the Stark potential hill. The timing sequence has been continuously shifted so that the bunched molecules sample the full Stark potential hill and this has shown the bunched molecules arrive at consistently later times and has also demonstrated the loss in intensity as the bunched molecules move closer to the top of the Stark hill. Finally we have considered the time of arrival of the decelerated molecules more closely, and found that a more accurate interpretation of this data is possible when the velocity distributions are also considered.

In summary, the Stark decelerator has been tested over a wide range of parameters encompassing different molecular species, beam speeds, applied voltages and timing sequences. The data observed agrees rather well with our simulations and more detailed experimental study is still underway.

6.2 Future Directions

6.2.1 Improvements to the Experimental Set-Up

In the short term, bringing the decelerator closer to the skimmer aperture by removing the gate valve that is presently in place between the two, would improve the operation of the decelerator. The incident solid angle on the entrance of the decelerator will increase by a factor of 3 and this would allow the beam to be limited by the skimmer aperture, rather than by the entrance aperture of the decelerator, thus increasing the flux of molecules through the decelerator.

6.2.2 Improved Transverse Field Profile

A significant improvement to the decelerator itself would be to design lenses whose high order terms in the electrostatic field are smaller than in the current two-rod lens design. It has been found [36] that one such lens is composed of four cylindrical electrodes placed on the corners of a square. An AG guide which implements the four–electrode geometry has been built in our laboratory. This is in the process of being tested and will pave the way for a four rod decelerator.

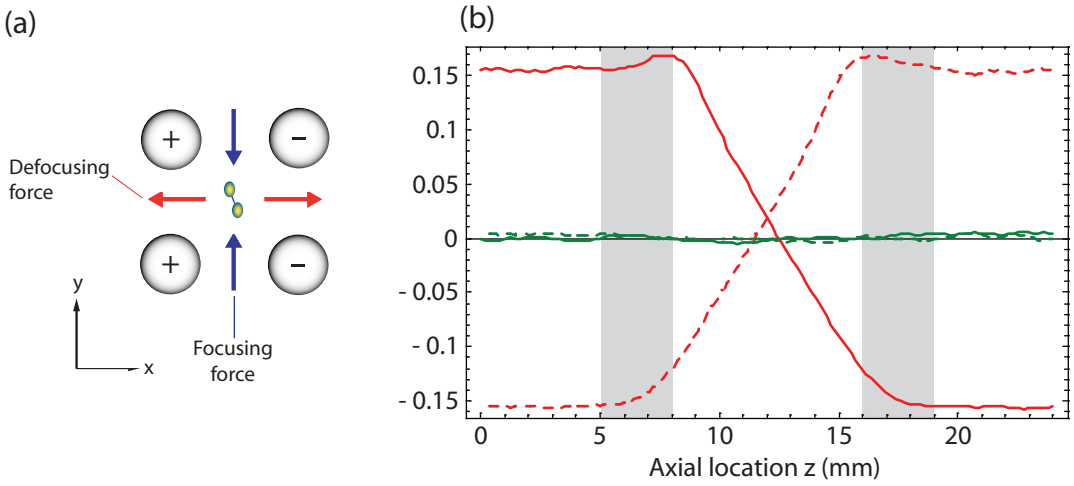

Figure 6.1: (a) The improved 4-electrode lens geometry has four electrodes arranged on the corners of a square and charged as indicated by the + and - signs. (b) A polynomial of the form $f(q) = 1+aq^2+bq^4$ is fitted to the transverse electric field along the x and y axes, where q is the transverse displacement. Variation of the fitting variables a (red curves) and b (green curves) beginning at the centre of one lens 24 mm to the centre of the next lens. Full (dashed) lines indicates the fits to the electric field magnitude along the focusing (defocusing) directions. The origin of the coordinate system is at the centre of the first lens and the grey regions indicate the hemispherical ends of the bullets. The variable q denotes transverse displacement.

In order to illustrate the improvement brought about by this geometry, consider a general 2–dimensional electrostatic potential $\phi(x, y)$, that is also consistent with Laplace's equation. Due to the cylindrical symmetry of the lens electrodes, we consider the multipole expansion of $\phi(x, y)$, this is

$$\phi(x,y) = \phi_0 \left[\sum_{n=1}^{\infty} \frac{a_n}{n} \left(\frac{r}{r_0} \right)^n \cos(n\theta) + \sum_{n=1}^{\infty} \frac{b_n}{n} \left(\frac{r}{r_0} \right)^n \sin(n\theta) \right], \tag{6.1}$$

where $r = \sqrt{(x^2+y^2)}$ and $\theta = tan^{-1}(\frac{y}{x})$. a_n and b_n are dimensionless constants. r_0 and ϕ_0 are scaling factors that characterize the size of the electrode structure and the applied voltages respectively. The electric field magnitude at the centre is given by $E_0 = (\phi_0/r_0)\sqrt{(a_1^2+b_1^2)}$. This multipole expansion is the most general expression of a z–independent electrostatic potential. It can be simplified when the electrode potentials are symmetric under reflection in the x-axis and anti-symmetric about the y-axis. With this restriction, the coefficients b_n are zero for all n and only the coefficients a_n that are odd in n are kept.

As we wish to minimize the higher order terms responsible for the lens aberrations we can re-write the electrostatic potential keeping terms in a_1, a_3 and a_5 only as

$$\phi(x,y) = \phi_0 \left(a_1 \frac{x}{r_0} + a_3 \frac{(x^3 - 3xy^2)}{3r_0^3} + a_5 \frac{(x^5 - 10x^3y^2 + 5xy^4)}{5r_0^5} + \ldots \right). \tag{6.2}$$

The electric field magnitude can be derived from the potential using

$$E(x,y) = \sqrt{\left(\frac{\partial\phi}{\partial x}\right)^2 + \left(\frac{\partial\phi}{\partial y}\right)^2}. \tag{6.3}$$

In the region $r < r_0$ between the electrodes the field can be expanded as a power series, and with $a_5 \ll a_3 \ll a_1$,

$$E(x,y) = E_0\left(1 + \frac{a_3}{a_1}\frac{(x^2-y^2)}{r_0^2} + 2\left(\left(\frac{a_3}{a_1}\right)^2 - 3\frac{a_5}{a_1}\right)\frac{x^2y^2}{r_0^4} + \frac{a_5}{a_1}\frac{(x^4+y^4)}{r_0^4} + \ldots\right). \tag{6.4}$$

For the two electrode lens, $a_3/a_1 = 0.143$ and $a_5/a_1 = 0.02$. A big improvement can be made using four electrodes as shown in Figure (6.1) (a). This gives $a_3/a_1 = -0.139$ and $a_5/a_3 = +0.002$. So with this geometry the aberrations due to the coefficient a_5/a_1 are minimized whilst keeping a_3/a_1 a modest size. A fit to the electrostatic field of the 4-electrode lens along the x and y–axes as a function of axial position showed that the localized strengthening of the defocusing force in the fringe field is almost absent as shown in Figure (6.1) (b). This design also has the benefit that the focusing and defocusing planes can be interchanged by simply switching the applied voltages. The electric field magnitude on the molecular beam axis is ∼41% of the corresponding value for a two-electrode lens. As the amount of deceleration is proportional to the on-axis field this is a disadvantage, however, the benefit of a reduced size of a_5/a_1 may offset this. A guide that implements the four-electrode geometry has been constructed and is in the process of being tested.

6.2.3 A new more intense molecular beam source

Currently our group is investigating the use of a cryogenic buffer gas source of cold polar diatomic molecules. This source holds the promise of providing more than a hundred times as many molecules as our supersonic source and at significantly lower velocity. The buffer gas is helium gas, cooled to 4 K or lower in a cryostat. The molecules are produced by the laser ablation of a target that sits inside the cryogenic cell. The molecules thermalize with the cold helium gas and escape through a hole in the gas cell. This technique has yielded 6×10^{11} YbF molecules per pulse using room temperature Ar as the buffer gas, already more than a hundred times as many molecules as we make in our supersonic beams. Work is underway to build a 4 K helium cryostat which is expected to reduce the velocity of the beams to ∼200 m/s which is the terminal velocity of the escaping helium. The high intensity of the source and the low speeds of the molecular beams enable very efficient coupling to a Stark decelerator or the four electrode guide.

Together, these technologies will enable a wealth of new experimental possibilities in biophysics, cold quantum chemistry, metrology and the physics of ultracold dipolar gases.

Bibliography

[1] C. N. Cohen-Tannoudji. Manipulating atoms with photons. *Reviews of Modern Physics*, 70(3):707, 1998.

[2] C. E. Wieman, D. E. Pritchard, and D. J. Wineland. Atom cooling, trapping and quantum manipulation. *Reviews of Modern Physics*, 71(2):S253, 1999.

[3] J. J. Hudson, B. E. Sauer, M. R. Tarbutt, and E. A. Hinds. Measurement of the electron electric dipole moment using YbF molecules. *Physical Review Letters*, 89(2):023003–1, 2002.

[4] J. J. Hudson *et al.* Towards a new measurement of the electron's electric dipole moment. In *Laser Spectroscopy*, volume 17, page 129, Singapore, 2005. World Scientific.

[5] B. E. Sauer, H. T. Ashworth, J. J. Ashworth, J. J. Hudson, and E. A. Hinds. Probing the electron EDM with cold molecules. In C. Roos, H. Haffner, and R. Blatt, editors, *Atomic Physics*, volume 20, page 44, New York, 2007. American Insitute of Physics.

[6] R. V. Krems. Molecules near absolute zero and external field control of atomic and molecular dynamics. *International Reviews in Physical Chemistry*, 24(1):99, 2005.

[7] E. R. Hudson *et al.* Production of cold formaldehyde molecules for study and control of chemical reaction dynamics with hydroxyl radicals. *Physical Review A*, 73(6):063404, 2006.

[8] A. Micheli, G. K. Brennen, and P. Zoller. A toolbox for lattice-spin models with polar molecules. *Nature Physics*, 2:341, 2006.

[9] D. DeMille. Quantum computation with trapped polar molecules. *Physical Review Letters*, 88(6):067901–1, 2002.

[10] J. Herbig *et al.* Preparation of a pure molecular quantum gas. *Science*, 301:1510, 2003.

[11] D. Wang *et al.* Photoassociative production and trapping of ultracold KRb molecules. *Physical Review Letters*, 93(24):243005–1, 2004.

[12] S. D. Kraft *et al.* Formation of ultracold LiCs molecules. *Journal of Physics B: Atomic, Molecular and Optical Physics*, 39:S993, 2006.

[13] S. A. Rangwala, T. Junglen, T. Rieger, P. W. H. Pinske, and G. Rempe. Continuous source of translationally cold dipolar molecules. *Physical Review A*, 67:043406–1, 2003.

[14] K. Maussang, D. Egorov, J. S. Helton, S. V. Nguyen, and J. M. Doyle. Zeeman relaxation of CaF in low-temperature collisions with helium. *Physical Review Letters*, 94(12):123002–1, 2005.

[15] J. D. Weinstein, R. deCarvalho, T. Guillet, B. Friedrich, and J. M. Doyle. Magnetic trapping of calcium monohydride molecules at millikelvin temperatures. *Nature*, 395:148, 1998.

[16] D. Egorov *et al.* Buffer gas cooling of NH via the beam loaded buffer-gas method. *The European Physical Journal D*, 31:307, 2004.

[17] J. D. Weinstein *et al.* Spectroscopy of buffer-gas cooled vanadium monoxide in a magnetic trapping field. *Journal of Chemical Physics*, 109(7):2656, 1998.

[18] S. E. Maxwell *et al.* High flux beam source for cold, slow atoms or molecules. *Physical Review Letters*, 95(17):173201–1, 2005.

[19] S. Schiller and C. Lammerzahl. Molecular dynamics simulation of sympathetic crystallization of molecular ions. *Physical Review A*, 68:053406–1, 2003.

[20] M. A. van Eijkelenborg, M. E. M. Storkey, D. M. Segal, and R. C. Thompson. Sympathetic cooling and detection of molecular ions in a penning trap. *Physical Review A*, 62:011401–1, 2000.

[21] K. Molhave and M. Drewsen. Formation of translationally cold MgH^+ and MgD^+ molecules in an ion trap. *Physical Review A*, 62:011401–1, 2000.

[22] Giacinto Scoles, editor. *Atomic and Molecular Beam Methods*, volume 1. Oxford University Press, Oxford, United Kingdom, 1988.

[23] M. R. Tarbutt et al. A jet beam source of cold YbF radicals. *Journal of Physics B: Atomic, Molecular and Optical Physics*, 35:5013, 2002.

[24] M. Gupta and D. Hershbach. A mechanical means to produce intense beams of slow molecules. *Journal of Physical Chemistry*, 103:10670, 1999.

[25] R. Fulton, A. I. Bishop, and P. F. Barker. Optical stark decelerator for molecules. *Physical Review Letters*, 93:243004–1, 2004.

[26] R. Fulton, A. I. Bishop, M. N. Schneider, and P. F. Barker. Optical stark deceleration of nitric oxide and benzene molecules using optical lattices. *Journal of Physics B: Atomic, Molecular and Optical Physics*, 39:S1097, 2006.

[27] H. L. Bethlem, F. M. H. Crompvoets, R. T. Jongma, S. Y. T. van de Meerakker, and G. Meijer. Decelerating neutral dipolar molecules. *Physical Review Letters*, 83(8):1558, 1999.

[28] H. L. Bethlem, F. M. H. Crompvoets, R. T. Jongma, S. Y. T. van de Meerakker, and G. Meijer. Deceleration and trapping of ammonia using time-varying electric fields. *Physical Review A*, 65:053416–1, 2002.

[29] J. R. Bochinski, E. R. Hudson, H. J. Lewandowski, G. Meijer, and J. Ye. Phase space manipulation of cold free radical OH molecules. *Physical Review Letters*, 24:243001–1, 2003.

[30] S. Y. T. van de Meerakker, P. H. M. Smeets, N. Vanhaecke, R. T. Jongma, and G. Meijer. Deceleration and electrostatic trapping of OH radicals. *Physical Review Letters*, 2:023004–1, 2005.

[31] S. Jung, E. Tiemann, and C. Lisdat. Cold atoms and molecules from fragmentation of decelerated So_2. *Physical Review A*, 74:040701–1, 2006.

[32] S. Y. T. van de Meerakker, I. Labazan, S. Hoekstra, J. Kupper, and G. Meijer. Production and deceleration of a pulsed beam of metastable NH($a^1\Delta$) radicals. *Journal of Physics B: Atomic, Molecular and Optical Physics*, 39:S1077, 2006.

[33] E. D. Courant and H. S. Snyder. Theory of the alternating gradient synchrotron. *Annals of Physics*, 3:1, 1958.

[34] H. L. Bethlem, A. J. A. van Roij, R. T. Jongma, and G. Meijer. Alternate gradient focusing and deceleration of a molecular beam. *Physical Review Letters*, 88(13):133003–1, 2002.

[35] M. R. Tarbutt et al. Slowing heavy, ground–state molecules using an alternating gradient decelerator. *Physical Review Letters*, 97(17):173002–1, 2002.

[36] H. L. Bethlem et al. Alternating gradient focusing and deceleration of polar molecules. *Journal of Physics B: Atomic, Molecular and Optical Physics*, 39:R263, 2006.

[37] W. H. Wing. On neutral particle trapping in quasistatic electromagnetic fields. *Progress in Quantum Electronics*, 8:181, 1984.

[38] W. Ketterle and D. E. Pritchard. Trapping and focussing ground state atoms with static fields. *Applied Physics B*, 54:403–406, 1992.

[39] Daniel Auerbach, Edward E. A. Bromberg, and Lennard Wharton. Alternate–gradient focusing of molecular beams. *The Journal of Chemical Physics*, 45(6):2160, 1966.

[40] D. A. McQuarrie. *Quantum Chemistry*. Oxford University Press, Oxford, United Kingdom, 1983.

[41] A. R. Edmonds. *Angular Momentum in Quantum Mechanics*. Princeton University Press, New Jersey, USA, 1996.

[42] http://www.comsol.com/.

[43] Jr. Stanley Humphries. *Charged Particle Beams*. John Wiley & Sons Inc., New York, USA, 1990.

[44] John D. Walecka. *Fundamentals of Statistical Mechanics: Manuscript and Notes of Felix Bloch*. Imperial College Press, London, United Kingdom, 2000.

[45] K. J. Astrom and T. Hagglund. *PID Controllers: Theory, Design and Tuning*. Instrument Society of America, USA, 1994.

[46] Bengt Edlén. The refractive index of air. *Metrologia*, 2:71, 1966.

[47] E. Kuffel, W. S. Zaengl, and J. Kuffel. *High Voltage Engineering: Fundamentals*. Newnes, Oxford, United Kingdom, 2000.

[48] J. B. Anderson and J. B. Fenn. Velocity distributions in molecular beams from nozzle sources. *Physics of Fluids*, 8:780, 1965.

[49] Paul Constantine Condylis. *Measuring the electron electric dipole moment using supersonic YbF*. PhD thesis, University of London, February 2006.

[50] http://encyclopedia.airliquide.com/encyclopedia.asp.

[51] Jun Wang. *Laser and radiofrequency spectroscopy of ytterbium fluoride ground state*. PhD thesis, Yale University, December 1996.

[52] B. E. Sauer, J. Wang, and E. A. Hinds. Laser-rf double resonance spectroscopy of ^{174}YbF in the $X^2\Sigma^+$ state. *Journal of Chemical Physics*, 105:7412, 1996.

[53] B. E. Sauer, J. Wang, and E. A. Hinds. Anomalous spin-rotation coupling in the $X^2\Sigma^+$ state of YbF. *Physics Review Letters*, 74:1554, 1995.

[54] B. E. Sauer, S. B. Cahn, M. G. Kozlov, G. D. Redgrave, and E. A. Hinds. Perturbed hyperfine doubling in the $A^2\Pi_{1/2}$ and the [18.6]0.5 state of YbF. *Journal of Chemical Physics*, 110:8424, 1999.

[55] P. C. Condylis, J. J. Hudson, M. R. Tarbutt, B. E. Sauer, and E. A. Hinds. Stark shift of the $A^2\Pi_{1/2}$ state in ^{174}YbF. *The Journal of Chemical Physics*, 123(23), 2005.

[56] Jonathan James Hudson. *Measuring the electric dipole moment of the electron with YbF molecules*. PhD thesis, University of Sussex, September 2001.

[57] W. J. Childs and L. S. Goodman. High-precision laser-rf double-resonance spectroscopy of the $^2\Sigma$ ground state of CaF. *Physical Review A*, 21(4):1216, 1980.

[58] L. A. Kaledin, J. C. Bloch, M. C. McCarthy, and R. W. Field. Analysis and deperturbation of the $A^2\Pi$ and $B^2\Sigma^+$ states of CaF. *Journal of Molecular Spectroscopy*, 197:289, 1999.

[59] P. J. Dagdigian, H. W. Cruse, and R. N. Zare. Radiative lifetimes of the alkaline earth monohalides. *Journal of Chemical Physics*, 60(6):2330, 1974.

[60] M. Pelegrini, C. S. Vivacqua, O. Roberto-Neto, F. R. Ornellas, and F. B. C. Machado. Radiative transition probabilities and lifetimes of the band systems $A^2\Pi$–$X^2\Sigma^+$ of the isovalent molecules BeF, MgF and CaF. *Brazilian Journal of Physics*, 35(4A):950, 2005.

[61] W. Demtroder. *Laser Spectroscopy: Basic Concepts and Instrumentation*. Springer-Verlag, Berlin, Germany, 2002.

[62] R. A. Smith, T. Ditmire, and J. W. G. Tisch. Characterization of a cryogenically cooled high-pressure gas jet for laser/cluster interaction experiments. *Review of Scientific Instruments*, 69(11):3798, 1998.

[63] O. F. Hagena. Cluster ion sources (invited). *Review of Scientific Instruments*, 63(4):2374, 1991.